U.PORTO

FEUP **FACULDADE DE ENGENHARIA**
UNIVERSIDADE DO PORTO

Thermomechanical modeling of semi-crystalline polymers

Advisor:
Dr. Francisco Manuel Andrade Pires
Co-advisor:
Dr. Bernardo Proença Ferreira

Author:
José Luís Passos Vila-Chã

Seminar presented under the scope of the
Doctoral Program in Mechanical Engineering

Porto, March 2023

Page intentionally left blank.

Abstract

Thermomechanical modeling of semi-crystalline polymers

Keywords: computational mechanics, constitutive modeling, semi-crystalline polymers, thermomechanics, multi-physics

Semi-crystalline polymeric materials are increasingly used in structural, medical, and electronic applications. Polymers such as high-density polyethylene (HDPE) and polypropylene (PP) are widely used in commodity applications such as packaging, while polyamides (PA) and polyether ether ketones (PEEK) are stiffer and therefore chosen for more demanding engineering applications. The microstructure of semicrystalline polymers is particularly complex, consisting of closely packed crystalline lamellae separated by layers of an amorphous polymer. The addition of fillers and particles to create new polymeric blends with enhanced behavior, a standard practice in engineering and industrial environments, significantly increases the overall complexity. Hence, this work seeks to provide a thorough review of the thermomechanical behavior of semi-crystalline polymers with the goal of developing an accurate description through macroscopic constitutive modeling. Their behavior is strongly nonlinear, exhibiting phenomena such as double yielding, nonlinear dependence of the yield stress on the strain rate, thermal softening, and rubber-like strain hardening. A detailed overview of the available models in the literature is provided, with particular focus on those based on rheological models with nonlinear elastic and viscous elements. Regarding the use of these models to describe semi-crystalline polymers, bulk crystallinity is often included through a mixture rule, such as the Voigt or Reuss mixture rule.

Moreover, self-heating is widely observed when semi-crystalline polymers are loaded at moderate strain rates, such that substantial heat is produced with a corresponding change in temperature. Thus, an appropriate description of this class of materials requires the solution of a thermomechanical problem. Implicit partitioned methods are identified as the most suitable solution methods due to several attractive features, namely taking advantage of existing software, providing accurate results that agree with a monolithic approach, being easy to implement, and being competitive in terms of computational efficiency, both in terms of speed, through the use of convergence acceleration techniques, as in terms of memory. The strategies discussed and explored in the present work are applied specifically to the thermomechanical problem, but they can be readily applied to other multi-physics phenomena. In particular, the fixed-point method, the underrelaxation method, the Aitken relaxation, the Broyden-like family of methods, the Newton-Krylov methods, and the polynomial vector extrapolation methods MPE and RRE in cycling mode are compared when applied to an elastoplastic constitutive model.

Page intentionally left blank.

Contents

List of Figures

Page intentionally left blank.

List of Tables

Page intentionally left blank.

Chapter 1

Introduction

1.1 Context

Design permeates engineering. According to Ashby (Ashby, 1999), the main features of mechanical design are function, material, shape, and process. There is a profound interplay between all these facets of design when developing a mechanical component. Accordingly, the component must meet functional criteria in terms of its thermomechanical behavior. Additional specifications of its electric, magnetic, or mass transfer characteristics may also be prescribed. The aptitude of a component to satisfy these demands is determined by the material or materials from which it is made, as well as its shape. Some materials, however, cannot be manufactured into a particular shape or by using a specific manufacturing process. Weight, cost, and environmental impact reduction can all be included as goals, and their achievement is closely related to the material and method selected.

An even more intimate relationship between the final performance of the mechanical component and the process selected for its manufacturing may be uncovered by taking into account the hierachical structure of engineering materials. Olson (Olson, 2000) emphasizes the cause/effect relationship between the process, the material's structure at multiple scales ranging from the nanoscale to the macroscale, the material's properties, and its final performance. The reverse goals/means perspective can also be adopted where a given performance requirement drives the search for a material with a particular set of properties. These in turn may only be realised if the appropriate multi-scale structure is obtained through a suitable process. Ashby (Ashby, 1999) highlights that first-order differences between the properties of materials, e.g., polymers and metals, are due to the mass of the atoms, the nature of the inter-atomic forces and the geometry of the atomic packing. The magnitude of the effect due to the microstructure on the properties of a material is generally an order of magnitude less than that of bonding and structure.

"Integrated Computational Materials Engineering" (ICME) is a systematic approach proposed by Horst and Wang (Horstemeyer and Wang, 2003) that includes the process-structure-property-performance relationships within a computational framework. Its goal is the simultaneous design of a component, the materials that it is composed of and the manufacturing process employed to produce it, taking into account the material's structure at different scales. To realize this vision, suitable models and numerical tools for simulating manufacturing processes and component

life at a given time and length scale must be available. Experimental methods to probe the model's validity and acquire the corresponding material parameters are also crucial. To accurately capture the behavior of the material, the correct boundary conditions, initial conditions, and material parameters must be established at each scale and time-frame. An adequate way to transfer information between the different scales must also be devised.

Taking into account the hierarchical nature of a material's structure, appropriate models must be set up at the structural (meters, centimeters), macro (millimeters), meso (hundreds to tenths of micrometers), micro (micrometers), and atomic/nanoscale (angstrom). Directly relevant to this work are both the structural and the macroscale scales. Concerning the first, solutions from FEM are used to model the thermomechanical behavior both during manufacturing and the service life of a component or machine, with full-scale experiments being needed to gauge the accuracy of the predictions. To achieve such a description, an appropriate constitutive/rheological model must be devised at the macroscale. Its validation is performed through its use in suitable FEM simulations and comparison with simple mechanical experiments, e.g., uniaxial or torsion experiments. An even more faithful description of a polymer blend, for example, may be achieved by retaining the appropriate continuum constitutive models and including an accurate mesoscale representation employing, for example, computational homogenization. However, this is outside the scope of the present work.

1.2   Motivation

The current work focuses on two aspects of the paradigm mentioned above: the use of FEM to predict the structural response of a component under multi-physics constraints, particularly those involving thermomechanical phenomena, and the macroscale constitutive description of semi-crystalline polymers. As such, the following sections provide two brief introductions to each topic.

1.2.1   Multi-physics simulations [1]

It is generally understood that thermomechanics is crucial in the description of many engineering applications and a highly sought-after feature in computational models. Thermomechanical effects play a central role in mainstream and heavy-duty applications such as rocket nozzles (Kuhl et al., 2002; Danowski et al., 2013), disk brakes and clutches (Yevtushenko et al., 2015), heat-assisted incremental sheet forming (Liu, 2018) and thermal stresses due to machining (Elsheikh et al., 2021), to name a few examples. There is a profound interplay between the mechanical and the thermal field:

- the thermal field influences the mechanical field through additional thermal stresses and potentially temperature-dependent material properties;

- the mechanical field affects the thermal field through coupling terms, which can be interpreted as heat sources (dissipation and thermomechanical structure heating), as well as through geometric coupling due to the deformation of the domain, which affects boundary conditions and the heat conduction law.

_____

[1]Adapted from Vila-Chã et al. (2023).

More sophisticated applications, such as the sintering process inspired by a Hybrid FAST process described in Rothe et al. (2014), also exist, where a direct current and an external heat source using convection are used to control the temperature in the die/punch/powder system. As a result, an appropriate description of the electric, thermal, and mechanical fields, as well as their interaction, must be taken into account.

Returning to the thermomechanical problem, its thermodynamically consistent formulation is necessary for the development of an appropriate solver. Having achieved an appropriate formulation of the problem, the Finite Element Method can be used to solve it. After spatial and temporal discretization, the thermomechanical problem is reduced to a system of coupled nonlinear algebraic equations on the mechanical variables (displacement) and thermal variables (temperatures). Generally speaking, the strategies typically employed to solve this problem can be classified into monolithic and partitioned approaches. The latter can be further divided into explicit (loosely or weakly coupled) and implicit (strongly coupled) schemes, depending on the type of coupling enforcement. When comparing them, one should keep in mind that the most desirable properties of an algorithm for solving coupled problems are unconditional stability, high accuracy, ease of implementation, low memory requirements, high computational efficiency, and the potential for software reuse (Felippa and Geers, 1988). Although a significant fraction of scientific research on solution techniques for coupled multi-physics problems has not originated from the thermomechanics community but rather from the Fluid-Structure Interaction field, the following sections present a review of these concepts linked with thermomechanics literature. Conversely, the observations and results provided in this work in the context of thermomechanics may be generalized to other multi-physical phenomena.

Monolithic schemes

Monolithic algorithms solve the nonlinear multi-physics system of equations simultaneously, fulfilling the coupling conditions exactly. Together with implicit time-integration techniques, monolithic schemes can provide unconditional stability and are typically associated with good robustness. These methods are often typified by the direct application of Newton's method to the coupled equations, requiring the computation of the cross-derivative blocks between fields. To solve the potentially large system of equations arising from the application of Newton's method, iterative methods are preferable to direct methods, partly due to memory footprint considerations. Newton-Krylov methods with the generalized minimal residual method (GMRES) or the biconjugate gradient stabilized method (BiCGStab) as Krylov subspace solvers are among the most widely used in multi-physics problems (Hron and Turek, 2006). The effective solution of a large system of equations, including any potential nonlinearities, is particularly difficult for monolithic algorithms (Danowski et al., 2013), as the algebraic properties of different blocks can be very distinct. In fact, a good preconditioning strategy is a key component of effective solvers for large-scale multi-physics problems and this has been the main development topic of monolithic schemes in the last decade (Tezduyar et al., 2006; Lin et al., 2010; Gee et al., 2011; Danowski et al., 2013; Verdugo and Wall, 2016; Mayr et al., 2020). In short, the great appeal of monolithic schemes is the robustness and stability of the solution method, which comes at the expense of poor flexibility as well as extensive development and maintenance costs.

Monolithic schemes have been successfully used in the literature to tackle thermomechanical problems considering a variety of constitutive behaviors. Carter and Booker (Carter and Booker, 1989) consider thermoelastic materials, Gawin and Schrefler (Gawin et al., 1996) deal with thermo-hydro-mechanical problems in partially saturated porous materials, while Ibrahimbegovic and Chorfi (Ibrahimbegovic and Chorfi, 2002) present a thermoplasticity covariant formulation, including large viscoplastic strains, strain localization, and cyclic loading cases. Danowski (Danowski, 2014) deals with various temperature-dependent, isotropic, elastic, and elastoplastic material models for small and finite strains, incorporating the effect of high temperatures predominating in rocket nozzles. Both Netz (Netz, 2013) and Rothe and coworkers (Rothe et al., 2015) present monolithic approaches, based on the multilevel Newton method, for the solution of the thermomechanical problem involving thermovisco-plastic materials. More recently, Felder and coworkers (Felder et al., 2022) proposed a finite strain thermomechanically coupled two-surface damage-plasticity theory. The authors obtain the solution for the three coupled fields, displacement, nonlocal damage variable, and temperature, employing an implicit and monolithic solution scheme. Relevant application of monolithic solution schemes to thermomechanical contact interaction can be found in Zavarise et al. (1992); Wriggers and Zavarise (1993); Oancea and Laursen (1997); Hüeber and Wohlmuth (2009); Dittmann et al. (2014); Seitz et al. (2018).

Partitioned schemes

The earliest contributions regarding the partitioned treatment of coupled systems emerged in the mid-1970s, involving structure-structure interactions and fluid-structure interactions (see, e.g., Belytschko and Mullen (1976), Park et al. (1977), Belytschko and Mullen (1978), Hughes and Liu (1978) and Belytschko et al. (1979)). There are usually many ways of partitioning a complex system into subsystems or fields. Felippa and Park (Felippa and Park, 1980) provide a very pragmatic and helpful criterion for selecting the fields to be considered. According to their definition, a field is characterized by computational considerations. It is a segment of the overall problem for which a separable software module is either available or readily prepared if the interaction terms are suppressed. As such, a partitioned approach to the solution of multi-physics problems employs analyzers specific to each field separately integrated in time. The coupling between the fields is achieved through proper communication between the individual components using prediction, substitution, and synchronization techniques. Although this renders a flexible and easy-to-implement solution scheme, it suffers from some numerical issues, as discussed shortly.

As previously stated, partitioned schemes can be either explicit or implicit. In explicit schemes, the solution is found by solving each field sequentially with a one-directional data transfer, using a suitable problem split. In one exemplary time step, an explicit coupling algorithm solves the mechanical problem first, then sends relevant data to the thermal solver, and finally solves the thermal problem without providing feedback on the thermal solution to the mechanical solver. It has been used in the context of thermoelasticity (Argyris and Doltsinis, 1981; Armero and Simo, 1992; Johansson and Klarbring, 1993; Miehe, 1995a,b; Holzapfel and Simo, 1996), thermoplasticity (Armero and Simo, 1992, 1993; Simo and Miehe, 1992b; Wriggers et al., 1992; Agelet de Saracibar, 1998; Agelet de Saracibar et al., 1999; Lee et al., 2015), thermoviscoplasticity (Adam and Ponthot, 2002, 2005; Miehe et al., 2011) and contact

(Wriggers and Miehe, 1994; Agelet de Saracibar, 1998; Xing and Makinouchi, 2002; Bergman and Oldenburg, 2004). The isothermic and adiabatic splits are the most common operator splits in thermomechanical problems. The isothermal split is arguably the most straightforward and natural approach, as noted in Argyris and Doltsinis (1981), one of the earliest contributions on the topic. This scheme seeks to solve the thermomechanical problem by first solving the mechanical problem at a constant temperature and then solving a purely thermal phase at a fixed configuration—newly updated. As an alternative, Armero and Simo (Armero and Simo, 1992) proposed the adiabatic split, which consists of a mechanical phase at constant entropy, followed by purely thermal conduction at fixed configuration. In terms of implementation complexity, the adiabatic split is comparable to the isothermal split and is unconditionally stable, a remarkable advantage in comparison with the conditionally stable isothermal split. It is, however, more challenging to extend to other material models as it requires the modification and creation of specific algorithmic components at the constitutive level which might not be readily available.

There are several techniques to improve the stability and accuracy characteristics of explicit partitioned approaches, e.g., algebraic augmentation (Park et al., 1977; Park, 1983), double-pass approach (Armero and Simo, 1992; Piperno, 1997; Farhat et al., 2006, 2010), prediction techniques (Piperno, 1997; Piperno and Farhat, 2001; Michler, 2005; Farhat et al., 2006), and subcycling (Piperno et al., 1995; Farhat et al., 1997; Piperno, 1997). Irrespective of the theoretical temporal convergence order of the partitioned explicit scheme, the fully coupled discretized equations of the problem will never be exactly satisfied at each time instant. There is a lag between the solution of the different fields, e.g., the mechanical and thermal fields, in a thermomechanical problem, which can be interpreted as an additional discretization error (Michler, 2005). The convergence conditions of partitioned solution procedures are also discussed by Turska and Schrefler (Turska and Schrefler, 1993) in the context of consolidation problems.

In implicit schemes, inter-field iterations are performed until a given tolerance for the different field's unknowns is reached—irrespective of the type of operator split employed. It converges to the solution of the monolithic scheme and thus can satisfy the discrete version of the coupled problem exactly. Regardless of the eventual conditional stability of the corresponding explicit scheme, the implicit alternative can be unconditionally stable—it has the same temporal stability properties as the monolithic scheme—but the convergence of the inter-field iterations is not guaranteed or may take an excessive number of iterations. This embodies a significant limitation and places a severe restriction on the use of these strategies. Nonetheless, several acceleration techniques are available in the literature to speed up convergence. Most of these are developed in the context of Fluid-Structure Interaction and their application to thermomechanical problems is not widespread.

There are a few contributions regarding the use of implicit partitioned schemes in the context of thermomechanics. Erbts and Düster (Erbts and Düster, 2012) solve problems involving thermoelasticity at finite strains, Netz (Netz, 2013) explores thermoviscoelastic problems, and Danowski (Danowski, 2014) presents results on thermoelasticity and thermoelastoplasticity. Including more than two fields, Erbts and coworkers (Erbts et al., 2015) tackle electro-thermomechanical problems, as do Wendt and coworkers (Wendt et al., 2015), which also consider radiative heat transfer. Successful applications to thermomechanical problems involving contact have been reported in Johansson and Klarbring (1993); Rieger and Wriggers (2004); Temizer

(2011); Krüger et al. (2020), to name a few.

Regarding computational efficiency, according to Michler (Michler, 2005), solving a fluid-structure interaction problem to the same accuracy using an explicit scheme is less efficient than employing an implicit approach. For the same total number of iterations, the difference in the accuracy reached ranges from one to three orders of magnitude—although the implicit coupling is more expensive for the same number of iterations, naturally. These findings contradict a claim made in Felippa et al. (2001), which is not supported by any numerical results. In the numerical examples presented in Danowski (2014), the monolithic solver is, in most cases, faster than an implicit scheme employing Aitken relaxation for problems in thermomechanics. The differences range from 120% to 140% in favor of the monolithic scheme. Supporting evidence for these conclusions can also be found in Novascone et al. (2015). The authors report CPU time ratios between the implicit partitioned and monolithic approaches, ranging from 0.635 to 3.75 on the coupling magnitude. This evidence suggests that implicit schemes can deliver competitive simulation times with the same accuracy as the monolithic if more sophisticated coupling techniques are used to accelerate the convergence and improve the robustness of the inter-field iterations, with the added benefit of more straightforward implementation and extension.

Lastly, it is important to recall the recommendations given in Felippa et al. (2001) regarding the choice between partitioned and monolithic approaches. According to the authors, the circumstances that favor the partitioned approach for tackling a coupled problem are a research environment with few delivery constraints, access to existing software, localized interaction effects, and widespread spatial/temporal component characteristics. The opposite circumstances, involving a commercial environment, a rigid deliverable timetable, massive software development resources, global interaction effects, and comparable length and time scales, favor a monolithic approach. Therefore, one can readily see a number of applications where partitioned strategies fit very well, involving small development times and preservation of pre-existing technology.

1.2.2   Semi-crystalline polymers

The majority of polymeric materials are made up of extremely long molecule chains with side groups composed of different elements, such as O, F, or Cl, or organic groups, like methyl, ethyl, or phenyl groups. These macromolecules comprise repeat units, which are smaller structural elements replicated along the chain (Callister and Rethwisch, 2014). In turn, the polymer structure can range from a completely amorphous polymer, where the macromolecules are arranged randomly, to a highly crystalline polymer, where most polymer chains are tightly packed into a crystalline structure. In between, one finds semi-crystalline polymers where crystalline and amorphous zones coexist in a variety of structural arrangements (Ward and Sweeney, 2004).

Properties and applications

According to a market study by Precedence Research (Precedence Research, 2022), the polymer market size in 2021 was 713 billion dollars, and it is projected to reach 1078.5 billion by 2030. By type, the thermoplastics segment accounted for 43% market share in 2021. Most semi-crystalline polymers are designated as thermoplastics, as they most often have linear structures and soften/harden when heated/cooled. Thermoplastics dominate the market due to their reduced production costs, energy

efficiency, ability to replace metals with considerable weight savings, and ability to be produced in extremely high volumes with high precision and cheaply.

By material, the polyethylene (PE) segment, a semi-crystalline polymer, has captured a significant market share in 2021 and is growing. It is widely sought after for packaging items, tubing products, connections, bottles, and plastic surgery implants. Increased consumer spending and industrial operations across various industries, including the automobile, building, and packaging, are the main drivers of this increase. Another widely used semi-crystalline polymer is polytetrafluoroethylene (PTFE), employed in many medical and industrial device applications, in particular, in rotary shafts seals, due to its tribological characteristics, chemical inertness and temperature stability (Kletschkowski et al., 2002). Polyamides (PA) are widely used materials due to their low material cost, low density (approximately 12.5% the weight of bronze, 14.3% the weight of cast iron, and 50% the weight of aluminum), corrosion resistance, insulation qualities, and good load bearing capacity. They are frequently used as replacement for bronze, brass, aluminum and other metals (Khan and Farrokh, 2006). PA6 is used in conjunction with PE in polymer films for food packaging, due to its good mechanical strength and impermeability to gas (Zeng et al., 2010). Polyether ether ketone (PEEK) is yet another semi-crystalline polymer which finds use in a variety of structural and insulation applications (Rae et al., 2007). Moreover, due to its excellent mechanical properties, PEEK is commonly used in seals and bearings, and more recently also in medical implants (e.g., spinal implants, screws, woven textiles) (Bergström, 2015), due to its biocompatibility, weight reduction, radiology advantage and 3D printing properties (Garcia-Gonzalez et al., 2015). Its exceptionally high melting temperature also makes it a good candidate for extreme service conditions (G'sell and Dahoun, 1994).

Semi-crystalline polymer structure

Semi-crystalline polymers have a complex and hierarchial heterogeneous morphology. Both their microstructure and their mesostructure will depend on the processing history, as well as mechanical and thermal histories, in addition to the polymer chemistry and conformation (Khoury and Passaglia, 1976; Cangemi and Meimon, 2001; Hoffman et al., 2007).

Microstructure At the microscopic level, semi-crystalline polymers consist of at least two different phases: a crystalline phase and an amorphous phase (Khoury and Passaglia, 1976). The crystalline portion of a semi-crystalline polymer is formed by the constituent chains packing parallel to one another into lamellae in an orderly fashion, as shown in Figure 1.1.

There are at least two types of crystal lamellae found in semi-crystalline polymers, as detailed in Anderson (1964) for polyethylene (PE), the chain-folded lamellae and extended-chain lamellae. In the former, the molecular chains within each platelet fold back and forth on themselves, with folds occurring at the faces. This picture is, in fact, an idealization, with reality resembling more a switchboard model, with the chains reentering through loose folds at non-adjacent sites or even forming tie-chains with neighboring lamellae (G'sell and Dahoun, 1994). The latter is more common at lower molecular weights, with the chains organized into lamellae in their extended conformation. The thickness of the lamellae in semi-crystalline polymers is of the order of nanometers, e.g., 10 nm to 15 nm for PE samples (Argon, 2013).
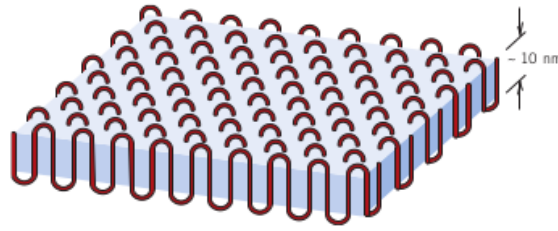
Figure 1.1: Arrangement of polymer chains into a lamella in the crystalline phase of a semi-crystalline polymer (Callister and Rethwisch, 2014).

The crystalline structure depends on the particular polymer. PE often possesses orthorhombic symmetry, where the chain direction forms an angle with the normal vector to the crystalline lamella ranging between 17° and 40° (Nikolov and Doghri, 2000). On the other hand, the crystal structure found in polytetrafluoroethylene (PTFE) at temperatures above 19 °C is hexagonal, with individual molecules arranged in helical conformations (Bergström, 2015).

The crystallinity of a semi-crystalline polymer can be specified by the degree of crystallinity. It may range from completely amorphous to almost entirely crystalline. Ward and Sweeney (Ward and Sweeney, 2004) mention values between 90% for polyethylene (PE) to about 30% for oriented poly(ethylene terephthalate) (PET). Commercially available semi-crystalline polymers range from 10% to 90% in the degree of crystallinity (van Dommelen et al., 2003). The degree of crystallinity by weight may be determined from accurate density measurements according to

$$\chi = \% \text{ crystallinity } = \frac{(\rho_s - \rho_a)/\rho_s}{(\rho_c - \rho_a)/\rho_c} \times 100 \tag{1.1}$$

where ρ_s is the density of a specimen for which the percent crystallinity is to be determined, ρ_a is the density of the completely amorphous polymer, and ρ_c is the density of the perfect polymer crystallite. In addition to this method based on density, other experimental methods employed to determine the crystallinity along with the lamellar thickness of the polymer crystallites include wide (WAXS) and small (SAXS) angle X-ray scattering (Schrauwen et al., 2004; Hobeika et al., 2000), differential scanning calorimetery (DSC) (Ayoub et al., 2011), and, electron microscopy, e.g., transmission electron microscopy (TEM) (Bartczak et al., 1992).

The main parameters influencing the degree of crystallinity are the molecular structure, the molecular weight, the presence of plasticizers, and especially the thermomechanical history of the polymer (Khoury and Passaglia, 1976; Cangemi and Meimon, 2001). Because of the way polymer crystals form, polymer chains must have a linear structure; the more branches/dependent side groups, the lower the degree of crystallinity. However, even linear polymers must have sufficient regularity to crystallize (Khoury and Passaglia, 1976). A high molecular weight tends to suppress a high degree of crystallinity (Hoffman et al., 2007), as seen when comparing high-density polyethylene (HDPE) and ultra-high weight polyethylene (UHWPE) (Brown et al., 2007). Since crystallization is a kinetic process, the crystallization rate in polymers depends on the temperature, with larger temperatures leading to lower rates (Callister and Rethwisch, 2014). As detailed later in this chapter, the mechanical

loading of a polymer may also induce changes in crystallinity, e.g., through the phenomenon of strain-induced crystallization (Rao and Rajagopal, 2001).

Accordingly, the most frequent approach to achieve different degrees of crystallinity is through the control of crystallization temperatures and crystallization times, be it when crystallizing from the melt or through annealing treatments (Fakirov and Krasteva, 2000; Schrauwen et al., 2004). However, preparing samples with different degrees of crystallinity is challenging for polymers such as HDPE since its crystallization rate is very high. It is possible to control the degree of crystallinity by taking PE samples differing in the degree of branching and introducing various amounts of defects in the main chain (Fakirov and Krasteva, 2000).

In what pertains to the amorphous portion of a semi-crystalline polymer, results reported by Zia and coworkers (Zia et al., 2008) on isotactic polypropylene (iPP) point to the existence of two different amorphous phases, a mobile amorphous phase, and a rigid amorphous phase, based on different glass transition temperatures. The results of Jolly (Jolly, 2000) concerning polyamide 11 (PA11), which were found employing WASX at different axial deformation rates, also support the existence of a phase that is neither wholly amorphous nor wholly crystalline. According to Mandelkern (Mandelkern, 2006), the existence of a rigid amorphous phase is supported by experimental results obtained from density measurements, wide and small-angle X-ray diffraction, thermal analyses, Raman spectroscopy, small-angle neutron scattering, dielectric relaxation and nuclear magnetic resonance involving different nuclei and techniques.

The reason for the increased rigidity in this part of the amorphous phase is the presence of polymer crystallites, which hinder the molecular mobility of the amorphous phase (Zia et al., 2008; Peacock, 2014). However, an increase in the degree of crystallinity will decrease the rigid amorphous fraction and the ratio between the rigid and mobile amorphous phases. This behavior is due to reduced covalent coupling between the polymer crystals and the amorphous phase in highly crystalline preparations (Zia et al., 2008). Furthermore, the presence of the crystallites also affects the properties of the mobile amorphous fraction, which is detected by a distinct decrease in its glass transition temperature, as shown for semi-crystalline iPP by Zia and coworkers (Zia et al., 2008).

Mesostructure   According to the processing, thermal and mechanical history, as well as its degree of crystallinity, molecular weight, and polydispersity, a semi-crystalline polymer can display different mesoscopic structures (Cangemi and Meimon, 2001; Mandelkern, 2006). When the polymer crystallizes from a dilute solution, the structure is often lamellar and composed of multiple layers if the solution is quiescent, and of the shish-kebab variety[2] if the solution is subject to high shear (Khoury and Passaglia, 1976; Callister and Rethwisch, 2014; Peacock, 2014). When the polymer crystallizes from the melt, the two most commonly reported types of mesoscopic structures for semi-crystalline polymers are the spherulitic structure (Zeng et al., 2010) (see Figure 1.2(a)), obtained from quiescent crystallization and the shish-kebab structure, obtained from crystallization under shear stress (Peacock, 2014) (see Figure 1.2(b)).

The spherulitic structure is composed of spherulites, an aggregate of ribbon-like chain-folded crystallites that radiate outward from a single nucleation site in the center, their diameter approximately 10 μm and their lammela approximately 10 to 20 nm thick

---

[2]The so-called shish-kebab structure consists of a long central fiber core (shish) surrounded by a lamellar crystalline structure (kebab) periodically attached along the shish. (Na et al., 2006; Peacock, 2014).

(b)

(a)
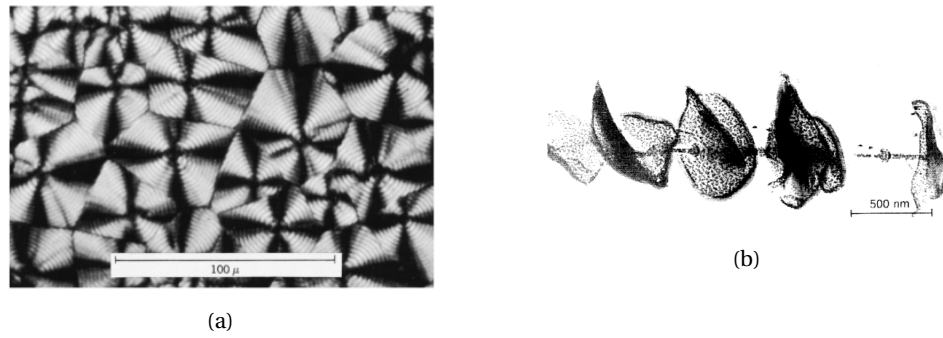
Figure 1.2: Mesostructures of polyethylene. (a) Transmission photomicrograph (using cross-polarized light) of a spherulitic structure (Callister and Rethwisch, 2014). (b) Electron micrograph of shish-kebab structure (Peacock, 2014).

for PE, and 2 to 6 nm for polyether ether ketone (PEEK), for example. Between them, there are amorphous regions, crossed by tie-chain molecules that act as connecting links between adjacent lamellae (Callister and Rethwisch, 2014; Khoury and Passaglia, 1976; Pouriayevali et al., 2013; G'sell and Dahoun, 1994). The lamellae are generally twisted about their long axis (Patlazhan and Remond, 2012). A sheave-like structure is also possible under suitable conditions (Peacock, 2014). Mandelkern (Mandelkern, 2006) warns, however, that spherulites, and other types of supermolecular structures, are not universally observed in homopolymers.

Mechanical loading will also lead to changes in the mesoscopic structure of the polymer. Regarding higher crystallinity polymers such as HDPE, it usually destroys the crystallites of the original morphology, followed by reordering to form new crystallites. The new lamellar morphology has a lamellar thickness independent of the original lamellar thickness, solely dependent upon the temperature at which the deformation occurred. In such morphologies, the unit cell axes are preferentially aligned in the stress direction, while the lateral planes of the lamellae lie approximately normal to the aligning force. These newly formed crystallites are themselves subject to disruption at higher deformation levels (draw ratios of approximately 10), being replaced by a fibrillar morphology, which consists of oriented crystallites arranged hierarchically into needle-like structures of various sizes. These macrofibrils are composed of microfibrils, in turn, made up of nanofibrils, stacks of crystallites separated by thin noncrystalline "plates," portions of which are spanned by "intercrystalline bridges" (Peacock, 2014). A nearly perfect alignment of the crystallized chains along the fiber axis and the parallel arrangement of the crystal lamellae relative to the same axis define the final fiber structure (Peterlin, 1971). Moreover, plastically deforming HDPE develops three important types of texture, resembling that of a large quasi-single crystal (Argon, 2013):

1. crystallographic texture due to preferential orientation of crystallographic axes in the crystalline lamellae;

2. morphological texture due to preferential orientation of the normals to the broad faces of the crystalline lamellae faces;

3. macromolecular texture in the amorphous component, which is promoted by the alignment of molecules in the direction of maximum stretch.

For materials such as PET, in which the crystalline and amorphous components are intermixed, the most noticeable effect may be strain-induced crystallization due to macromolecular texture, as described above (Ward and Sweeney, 2004). More specifically, temperatures above the glass transition temperature, a linear structure, and large deformations increase the crystallinity of the material (Ahzi et al., 2003). The crystalline structures produced in this way are oriented, which results in an anisotropic mechanical response. Experiments on polymer film also point to crystallization at lower strain when the strain rate is higher (Rao and Rajagopal, 2001). Most plastic products are manufactured by deforming the material at elevated temperatures to get it into the desired shape. Examples of these operations include film blowing, fiber spinning, and injection molding. In many of these applications, the formation of a highly oriented crystalline phase has a beneficial impact on the mechanical behavior of the material (Dairanieh et al., 1999; Rao and Rajagopal, 2001). Hence, most PET articles are manufactured in this way (Boyce et al., 2000; Rao and Rajagopal, 2001; Makradi et al., 2005).

1.3 Computational framework

All the numerical simulations based on the Finite Element Method (FEM) are held in the in-house Fortran (IBM Mathematical Formula Translation System) program LINKS (Large Strain Implicit Nonlinear Analysis of Solids Linking Scales), a multi-scale finite element code for implicit infinitesimal and finite strain analyses of hyperelastic and elastoplastic solids, that is continuously developed by the CM2S research group (Computational Multi-Scale Modeling of Solids and Structures) at the Faculty of Engineering of University of Porto.

In the present work, the author contributes to the addition of a suitable coupling environment for the partitioned solution of coupled fields and a thermal solver based on the Finite Elements Method. Appropriate nonlinear solvers are also added as implicit solution strategies for the coupled thermomechanical problem.

The numerical simulations concerning the solution of uniaxial traction and compression problems for validating constitutive models are run in an in-house Python program based on the implementation described in Bergström (2015).

The author contributes with two constitutive models to describe the behavior of semi-crystalline polymers.

1.4 Objectives

The main goals of this work are:

- To formulate the thermomechanical problem in a thermodynamically consistent way;

- To provide a thorough overview of the available methods for the solution of coupled problems, in particular, the thermomechanical problem;

- To validate the thermomechanical solver and compare the strongly coupled partitioned strategies available in the literature;

- To thoroughly describe the thermomechanical behavior of semi-crystalline polymers;

- To review the state-of-the-art of semi-crystalline polymer constitutive modeling;

- To implement some of the state-of-the-art constitutive models for semi-crystalline polymers.

1.5   Document structure

The remainder of this document is structured as follows:

Chapter 2 - Thermomechanical problem
This chapter covers the concepts required to describe how a solid responds to thermal and mechanical loads under large deformations, including the conservation laws that guarantee mechanical equilibrium and energy conservation. Additionally, the application of thermodynamics with internal variables is discussed, along with the resulting inferences about the constitutive behavior of the solid material. The implicit partitioned methods to solve the thermomechanical problem are also described.

Chapter 3 - Thermomechanical behavior of semi-crystalline polymers
This chapter attempts to outline the thermomechanical response of semi-crystalline polymers. An account of their deformation mechanisms, experimental results of various mechanical experiments, and an appropriate discussion regarding their dependency on factors such as temperature, strain rate, or pressure is included. This chapter also contains the results of thermal analysis techniques, such as differential scanning calorimetry. An effort is made to provide relevant literature references where the experimental results can be found.

Chapter 4 - State of the art in thermomechanical semi-crystalline polymer constitutive modeling
The main goal of this chapter is to report on the semi-crystalline polymer modeling state of the art. The departure point is infinitesimal thermoviscoelasticity. Nonlinear generalizations are considered by specifying nonlinear laws for the elastic and viscous elements in rheological models originating from infinitesimal viscoelasticity. These are the most commonly available models in the literature, and a detailed overview is provided in this chapter. Following that is a description of models that distinguish between the crystalline and amorphous phases while only considering bulk crystallinity and no additional geometrical information. Finally, multi-scale models with micro and mesostructure considerations are described.

Chapter 5 - Numerical results
This chapter presents two sets of results concerning the thermomechanical modeling of semi-crystalline polymers. The first is adapted from Vila-Chã et al. (2023) and pertains to the implicit partitioned solution of a thermomechanical problem involving nonlinear elastoplastic material behavior. The second pertains to the implementation and validation of two state-of-the-art constitutive models for semi-crystalline polymers.

Chapter 6 - Conclusion and Future Works
This chapter presents the conclusions reached in this work and discusses future research directions.

Chapter 2

Thermomechanical problem

This chapter is adapted from Vila-Chã et al. (2023) and provides a fundamental description of a solid material's response to mechanical and thermal loads in a finite strain setting. It covers the use of thermodynamics with internal variables and the corresponding restrictions on the constitutive description of the material. It also includes a discussion on the methods available in the literature for solving the thermomechanical problem.

2.1   Kinematics of deformation

Let a deformable body $\mathscr{B}$ occupy an open region Ω_0 of the tridimensional Euclidean space $\mathscr{E}$ with a regular boundary $\partial\Omega_0$ in its reference configuration. A smooth one-to-one function defines its motion $\boldsymbol{\varphi} \colon \Omega \times \mathbb{R} \to \mathscr{E}$, mapping each material particle of coordinates $\boldsymbol{X}$ in the reference configuration to its position $\boldsymbol{x}$ in the deformed configuration. Accordingly, the displacement is defined as $\boldsymbol{u} \equiv \boldsymbol{x} - \boldsymbol{X}$. In this work, the finite deformation of the body is described with respect to the initial configuration, following the so-called Lagrangian or material description. The well-known deformation gradient second-order tensor is defined as $\boldsymbol{F}(\boldsymbol{X}, t) \equiv \nabla_0 \boldsymbol{\varphi}(\boldsymbol{X}, t)$, and its determinant, denoted as $J \equiv \det \boldsymbol{F} \geq 0$ represents the local unit volume change. Also relevant to the present work is the spatial velocity gradient $\boldsymbol{L} \equiv \dot{\boldsymbol{F}} \boldsymbol{F}^{-1}$, where $\dot{\boldsymbol{F}}$ denotes the time derivative of the deformation gradient and the dependence of the spatial coordinates and time is omitted.

2.2   Fundamental conservation principles

In continuum thermomechanics, there is a set of conservation principles and thermodynamic laws that, irrespective of the quantities used to describe the mechanical behavior of a body undergoing large deformations, must always be satisfied, namely,

$$\text{div}_0 \, \boldsymbol{P} + \boldsymbol{b}_0 = \rho_0 \ddot{\boldsymbol{u}}, \quad \text{(balance of momentum)}; \tag{2.1}$$

$$\boldsymbol{F}^{-1} \boldsymbol{P} = \boldsymbol{P}^T \boldsymbol{F}^{-T}, \quad \text{(balance of moment of momentum)}; \tag{2.2}$$

$$\rho_0 \dot{e} = \boldsymbol{P} : \dot{\boldsymbol{F}} + \rho_0 r - \text{div}_0 \, \boldsymbol{q}_0, \quad \text{(balance of energy)}; \tag{2.3}$$

$$\rho_0 \dot{s} + \text{div}_0 \left[\frac{\boldsymbol{q}_0}{T} \right] - \frac{\rho_0 r}{T} \geq 0, \quad \text{(entropy production inequality)}, \tag{2.4}$$

where $\boldsymbol{b}_0$ is the body forces field , measured in force per unit undeformed volume; ρ_0 is the material density, measured in mass per unit undeformed volume; $\boldsymbol{P}$ is the first Piola-Kirchhoff stress tensor; e is the internal energy per unit mass; r is the heat supply per unit mass; $\boldsymbol{q}_0$ the first Piola-Kirchhoff heat flux vector, measured in heat power per unit undeformed surface; T is the absolute temperature; and s is specific entropy per unit mass. The second order tensor $\dot{\boldsymbol{F}}$ is the appropriate strain rate measure, such that the double contraction $\boldsymbol{P} : \dot{\boldsymbol{F}}$ represents the stress power per unit volume in the undeformed configuration of the body.

2.3   Thermodynamically consistent constitutive modeling

The stresses and heat fluxes in the governing equations need to be associated with the deformations and temperatures via constitutive laws that represent the physical behavior of the material. For a simple material, the thermodynamic state is assumed to be completely defined by the instantaneous values of a finite number of state variables, i.e., $\{\boldsymbol{F}, T, \boldsymbol{g}_0, \boldsymbol{\alpha}\}$, where $\boldsymbol{g}_0 \equiv \nabla_0 T$ is the material gradient of the temperature and $\boldsymbol{\alpha} \equiv \{\alpha_k\}$ is a set of internal variables, scalar or tensorial, associated with dissipative mechanisms. This approach is included within the so-called rational thermodynamics as developed by Truesdell, Noll, Coleman and others (Noll, 1958; Coleman and Noll, 1961; Coleman and Mizel, 1964). It is a framework broad enough to describe thermodynamically irreversible processes, i.e., processes involving dissipation, thus allowing the modeling of physical phenomena relevant in terms of engineering practice. A thorough review of the different approaches to the thermodynamics of irreversible processes can be found in Lavenda (1978).

The constitutive description of the material must be consistent with the principles established by Equations (2.1)-(2.4), yielding the following constitutive relations

$$\boldsymbol{P} = \rho_0 \frac{\partial \psi}{\partial \boldsymbol{F}}, \tag{2.5}$$

$$s = -\frac{\partial \psi}{\partial T}, \tag{2.6}$$

$$\psi = \psi(\boldsymbol{F}, T, \boldsymbol{\alpha}), \tag{2.7}$$

$$\dot{\boldsymbol{\alpha}} = f(\boldsymbol{F}, T, \boldsymbol{g}_0, \boldsymbol{\alpha}), \tag{2.8}$$

$$\boldsymbol{q}_0 = g(\boldsymbol{F}, T, \boldsymbol{g}_0, \boldsymbol{\alpha}), \tag{2.9}$$

where $\psi \equiv e - Ts$ denotes the Helmholtz free energy. These still need to comply with the second law of thermodynamics, which places constraints on the evolution equations for the internal variables and the constitutive equation for the heat flux.

The development of concrete models that are framed within such a constitutive theory can be achieved by postulating suitable functions for the Helmholtz free energy and other ingredients, such as dissipation potentials and yield surfaces (see Chapter 4 for more details). Regarding the constitutive model for the heat flux, the second law of thermodynamics essentially requires the heat flow to occur in the opposite direction of the temperature gradient. The Fourier heat conduction law for isotropic conduction in the deformed volume is one of the simplest and most popular alternatives, defining the heat flux as

$$\boldsymbol{q}_0 = -k_0 \boldsymbol{C}^{-1} \boldsymbol{g}_0, \tag{2.10}$$

where k_0 is the thermal conductivity and $\boldsymbol{C} = \boldsymbol{F}^T \boldsymbol{F}$ is the right Cauchy-Green strain tensor.

2.4 Heat conduction equation

In the context of thermomechanics, the most common form of the energy balance equation (Equation (2.3)) is the heat conduction equation. Let C_F denote the specific heat at constant deformation , i.e., the amount of heat required to change a unit mass of a substance by one degree in temperature at fixed deformation, defined as

$$C_F \equiv \frac{\partial e}{\partial T}\bigg|_F = -\frac{\partial^2 \psi}{\partial T^2} T = \frac{\partial s}{\partial T} T. \tag{2.11}$$

Taking Equation (2.11), introducing the so-called Gough-Joule effect or thermoelastoplastic heating (or cooling) effect, $\mathscr{H}^{\text{ep}}$, as

$$\mathscr{H}^{\text{ep}} = -\rho_0 T \left(\frac{\partial^2 \psi}{\partial F \partial T} : \dot{F} + \frac{\partial^2 \psi}{\partial \boldsymbol{\alpha} \partial T} * \dot{\boldsymbol{\alpha}} \right), \tag{2.12}$$

and the internal dissipation $\mathscr{D}_{\text{int}}$, given by

$$\mathscr{D}_{\text{int}} = \boldsymbol{P} : \dot{F} - \rho_0 (\dot{\psi} + \dot{T} s), \tag{2.13}$$

the energy balance equation can be recast as

$$\rho_0 C_F \dot{T} = \rho_0 r - \text{div}_0\, \boldsymbol{q}_0 + \mathscr{D}_{\text{int}} + \mathscr{H}^{\text{ep}}. \tag{2.14}$$

2.5 Weak equilibrium and the principle of virtual work

Together with the set of boundary and initial conditions, Equations (2.1) and (2.3) are the so-called strong, point-wise, or local equilibrium equations, as they enforce the balance of momentum and energy at every material particle of the body. The weak form of the linear momentum and energy balance equations can be formulated through the Virtual Work Principle as

$$\int_{\Omega_0} [\boldsymbol{P}(\boldsymbol{F}, T) : \nabla_0 \boldsymbol{\eta} - (\boldsymbol{b}_0(t) - \rho_0 \ddot{\boldsymbol{u}}(t)) \cdot \boldsymbol{\eta}]\, dv - \int_{\partial\Omega_0} (\boldsymbol{P}\boldsymbol{n}_0) \cdot \boldsymbol{\eta}\, da = 0\,, \tag{2.15}$$

$$\int_{\Omega_0} \left[-\boldsymbol{q}_0(\boldsymbol{F}, T) \cdot \nabla_0 \xi - \left(\mathscr{D}_{\text{int}}(\boldsymbol{F}, T) + \mathscr{H}^{\text{ep}}(\boldsymbol{F}, T) + \rho_0 r(t) - \rho_0 C_F \dot{T}(t) \right) \xi \right] dv$$
$$+ \int_{\partial\Omega_0} \boldsymbol{q}_0 \cdot \boldsymbol{n}_0 \xi\, da = 0, \tag{2.16}$$

where, at each point of $\mathscr{B}$, the first Piola-Kirchhoff stress tensor is the solution to the material thermomechanical constitutive initial value problem and the virtual displacements $\boldsymbol{\eta}$ and virtual temperatures ξ satisfy the essential boundary conditions of the problem in a homogeneous sense. The coupling between the mechanical and thermal fields can be understood from a physical point of view as follows:

- the temperature influences the mechanical field through additional thermal stresses and potentially temperature-dependent material properties;

- the mechanical field affects the thermal field through coupling terms which can be interpreted as heat sources (dissipation and thermomechanical structure heating) and through geometric coupling due to the deformation of the domain, which affects boundary conditions and the heat conduction law.

2.6   Finite Element Method

It is now possible to apply the Finite Element Method to the solution of the thermomechanical initial boundary value problem, providing a suitable spatial discretization in a finite element mesh. Defining the global vector of nodal displacements $\mathbf{u}$ and the global vector of nodal temperatures θ as

$$\mathbf{u}(t) = \left[u_1^1(t), \ldots, u_{n_{\dim}}^1(t), \ldots, u_1^{n_{\mathrm{nod}}}(t), \ldots, u_{n_{\dim}}^{n_{\mathrm{nod}}}(t) \right]^T, \tag{2.17}$$

$$\theta(t) = \left[T^1(t), T^2(t), \ldots, T^{n_{\mathrm{nod}}}(t) \right]^T, \tag{2.18}$$

where $n_{\dim}$ denotes the number of spatial dimensions and n_{nod} the total number of nodes in the mesh, the displacement, $\boldsymbol{u}(\boldsymbol{X}, t)$, and temperature, $T(\boldsymbol{X}, t)$, fields defined over the global domain Ω_0 can be approximated at any point $\boldsymbol{X}$ by appropriate interpolation functions. This yields the discretized versions of the momentum and energy balance equations

$$\mathbf{r}_u(\mathbf{u}, \theta, t) \equiv \mathbf{M}\ddot{\mathbf{u}}(t) + \mathbf{f}_u^{\mathrm{int}}(\theta(t), \mathbf{u}(t)) - \mathbf{f}_u^{\mathrm{ext}}(\theta(t), \mathbf{u}(t), t) = \mathbf{0}, \tag{2.19}$$

$$\mathbf{r}_T(\mathbf{u}, \theta, t) \equiv \mathbf{C}\dot{\theta}(t) + \mathbf{f}_T^{\mathrm{int}}(\theta(t), \mathbf{u}(t)) - \mathbf{f}_T^{\mathrm{ext}}(\theta(t), \mathbf{u}(t), t) = \mathbf{0}, \tag{2.20}$$

which are written in residual form, with $\mathbf{r}_u$ the mechanical residual and $\mathbf{r}_T$ the thermal residual, where $\mathbf{f}_u^{\mathrm{int}}$ and $\mathbf{f}_u^{\mathrm{ext}}$ are the mechanical global vectors of internal and external forces, $\mathbf{f}_T^{\mathrm{int}}$ and $\mathbf{f}_T^{\mathrm{ext}}$ are the thermal global vectors of internal and external forces, $\mathbf{M}$ is the mass matrix, and $\mathbf{C}$ is the thermal capacitance matrix. The previous matricial entities are usually obtained by the appropriate assemblage of their elemental counterparts, defined by the corresponding integral quantities.

2.7   Time discretization

In the context of thermomechanical problems, a general path-dependent constitutive model depends on both the instantaneous deformation and temperature states as well as their history. Under these circumstances, for complex deformation, $\boldsymbol{F}(t)$, or temperature paths, $T(t)$, the solution of the constitutive initial value problem for a given set of initial conditions is typically unknown. Therefore, a suitable numerical approach is necessary to integrate the rate constitutive equations, being an implicit backward-Euler scheme adopted in the present contribution.

The space-discrete time-continuous equilibrium equations (Equations (2.19) and (2.20)) can be integrated by employing an adequate and robust time discretization scheme. The fully discrete problem can be written as

$$\mathbf{r}_u^{n+1}(\mathbf{u}_{n+1}, \theta_{n+1}, t_{n+1}) = \mathbf{0} \tag{2.21}$$

$$\mathbf{r}_T^{n+1}(\mathbf{u}_{n+1}, \theta_{n+1}, t_{n+1}) = \mathbf{0}. \tag{2.22}$$

For quasi-static structural problems and steady-state heat flow problems, the temporal integration is fully restrained at the constitutive level, as previously addressed. For transient problems, the Generalised-α method is a popular alternative, which establishes finite-difference approximations of the temporal derivatives and evaluates the equilibrium at generalised midpoints, providing enough freedom to have second-order accuracy, unconditional stability in linear problems and optimal

numerical dissipation in terms of a sole parameter ρ_∞. Unless otherwise stated, the Generalised-α for first-order systems is employed to integrate the transient thermal response (Jansen et al., 2000).

2.8 Solution of the thermomechanical problem

In the present work, implicit partitioned schemes are adopted to solve the thermomechanical problem. The cornerstone of partitioned solution schemes is to solve the thermal and mechanical problems separately, i.e., Equation (2.21) is solved considering a fixed temperature, and Equation (2.22) is solved assuming a fixed configuration. For convenience, consider the existence of two functions, $\mathcal{U}_{n+1}$ and $\mathcal{T}_{n+1}$, that represent these solution procedures at instant t_{n+1}, such that

$$\mathbf{u} = \mathcal{U}_{n+1}(\theta) \rightarrow \text{solve } \mathbf{r}_u^{n+1}(\mathbf{u}, \theta, t_{n+1}) = \mathbf{0} \text{ in order to obtain } \mathbf{u}, \qquad (2.23)$$

$$\theta = \mathcal{T}_{n+1}(\mathbf{u}) \rightarrow \text{solve } \mathbf{r}_T^{n+1}(\mathbf{u}, \theta, t_{n+1}) = \mathbf{0} \text{ in order to obtain } \theta. \qquad (2.24)$$

In the following, the time-step subscripts $(\bullet)_{n+1}$ on the solvers are dropped for notation compactness.

The standard conceptual approach found in the literature for implicit solution schemes is to adopt a fixed-point scheme, such as

$$\theta_*^k = \mathcal{T} \circ \mathcal{U}(\theta^k) \quad \text{or} \quad \mathbf{u}_*^k = \mathcal{U} \circ \mathcal{T}(\mathbf{u}^k), \qquad (2.25)$$

where $\circ$ denotes function composition. The solution found from the fixed-point scheme, θ_*^k or $\mathbf{u}_*^k$ can then be accelerated, i.e.,

$$\theta^{k+1} = \mathcal{A}(\theta_*^k) \quad \text{or} \quad \mathbf{u}^{k+1} = \mathcal{A}(\mathbf{u}_*^k), \qquad (2.26)$$

with $\mathcal{A}$ denoting an appropriate acceleration scheme, which may also use previous iterations. The superscript k denotes the nonlinear iterations performed within each time step.

A slightly different conceptualization of the thermomechanical coupled problem is pursued here. In general, a fixed-point procedure can be transformed into a root-finding problem. In this case, the goal is to define suitable functions, built from $\mathcal{U}$ and $\mathcal{T}$, whose roots are also the solutions to the thermomechanical problem (Equations (2.21) and (2.22)). In the thermomechanical context, the following residual functions are employed

$$\mathcal{R}_J(\mathbf{u}, \theta) = \left\{ \begin{array}{c} \mathbf{u} - \mathcal{U}(\theta) \\ \theta - \mathcal{T}(\mathbf{u}) \end{array} \right\}, \qquad (2.27)$$

and

$$\mathcal{R}_{GS}(\theta) = \theta - \mathcal{T} \circ \mathcal{U}(\theta) \quad \text{or} \quad \mathcal{R}_{GS}^*(\mathbf{u}) = \mathbf{u} - \mathcal{U} \circ \mathcal{T}(\mathbf{u}), \qquad (2.28)$$

where the subscript 'J' stands for Jacobi and the subscript 'GS' for Gauss-Seidel. It should be noted that the residuals, as given here, are the symmetric counterparts of the definitions commonly employed in FSI. The residual $\mathcal{R}_{GS}$ (Equation (2.28)) coinciding with the isothermic split, where the mechanical problem is solved first at a fixed temperature, followed by the solution of the thermal problem at a fixed configuration is employed in the numerical results provided in the present work. Keep in mind that which of the fields is solved first may be critical for the approach's stability and convergence rate. (Joosten et al., 2009).

Since the methods described below for the solution of nonlinear systems of equations apply to both functions $\mathscr{R}_\mathrm{J}$ and $\mathscr{R}_\mathrm{GS}$, a general function denoted as $\mathscr{R}$, whose variable is $\mathbf{x}$, is conveniently adopted in the following discussion.

As previously stated, the solution to the thermomechanical problem (Equations (2.21) and (2.22)) can be conceptually posed as the solution of

$$\mathscr{R}(\mathbf{x}) = 0, \tag{2.29}$$

where $\mathbf{x}$ stands for the appropriate unknowns based on the particular residual (θ or $\mathbf{u}$, see Equation (2.28)). It should be mentioned that unknowns in all mesh nodes must be considered for a volumetric coupling, such as in a thermomechanical problem. This is in contrast with fluid-structure interaction, where just the degrees of freedom at the interface must be taken into account. For completeness, also consider the function

$$\mathscr{S}(\mathbf{x}) = \mathbf{x} - \mathscr{R}(\mathbf{x}), \tag{2.30}$$

whose fixed-point is the solution to the nonlinear equation system in Equation (2.29). Therefore, a broad class of standard implicit methods available in the literature can be applied to solve the problem at hand, allowing the use of appropriate libraries when available. The accelerated fixed-point counterparts can also be properly identified, as shown in the remainder of this section.

In the present work, the criteria used for the choice of the most suitable implicit methods are similar to the ones provided by Fang and Saad (Fang and Saad, 2009) in the context of electronic structure problems. These can be summarized as follows:

1. The dimensionality of the problem is large;

2. $\mathscr{R}$ is continuously differentiable, but the analytical form of its derivative is not readily available or is computationally expensive to compute;

3. The evaluation of $\mathscr{R}(\mathbf{x})$ is computationally demanding;

4. The problem is noisy, i.e., the computed function values of $\mathscr{R}$ usually contain errors.

Attending to the previous criteria, the most suitable methods should comply with the following desirable features: it must minimize the number of calls to $\mathscr{R}$, as it is expensive to compute; the amount of information saved from previous iterations must be judiciously chosen as the problem's dimensionality is large; and it cannot require the analytical derivative of $\mathscr{R}$, since it is not available.

Remark. To clarify, each appearance of $\mathscr{R}(\bullet)$ in the formulas entails new calls to the mechanical solver, thermal solver, and data communication according to its particular definition.

2.8.1 Fixed-point

The application of the fixed-point method to obtain the roots of $\mathscr{R}$ yields

$$\mathbf{x}^{k+1} = \mathscr{S}(\mathbf{x}^k) = \mathbf{x}^k - \mathscr{R}(\mathbf{x}^k). \tag{2.31}$$

If the particular functions defined in Equations (2.27) and (2.28) are used, one finds the two basic Schwarz procedures commonly employed in partitioned implicit solution

procedures (Uekermann et al., 2013; Danowski, 2014; Gatzhammer, 2014). They are the additive or block Jacobi and the parallel Scharwz or Gauss-Seidel procedures. The names originate from domain decomposition, and justify the subscripts employed in Equations (2.27) and (2.28).

This approach necessitates only one residual evaluation per nonlinear iteration, with no previous iterations being required. Its computational complexity scales linearly with the number of unknowns, and it is the simplest method to implement.

2.8.2 Constant underrelaxation

One of the most straightforward ways to stabilize an iterative method is to use constant underrelaxation (see, e.g., Erbts and Düster (2012) or Gatzhammer (2014)). The relaxation is performed as follows

$$\mathbf{x}^{k+1} = (1 - \omega)\mathbf{x}^k + \omega \mathcal{S}(\mathbf{x}^k) = \mathbf{x}^k - \omega \mathcal{R}(\mathbf{x}^k), \qquad (2.32)$$

where ω is the relaxation factor chosen in the range $0 < \omega < 1$, which corresponds to an underrelaxation, to achieve a stabilizing effect.

Constant underrelaxation works well if ω is close to 1 but leads to a slow convergence if ω has to be chosen close to 0. Thus, the constant underrelaxation method creates unmanageable computational costs for severe instabilities. Overrelaxation can also be considered, keeping in mind that for $\omega > 2$, convergence is lost. The optimal ω is not necessarily the largest stable one (Gatzhammer, 2014) and has to be set empirically. In what follows, alternative methods are discussed to decrease the number of iterations necessary while maintaining stability.

The number of residual evaluations, memory requirements, and computation complexity equals the ones displayed by the fixed-point approach. Compared to the last approach, the increase in complexity is negligible.

2.8.3 Aitken relaxation

The so-called Aitken Δ^2 relaxation method was introduced by Irons and Tuck (Irons and Tuck, 1969) as a modified Aitken Δ^2 that does not require the computation of the function twice per iteration as in the original method [1]. It has been widely used in the context of FSI (Irons and Tuck, 1969; Küttler and Wall, 2008; Joosten et al., 2009; Küttler and Wall, 2009) and also in thermomechanics (see, e.g.,Erbts and Düster (2012); Danowski (2014); Erbts et al. (2015); Wendt et al. (2015)).

In the one-dimensional case, this method resembles the secant method applied to the fixed point problem, which can be used to solve nonlinear equations without differentiation. This version of Aitken's Δ^2 method provides a dynamic relaxation parameter, which can be used to improve the convergence/stability properties of the coupling algorithm.

The solution to the current iteration from the outcome of the previous iteration $\mathbf{x}^k$ plus a new increment $\Delta \mathbf{x}^k$ is found from

$$\mathbf{x}^{k+1} = \mathbf{x}^k + \Delta \mathbf{x}^k. \qquad (2.33)$$

---

[1]The use of the Aitken-Δ^2 process to solve nonlinear equations leads to Steffenson's method. There are also generalizations of the Aitken-Δ^2 process to the vector case (Sidi, 2017). Both lead, however, to schemes where the residual is evaluated twice per nonlinear iteration.

The increment reads

$$\Delta \mathbf{x}^k = \omega^k \left(\mathscr{S}(\mathbf{x}^{(k)}) - \mathbf{x}^{(k)} \right) = -\omega^k \mathscr{R}(\mathbf{x}^k), \tag{2.34}$$

with ω^k being the relaxation coefficient. This coefficient is updated at every iteration cycle as a function of two previous residuals,

$$\omega^k = -\omega^{k-1} \frac{\left(\mathscr{R}(\mathbf{x}^k) - \mathscr{R}(\mathbf{x}^{k-1}) \right)^{\mathrm{T}} \mathscr{R}(\mathbf{x}^{k-1})}{\left(\mathscr{R}(\mathbf{x}^k) - \mathscr{R}(\mathbf{x}^{k-1}) \right)^2}. \tag{2.35}$$

The dynamical relaxation coefficient is restricted to the range $(0,2)$ because employing a relaxation coefficient outside this range leads to a loss of convergence (Erbts and Düster, 2012). For the first nonlinear iteration, an initial value for the relaxation coefficient must be specified. If $\omega^0 = 1$ is chosen, the result will be a fixed-point iteration, then followed by dynamic relaxation.

This approach is also easy to implement, and the additional computational input is acceptable since only inner vector products must be performed. It only requires a residual evaluation per iteration and the residual value of the previous iteration.

2.8.4 Newton-Krylov methods

The Newton-Raphson or Newton scheme is a very popular iterative solution procedure for nonlinear systems of equations. When certain mathematical conditions are met, this scheme converges quadratically. It can be applied to Equation (2.29), yielding

$$\mathbf{J}_{\mathscr{R}(\mathbf{x}^k)} \Delta \mathbf{x}^k = -\mathscr{R}(\mathbf{x}^k), \tag{2.36}$$

$$\mathbf{x}^{k+1} = \mathbf{x}^k + \Delta \mathbf{x}^k. \tag{2.37}$$

Every iteration of the Newton scheme involves at least one invocation of the thermal and mechanical solvers when computing $\mathscr{R}\left(\mathbf{x}^k\right)$. The critical point for black-box equation coupling is obtaining the derivative information in the Jacobian matrix, which is not readily available.

One possibility to bypass the need for $\mathbf{J}_{\mathscr{R}}$ is by employing Newton-Krylov methods, which seek the solution of the Newton system of equations in Equation (2.36) using Krylov methods, such as the generalized minimal residual method (GMRES) or the biconjugate gradient stabilized method (BiCGSTAB). The Krylov iterative methods approximate the solution of a linear system $\mathbf{Az} = \mathbf{b}$ using the Krylov subspace

$$\mathcal{K}_m = \mathrm{span}\{\mathbf{r}_0, \mathbf{A}\mathbf{r}_0, \mathbf{A}^2\mathbf{r}_0, \dots, \mathbf{A}^{m-1}\mathbf{r}_0\}, \tag{2.38}$$

such that the m-th iterate $\mathbf{z}_m \in \mathcal{K}_m$, with $\mathbf{r}_0 = \mathbf{b} - \mathbf{A}\mathbf{z}_0$. The precise way in which $\mathbf{z}_m$ is built is what distinguishes the different methods. To generate the appropriate Krylov subspace, one needs the product $\mathbf{J}_{\mathscr{R}}(\mathbf{x}^k)\mathbf{y}$ in Equation (2.36), for some vector $\mathbf{y}$. It is assumed that the Jacobian is unavailable, so it must be approximated. Also, it would be beneficial if the full Jacobian is neither computed in its entirety nor fully stored in memory, i.e., a matrix-free method is desirable. Although the matrix of coefficients $\mathbf{A} = \mathbf{J}_{\mathscr{R}}$ is unknown, it is possible to exploit the fact that $\mathbf{A}$ is a Jacobian matrix, such that the Jacobian-vector product can be approximated with a numerical forward difference directional derivative (Kelley, 2003b).

Since the present use case includes many unknowns, it leads to memory concerns if the Krylov subspace is allowed to grow indefinitely. A restarted version where the maximum size of the Krylov space is restricted to p elements is preferred. Once this number is reached, the procedure is restarted. However, the convergence can be poor if p is small. The so-called restarted GMRES is denoted as GMRES(p), with p being the maximum number of previous iterations in memory. Further details on Newton-Krylov methods can be found in Kelley (2003b).

In each nonlinear iteration of the Newton-Krylov method, the number of iterations inside the Krylov subspace solver can be large, and each iteration requires an evaluation of the residual. This number of residual evaluations can be a significant drawback when the evalution of $\mathscr{R}$ is expensive. This problem is, however, mitigated by the fact that the linear system in Newton's method is only solved until it satisfies

$$\|\mathbf{J}_{\mathscr{R}}(\mathbf{x}^k)\Delta\mathbf{x}_m^* + \mathscr{R}(\mathbf{x}^k)\| \leq \eta\|\mathscr{R}(\mathbf{x}^k)\|, \tag{2.39}$$

where η is called the forcing term, and it is chosen to avoid over-solving the Newton system (Equation (2.36))— the linear system is solved to an error that does not influence the error in the nonlinear solution procedure. As a simple approach, Kelley (Kelley, 2003b) suggests using a fixed value for the forcing term, e.g., $\eta = 0.1$. However, according to the same author there are more sophisticated ways to choose this parameter, such as the Eisenstat-Walker method. The smaller the forcing term η, the closer one gets to the standard Newton method. However, especially in the first nonlinear iterations, choosing a η that is too small leads to unnecessarily long computational times since the error in the Newton iterations supersedes the error in the solution of the linear system.

2.8.5   Broyden-like class

Both the generalized Broyden's family, including Broyden's method, and Anderson's mixing can be understood as methods in the Broyden-like class as described in Fang and Saad (2009). They are multisecant quasi-Newton methods which rely on the Newton update and build approximations to the Jacobian or to its inverse.

Suppose the latest m iterates of the nonlinear solution sequence is available, which are denoted by $\mathbf{x}^1,\ldots,\mathbf{x}^m$. Let $\Delta\mathbf{x}^i = \mathbf{x}^{i+1} - \mathbf{x}^i$ for $i = 1,\ldots,m-1$. The $m-1$ step vectors, $\Delta\mathbf{x}^1,\ldots,\Delta\mathbf{x}^{m-1}$, are partitioned into p groups,

$$\mathbf{X}^1 = \left[\Delta\mathbf{x}^1,\ldots,\Delta\mathbf{x}^{z_1}\right], \tag{2.40}$$

$$\mathbf{X}^2 = \left[\Delta\mathbf{x}^{z_1+1},\ldots,\Delta\mathbf{x}^{z_2}\right], \tag{2.41}$$

$$\vdots \tag{2.42}$$

$$\mathbf{X}^p = \left[\Delta\mathbf{x}^{z_{p-1}+1},\ldots,\Delta\mathbf{x}^{z_p}\right], \tag{2.43}$$

where z_i is the index of the last entry in the i-th group for $i = 1,\ldots,p$, meaning that $z_0 = 0$ and $z_p = m-1$. Also partition $\Delta\mathscr{R}^1,\ldots,\Delta\mathscr{R}^{m-1}$ into $\mathbf{R}^1,\ldots,\mathbf{R}^p$ accordingly, where $\Delta\mathscr{R}^i = \mathscr{R}^{i+1} - \mathscr{R}^i$ with $\mathscr{R}^i = \mathscr{R}(\mathbf{x}^i)$. The sizes of the groups for $i = 1,\ldots,p$ are denoted by $s_i \equiv z_i - z_{i-1}$. For a generic iteration $k \in [z_{i-1} + 1, z_i]$ inside group i, the inverse of the Jacobian, $\mathbf{G}_{\mathscr{R}} \equiv \mathbf{J}_{\mathscr{R}}^{-1}$, is approximated as

$$\mathbf{G}_{\mathscr{R}}^k = \mathbf{G}_{\mathscr{R}}^{z_{i-1}} + \left(\mathbf{X}^{i-1} - \mathbf{G}_{\mathscr{R}}^{z_{i-1}}\mathbf{R}^{i-1}\right)\mathbf{V}^{i-1^T}, \tag{2.44}$$

where $\mathbf{V}^{j\,T}\mathbf{R}^j = \mathbf{I}$ for the multi-secant condition

$$\mathbf{G}_{\mathcal{R}}^{z_j+1}\mathbf{R}^j = \mathbf{X}^j, \tag{2.45}$$

to be satisfied. The two optimal choices of $\mathbf{V}^{j\,T} = \mathbf{M}^{j\,-1}\mathbf{N}^{j\,T}$ are

$$\text{Type I:} \qquad \mathbf{M}^j = \mathbf{X}^{j\,T}\mathbf{G}_{\mathcal{R}}^j\mathbf{R}^j, \qquad \mathbf{N}^{j\,T} = \mathbf{X}^{j\,T}\mathbf{G}_{\mathcal{R}}^j, \tag{2.46}$$

$$\text{Type II:} \qquad \mathbf{M}^j = \mathbf{R}^{j\,T}\mathbf{R}^j, \qquad \mathbf{N}^{j\,T} = \mathbf{R}^{j\,T}. \tag{2.47}$$

The next iterate is set as

$$\mathbf{x}^{k+1} = \mathbf{x}^k - \mathbf{G}_{\mathcal{R}}^k\mathcal{R}^k. \tag{2.48}$$

One still needs the initial approximation to the inverse of the Jacobian, $\mathbf{G}_{\mathcal{R}}^1$, whose size is $N \times N$. In Fang and Saad (2009), the approach adopted was to follow the idea of Anderson's mixing and set

$$\mathbf{G}_{\mathcal{R}}^0 = -\beta\mathbf{I}, \tag{2.49}$$

drastically improving the memory requirements, as only one scalar parameter, β, needs to be saved. Also, Kelley (Kelley, 2003b) assumes, in his implementation of Broyden's method, an initial approximation to $\mathbf{G}_{\mathcal{R}}^0$ equal to the identity matrix. Information about $\mathbf{G}_{\mathcal{R}}^0$ is applied in the preconditioning of the system instead.

To clarify the procedure behind the previous expressions, the whole process departs from the initial estimate of the inverse of the Jacobian, given by Equation (2.49). The Newton-update (Equation (2.48)) is repeated $s_1 = z_1 - 0$ times with a constant Jacobian ($\mathbf{G}_{\mathcal{R}}^0$). At the beginning of iteration $k = z_1 + 1$, when the first group ($i = 1$) is finalised and the second group ($i = 2$) starts, the inverse of the Jacobian is updated with the s_i previous steps using Equation (2.44). Then, the Newton iterations are performed $s_2 = z_2 - z_1$ times with constant Jacobian $\mathbf{G}_{\mathcal{R}}^{z_1+1}$ and the process repeats over time until convergence is achieved. It is also common for the sizes of the p groups to be equal, i.e., $s_i = s$, for $i = 1, \ldots, m$.

Broyden's method   Broyden's method (Broyden, 1965) with the identity matrix as the initial guess for the inverse of the Jacobian corresponds to using a group size equal to one, $s = 1$, $\beta = -1$, and enforcing the secant condition according to Equation (2.46), referring only to the previous two iterations.

Regarding memory availability, the iteration can be restarted if there is no more room to store the vectors (Kelley, 2003a). A different approach, called limited memory in the optimization literature, replaces the oldest stored iterations with the most recent ones.

A set of practical considerations must be taken into account and can be found in Fang and Saad (2009). These lead to a storage need of

1. Two column vectors of size N for $\mathbf{x}^m$ and $\mathcal{R}^m$.

2. An $N \times (m-1)$ matrix for $\mathbf{X}^1, \ldots, \mathbf{X}^k$.

3. An $N \times (m-1)$ matrix for $\mathbf{R}^1, \ldots, \mathbf{R}^k$.

4. For Type-I update, the last group $\mathbf{N}^k$ is also stored since its computation involves $\mathbf{G}_{\mathcal{R}}^k$.

and for each update of the inverse of the Jacobian, the computational cost is $\mathcal{O}(Nm^2)$, due to the QR decomposition of an $N \times m$ matrix needed in the computation of $\mathbf{V}^{j\,T}$ (see Equations (2.46) and (2.47)). Kelley (Kelley, 2003b) presents an implementation for Broyden's method that halves the memory requirement relative to the one presented in Fang and Saad (2009).

Fang and Saad (Fang and Saad, 2009) also employ a simple restarting procedure. If in two consecutive values of $\mathcal{R}$, $\mathcal{R}_{\text{old}}$ and $\mathcal{R}_{\text{new}}$, $\|\mathcal{R}_{\text{new}}\|$ is much larger than $\|\mathcal{R}_{\text{old}}\|$, the solution procedure is restarted, with the new initial trial values corresponding to $\mathcal{R}_{\text{old}}$. They suggest r between 0.1 and 0.3, with $\|\mathcal{R}_{\text{old}}\| < r\|\mathcal{R}_{\text{new}}\|$ leading to a restart. This approach is not used here as there is evidence that these methods perform well without it in the thermomechanical problems studied.

In the context of FSI The multi-secant quasi-Newton methods have been used in the context of FSI, e.g., the interface block quasi-Newton method with least-squares approximation (IBQN-LS) (Vierendeels et al., 2007) and the Interface Quasi-Newton technique with an approximation for the Inverse of the Jacobian from a Least-Squares model (IQN-ILS) (Degroote et al., 2009), which fit into the framework presented above. For more detailed treatments see, e.g., Haelterman et al. (2009); Gatzhammer (2014); Uekermann (2016); Scheufele (2018).

2.8.6 Vector extrapolation techniques in cycling mode

There is vast literature on sequence acceleration/extrapolation methods (see Brezinski and Zaglia (2013) and Sidi (2017) for textbook treatments of this topic). Perhaps the most well-known acceleration method is the Aitken Δ^2 process, which has been mentioned in Section 2.8.3, due to its popularity and inherent simplicity. They are based on the very natural idea of extrapolation. According to Brezinski and Zaglia (2013), there is a strong connection between sequence transformations and fixed point methods for solving $x = g(x)$, $g: \mathbb{R} \to \mathbb{R}$. The most well-known example of this connection is that between Aitken's Δ^2 process and Steffensen's method.

Turning to vector sequences and systems of nonlinear equations, let F be a vector extrapolation method which takes the last $q + 2$ vectors of $(\mathbf{w}^0, ..., \mathbf{w}^{p+q+1})$ computed from the sequence $\{\mathbf{w}\}^i$ and computes the extrapolated value as

$$\mathbf{s}_{p,q} = F\left(\mathbf{w}^p, \ldots, \mathbf{w}^{p+q+1}\right), \tag{2.50}$$

with $p \geq 0$ and $q \geq 1$. For solving the fixed point problem $\mathbf{x} = \mathscr{S}(\mathbf{x})$, one can associate the iterative method F such that the k-th iteration of the nonlinear solution sequence is given by

$$\mathbf{x}^{k+1} = F\left(\mathscr{S}^p(\mathbf{x}^k), \ldots, \mathscr{S}^{p+q+1}(\mathbf{x}^k)\right), \tag{2.51}$$

where $\mathscr{S}^{i+1}(\mathbf{x}) = \mathscr{S} \circ \mathscr{S}^i(\mathbf{x})$ and $\mathscr{S}^0(\mathbf{x}) = \mathbf{x}$. This approach is called full cycling or simply cycling. Essentially, for each nonlinear iteration the fixed-point is applied p times in a recursive manner, and the last $q + 1$ of this sequence is used to perform the extrapolation.

Vector extrapolation methods are classified into two types: polynomial methods and methods based on the ϵ-algorithm (Brezinski and Zaglia, 2013; Sidi, 2017). In what follows, only the first category is considered since the second requires a relatively large number of function evaluations per iteration. Sidi (Sidi, 2017) presents four different

polynomial extrapolation methods, that attempt to express the limit of the vector sequence as a linear combination of $q + 1$ iterates,

$$\mathbf{x}^{k+1} = \sum_{j=0}^{q} \gamma_j \mathscr{S}^{p+j}(\mathbf{x}^k) = \sum_{j=0}^{q} \gamma_j \mathbf{w}^{p+j}, \tag{2.52}$$

where the notation shorthand $\mathbf{w}^i = \mathscr{S}^i(\mathbf{x}^k)$ has been introduced. It should be remarked that although the linear combination is performed over $q + 1$ vectors, the previously mentioned $q + 2$ vectors are still used in the computation of the coefficients γ_j. The methods considered in the present work are the minimal polynomial extrapolation (MPE) and the reduced rank extrapolation (RRE).

MPE   Solve the overdetermined linear system $\mathscr{W}^{q-1}\mathbf{c}' = -\Delta\mathbf{w}^{p+q}$ in the least-squares sense for $\mathbf{c}' = \left[c_0, c_1, \ldots, c_{q-1}\right]^T$, where $\mathbf{W}^{q-1} = [\Delta\mathbf{w}^p, \ldots, \Delta\mathbf{w}^{p+q-1}]$ and $\Delta\mathbf{w}^i = \mathbf{w}^{i+1} - \mathbf{w}^i$. With $c_0, c_1, \ldots, c_{q-1}$ available, set $c_q = 1$ and compute $\gamma_j = c_j / \sum_{i=0}^{q} c_i, j = 0, 1, \ldots, q$, provided $\sum_{j=0}^{q} c_j \neq 0$.

RRE   Solve the overdetermined linear system $\mathbf{W}^q\boldsymbol{\gamma} = 0$ in the least-squares sense, subject to the constraint $\sum_{j=0}^{q} \gamma_j = 1$, where $\boldsymbol{\gamma} = [\gamma_0, \ldots, \gamma_q]$.

For a combination (p, q), the required number of residual evaluations per nonlinear iteration is $p + q + 1$. In making sensible management of memory, only a constant $q + 2$ vectors must be stored in memory. To solve the least-squares problems defining the MPE and the RRE can be achieved by employing a QR decomposition, whose computational cost is $\mathcal{O}(Nq^2)$ (Sidi, 2017).

Chapter 3

Thermomechanical behavior of semi-crystalline polymers

The goal of this chapter is to outline the thermomechanical response of semi-crystalline polymers. An account of their deformation mechanisms opens the chapter, followed by the experimental results of various mechanical experiments, such as constant strain rate, stress relaxation, and creep tests. A discussion regarding their dependency on factors such as temperature, strain rate, and pressure is also included. Closing the chapter are the results of thermal analysis techniques, such as differential scanning calorimetry.

An effort is made to provide relevant literature references where the experimental results can be found.Some of them are later used in the validation and comparison of the various models available in the literature.

3.1 Deformation mechanisms for semi-crystalline polymers

A deformation mechanism is a kinetic process occurring at the atomic, microscopic, or mesoscopic scale that is responsible for changes in a material's internal structure, shape, or volume, thus implying a characteristic deformation behavior, i.e., a constitutive relation between stress, strain, strain rate, and temperature (Frost and Ashby, 1982). According to Arzhakov (Arzhakov, 2019), it includes

1. molecular-kinetic aspects, such as the mutual torsional-vibrational and translational motions of microscopic kinetic units of various sizes,

2. structural aspects, such as the creation or annihilation of kinetic units or changes in the resistance to their motion,

where a kinetic unit is a structural element possessing vibrational and translational degrees of freedom. As a rule of thumb, the molecular-kinetic aspects by themselves describe a steady state, such that the stress and the temperature determine completely the strain rate and other variables describing the structure of the material. The structural aspects will lead to a transient behavior, meaning that the stress and the

temperature will not be enough to determine the response of the material since the structure is also changing (Frost and Ashby, 1982).

One way to study the deformation mechanisms in a polymer is to consider its relaxation transitions. A relaxation transition is a change in the material's response to an external action caused by the mobility of a specific kinetic unit in a given temperature-time test mode. However, irreversible deformation or structure change is allowed (Arzhakov, 2019). The experimental approaches and techniques used to study relaxation phenomena are extremely diverse, including isochronal (considering the response at the same instant or frequency) and isothermic results from experiments such as thermomechanical analysis, differential scanning calorimetry (DSC) (reviewed in more detail below), dielectric and acoustic measurements, radiothermoluminescence, nuclear magnetic resonance, and several modifications of probing techniques. (Ferry, 1980; Arzhakov, 2019).

Despite the partially ordered structure of the crystalline phase and the corresponding limitation of molecular mobility, the relaxation spectrum of a semi-crystalline polymer is generally richer than that of a glassy polymer. The kinetic units in the former can be made to correspond to features inside crystallites, in the intercrystalline amorphous region, or on the surface of the crystallites (Ferry, 1980; Arzhakov, 2019).

The assignment of a given relaxation transition to a deformation mechanism within a phase of the semi-crystalline polymer can be achieved in two ways: (i) by considering the same polymer at different degrees of crystallinity, lamellar thicknesses, defect content, cross-linking; (Ferry, 1980), and (ii) by employing an etching procedure (Arzhakov, 2019). Hoffman and coworkers (Hoffman et al., 2007), when discussing the relaxation behavior of polycholorotrifluoroethylene (PCTFE) and polyethylene (PE) , describe deformation mechanisms such as the motion of chain folds coupled with interior chains and relaxation at chain-end induced row vacancies in chain-folded crystals. The relaxation behavior of semi-crystalline polymers is discussed later with thermomechanical experiments as a basis, both isotermic and isochronal. Some of the kinetic units involved in a semi-crystalline polymer's deformation mechanisms are (Arzhakov, 2019) (see Figure 3.1):

1. between the crystalline cores of the lamellae;

2. regular folds with suppressed mobility;

3. irregular loops;

4. folded tie-chains;

5. free ends of macromolecules coming out of lamellae;

6. slightly curved tie-chains;

7. folds the mobility of which is significantly limited by crystallites;

8. fully straightened tie-chains, the ends of which are fixed by neighboring lamellas.

Bowden and Young (Bowden and Young, 1974) provide an early description of the deformation mechanisms in a semi-crystalline polymer not associated with relaxation transitions. These may include structural changes and lead to permanent deformation. Drozdov and coworkers (Drozdov et al., 2009) provide a fairly comprehensive list of such microstructural changes.   In the amorphous phase, orientation of
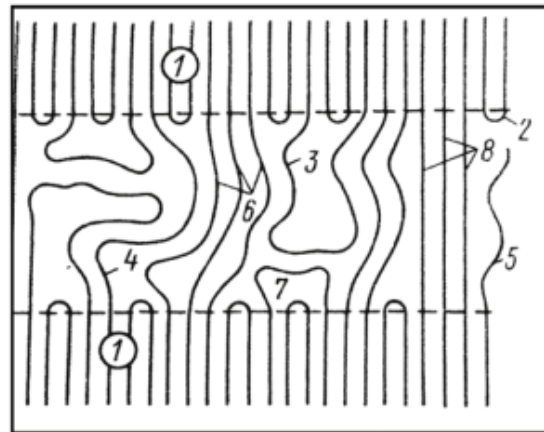
Figure 3.1: Schematic depiction of the kinetic units associated with relaxation transitions in lamellar PE. 1) between the crystalline cores of the lamellae; 2) regular folds with suppressed mobility; 3) irregular loops; 4) folded tie-chains; 5) free ends of macromolecules coming out of lamellas; 6) slightly curved tie-chains; 7) folds the mobility of which is significantly limited by crystallites; 8) fully straightened tie-chains, the ends of which are fixed by neighboring lamellas. Taken from Arzhakov (2019).

macromolecules along the direction of maximum stress can be observed, as can changes in the concentration of entanglements between chains (junctions in the polymer network), and the formation and growth of micro-voids. In the crystalline phase, there can be formation and motion of dislocations in the crystallites, rotation and twist of lamellae in spherulites, fine (homogeneous shear of crystal blocks) and coarse (heterogeneous inter-lamellar sliding) slip of lamellar blocks and their fragmentation, micro-necking of lamellae, rotation of lamellar stacks, or rearrangement of the spherulitic structure into a fibrilar structure, among others. At the interface between the amorphous and crystalline phases, phenomena such as chain slip through the crystals, sliding of tie chains and detachment of chain folds and loops from lamellar block surfaces, diffusion of micro-voids from the amorphous into the crystalline phase, and creation and annihilation of dislocations at lamellae surfaces can all be observed.

Based on several works, including Peterson (1966) and Lin and Argon (1994), Argon (Argon, 2013) identifies three different interlamellar slip deformation mechanisms in semi-crystalline polymer crystallites: nucleation of a monolithic screw dislocation from the thin edge of the lamella into the (100) plane; nucleation of a screw dislocation half loop from the narrow edge; and nucleation of an edge-dislocation half loop from the large flat surface of the wide face of a lamella.

Relevant to the behavior of the amorphous phase, Boyce and coworkers (Boyce et al., 1988) mention that, for glassy polymers, flow is only observed after the segments of the polymer molecules undergo a sufficient rotation. It follows the molecular alignment of the polymer chains, resulting in entropy change and increased resistance to the loading.

The nature of the deformation associated with each of these mechanisms must be discussed, i.e., whether it is elastic or plastic, reversible or irreversible. After all, if they lead to flow, it may appear at first glance that the corresponding deformation is always

permanent. Consider this simplified picture: Add a schematic the mechanisms are parallel combinations of dashpots and springs in series, as described in Keller and Pope (1971). The differences in the viscosity and stiffness of the springs in this model allow for both permanent deformation and recovery (Fotheringham and Cherry, 1978). Some of the mechanisms may remain elastic, when the viscosity of the corresponding dashpot is very large, and even allow for complete recovery. Physically, it means that the kinetic units responsible for a given flow mechanism may be components of a composite overall structural element whose behavior remains elastic. Even intralamellar slip in the crystalline part of a semi-crystalline polymer can show some recovery due to the polymer crystallite structure, e.g., when the slip planes cut across fold planes (Keller and Pope, 1971). The decomposition of deformation into reversible and irreversible parts is discussed based on mechanical experiments in Section 3.2.3.

Regarding the modeling of the deformation behavior connected to each of these phenomena, some of them accept numerically feasible descriptions, e.g., the plastic flow rule corresponding to the nucleation of dislocation in the crystalline part of the polymer or the strain hardening due to the molecular alignment of the amorphous part of the polymer. However, there are some hurdles to the practical application of these models. Since semi-crystalline polymers are heterogeneous and hierarchical in structure, the descriptions of the deformation mechanisms may not be directly applicable to the bulk material. Also, the structure of the material changes with deformation, as does the relative importance of each mechanism in the overall deformation behavior. More details on some of these models are provided in Chapter 4.

To better understand how the micro- and mesostructure evolve with mechanical loading, consider the split of the stress-strain curve proposed by Strobl and coworkers (Hiss et al., 1999; Hobeika et al., 2000; Hong et al., 2004a,b; Na et al., 2006). It is based on free shrinkage and step-cycle tests, as well as x-ray scattering experiments on deformed samples. The results were obtained for PEs with different degrees of crystallinity and molecular weight above the glass transition temperature.

At small strains, below a true strain of approximately 0.025, deformation manifests itself mainly through the soft amorphous layers (Patlazhan and Remond, 2012). In fact, according to Nikolov and coworkers (Nikolov and Doghri, 2000; Nikolov et al., 2002), experiments show that interlamellar shear is the dominant deformation mode at small strains for PE. The onset of local flow processes at the end of the Hookean range through isolated slip processes begins at around a true strain of 0.025 (Hiss et al., 1999). Taking into account that local stresses in two-phase heterogeneous solids may strongly exceed the imposed stress, plastic flow of crystal lamellae may appear locally at fairly low strains (Patlazhan and Remond, 2012). A collective onset of sliding processes among the crystal blocks composing the crystal lamellae determines the yield point (point B in Figure 3.2), at around a true strain of 0.1. The beginning of the disintegration of the crystal blocks, which is followed by fibril formation (point C in Figure 3.2) starts at around a strain of 0.6. Solid-state deformation of a semi-crystalline polymer normally results in the destruction of the crystallites belonging to the original morphology, followed by reordering to form new crystallites. Newly formed crystallites are themselves subject to disruption at higher orientation levels, being replaced by a fibrillar morphology (Peacock, 2014). According to G'Sell (G'sell and Dahoun, 1994), it is conceivable that the crystallites begin to undergo fragmentation and unfolding at strains between 0.5 and 1.0. Chain disentanglement (point D in Figure 3.2) happens at around a true strain of 1.
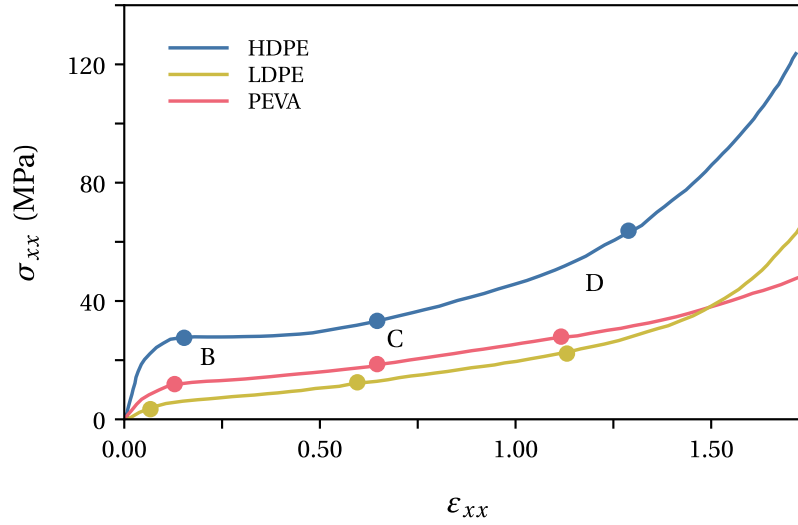
Figure 3.2: Locations of the transition points B-D along the stress-strain curve for HDPE, LDPE and PEVA. Adapted from Hiss et al. (1999).

3.2   Mechanical response of semi-crystalline polymers

The thermomechanical response of semi-crystalline polymers is reviewed in this section with the aim of identifying relevant features for constitutive modeling (see Chapter 4 and 5). There are several factors affecting the mechanical response of semi-crystalline polymers. Extrinsic factors, such as temperature, strain rate, hydrostatic pressure, and the chemical nature of the environment (e.g., the presence of water, oxygen, and organic solvents), are critical in describing the behavior of a polymer. Other relevant elements in the characterization of semi-crystalline polymers are intrinsic. Of crucial importance are the degree of crystallinity, lamellar thickness, mesoscopic structure, molecular weight, physical entanglement, cross-linking, and polymer aging (Ayoub et al., 2011; Şerban et al., 2013; Callister and Rethwisch, 2014; Cundiff et al., 2022).

Numerous experimental procedures provide information about a material's mechanical response. Constant strain rate tests are among the most relevant experiments for the characterization of semi-crystalline polymers, mainly through uniaxial loading experiments, whether tensile or compressive. Pure shear and torsion tests are also often employed. Stress relaxation, creep experiments, and dynamic mechanical analysis are useful tests as well, highlighting the time-dependent response of the material. The polymer's behavior upon unloading must also be considered, using step-cycle and free-shrinkage tests. The data from these last two experiments is critical in identifying irreversible deformation in semi-crystalline polymers, which is less easily defined at room temperature than in most metals. The impact of the previously mentioned factors, such as temperature, strain rate, and hydrostatic pressure, on the mechanical response of the polymer in each type of experiment is thoroughly discussed in the subsequent paragraphs.

3.2.1   Constant strain rate loading

The mechanical response of a semi-crystalline polymer in a constant strain rate experiment is determined by several factors. However, in the typical conditions of most applications, they exhibit the behavior of a plastic polymer. These polymers exhibit structural rigidity under load and are suitable for general-purpose applications. To be included in this material class, a polymer must be possess a linear or branched structure. In addition, if amorphous, it must be used below its glass transition temperature, T_g, supposed to be in the range from $100\,°C$ to $400\,°C$ and much higher than their service temperature, T_{ser}. If semi-crystalline, the temperature should not exceed its melting temperature (Callister and Rethwisch, 2014; Arzhakov, 2019).

The stress-strain curves of different plastic polymers show some common features (see Figure 3.3). The material exhibits a relatively stiff initial response, followed by yielding. It must be stressed, however, that in most polymers the development of permanent plastic strain is a continuous function of the applied strain, showing no discontinuity at the nominal stress drop or extrapolated yield point (Ward, 1971) (see Remark 3.1). After this transient behavior, it sometimes follows a steady state where the stress stabilizes, after which strain hardening begins, intensifying dramatically at large strains (Hiss et al., 1999; Callister and Rethwisch, 2014; Makradi et al., 2005).
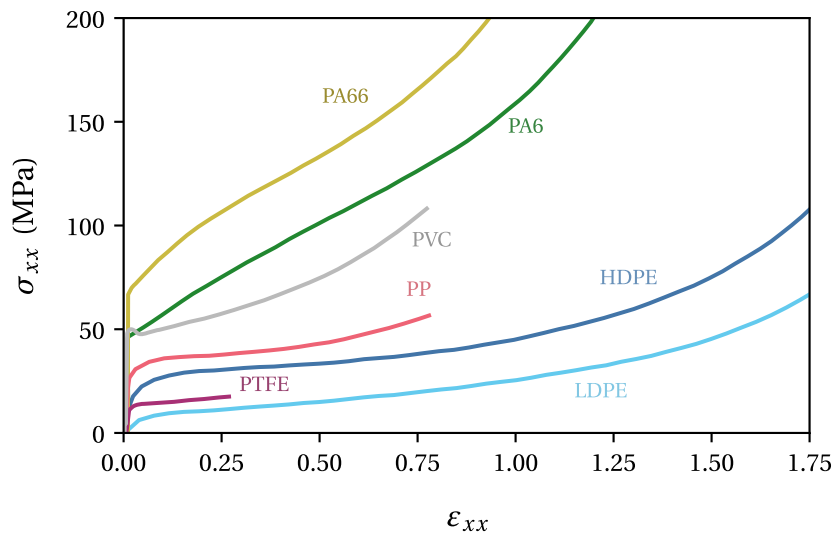
Figure 3.3: Stress-strain curves for different plastic polymers, including both glassy (PVC) and semi-crystalline (LDPE, HDPE, PTFE, PP, PA 6, PA 66) polymers in a constant strain rate uniaxial tension experiment. Adapted from G'Sell and Jonas (1981).

Remark 3.1 | Definition of yield in polymers

Yielding is commonly defined as the beginning of plastic flow. When modeling metals far from their melting temperature, it is commonly assumed that plastic flow only begins when a critical stress, the yield stress, is reached. Most polymers, on the other hand, may flow, i.e., "yield," at any stress level. The initiation of

plastic strain is mainly controlled by kinetic processes and appears to play no part in determining the yield stress of the material (Fotheringham and Cherry, 1978), commonly defined in one of three ways (Ward, 1971) (see Figure 3.4): Fix this

- the stress at the maximum observed load;

- the stress corresponding to the point of intersection of two tangent lines on the stress-strain curve;

- the stress obtained when offsetting the linear portion of the response by a pre-defined strain amount.
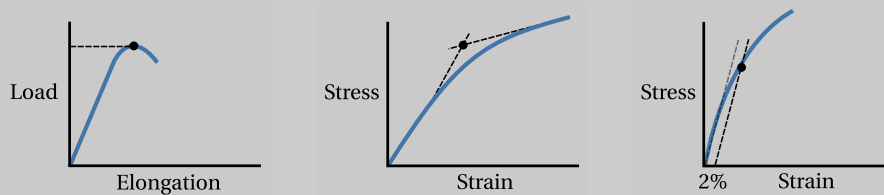
Figure 3.4: Yield criteria for polymers.

Pre-yield and yield behavior   Based on the description already given for the behavior of a plastic polymer, one should compare the stiffness and strength of polymers, particularly semi-crystalline polymers, relative to other materials. In general, the Young modulus of polymers ranges from 0.1 GPa to 10 GPa. The upper bound is the domain of resins, with thermoplastics, both glassy and semi-crystalline, rarely going over 2 GPa, which is relatively low compared with ceramics and metals, which boast Young moduli approximately 50 and 500 times larger, respectively. Their strength ranges from less than 10 MPa to approximately 100 MPa (see Table 3.1). In turn, some alloys reach tensile strengths above 1000 MPa, and some ceramics display compressive strengths as large as 10 000 MPa. That said, polymers possess densities around 1000 kg/m^3, making their specific stiffness and strength competitive with metals and well-suited for applications where weight reduction is paramount. Polymers are also distinguished by their relatively large failure strain, or the strain at which the materials cease to be linearly elastic, which ranges between 0.01 and 0.10, indicating an excellent capacity to store energy per unit weight (Ashby, 1999).

Table 3.1 displays the Young moduli and tensile strengths of semi-crystalline polymers ranging from commodity (HDPE and PP) to engineering grade (PA66 and PET), high performance (PPA), and ultra-high performance (PEEK) as supplied by a manufacturer (RTP Company, 2021). Glassy polymers of comparable stiffness and strength can be found, with PVC being suitable for commodity applications, ABS and PC being engineering grade, PSU being a high performance glassy polymer, and PAI being an ultra-performance glassy polymer.

Regarding the response of a semi-crystalline polymer pre-yield, an increase in temperature will lead to a more compliant response and a lower yield strength, as shown in Figure 3.5 for nylon 101 (Khan and Farrokh, 2006), and in the results reported in Brown et al. (2007) and Hobeika et al. (2000) for PEs. In fact, the temperature is possibly the single most influential parameter dictating a polymer's mechanical response. Some polymers may exhibit brittle fracture to necking or even

Table 3.1: Young moduli and tensile strength of semi-crystalline polymers (RTP Company, 2021).

	HDPE	PP	PA66	PET	PPA	PEEK
Young modulus (MPa)	1241	1724	1793	1379	4137	3792
Yield stress (MPa)	20	32	45	43	76	93

homogeneous rupture during a uniaxial tension test depending on the temperature (Ward and Sweeney, 2004). Moreover, whether the polymer is below or above its glass transition temperature results in markedly different behaviors in the case of amorphous polymers (see Figure 3.5 adapted from Van Loock and Fleck (2018)). An amorphous polymer in its glassy state behaves as a plastic polymer, whereas in its rubbery state has a much more compliant response that involves large deformations and a lack of a clear yield point. On the other hand, even if the temperature of a semi-crystalline polymer is much higher than its glass transition temperature, the crystalline phase causes the polymer's response to be qualitatively similar to that of a plastic polymer, although less stiff than it would be at a lower temperature (see Figure 3.5).
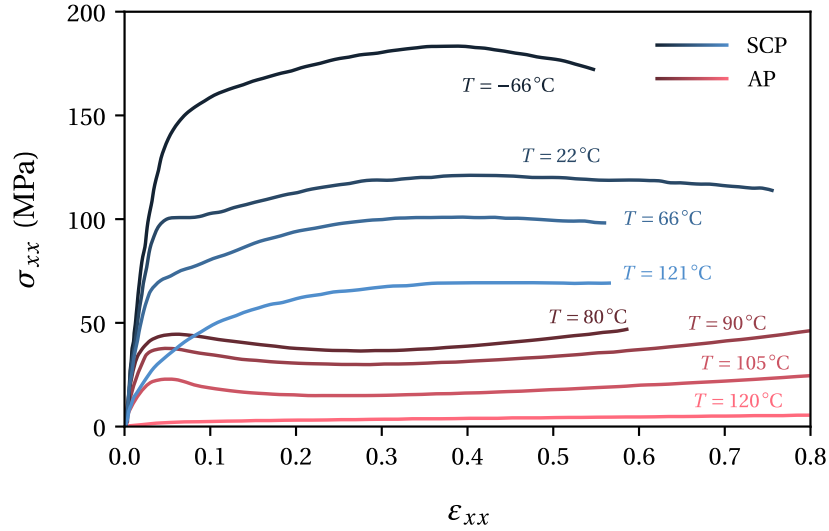
Figure 3.5: Stress-strain curves for a semi-crystalline polymer (SCP), nylon 101 (Khan and Farrokh, 2006), and an amorphous polymer (AP), poly(methyl methacrylate) (Van Loock and Fleck, 2018), Above and below their glass transition temperatures, 60 °C and 118 °C, respectively.

The strain rate and the hydrostatic pressure have the opposite effect, such that their increase will lead to a stiffer response and higher yield stresses, as gathered from the results in Popelar et al. (1990) (uniaxial tension) and Truss et al. (1981) (torsion). More specifically, regarding the effect of the strain rate on the stress response, Walley and Field (Walley and Field, 1994) present experimental results for uniaxial

compressive tests on a wide selection of polymers, including semi-crystalline polymers. The HDPE samples display a linear relationship between the stress at different strain levels and the logarithm of the strain rate, while the PTFE's response shows a non-monotic relationship between the same quantities, which is however broadly increasing. A linear relationship is found between the maximum stress and the logarithm of the strain rate for PEEK, until a critical strain rate is reached, followed by a decrease in the stress response. El-Qoubaa and Othman (El-Qoubaa and Othman, 2016) also provide an extensive set of results regarding the relationship between the strain rate, the temperature and the yield strength of PEEK. They find, however, that the yield stress of the polymer always increases with the strain rate, as shown in Figure 3.6.
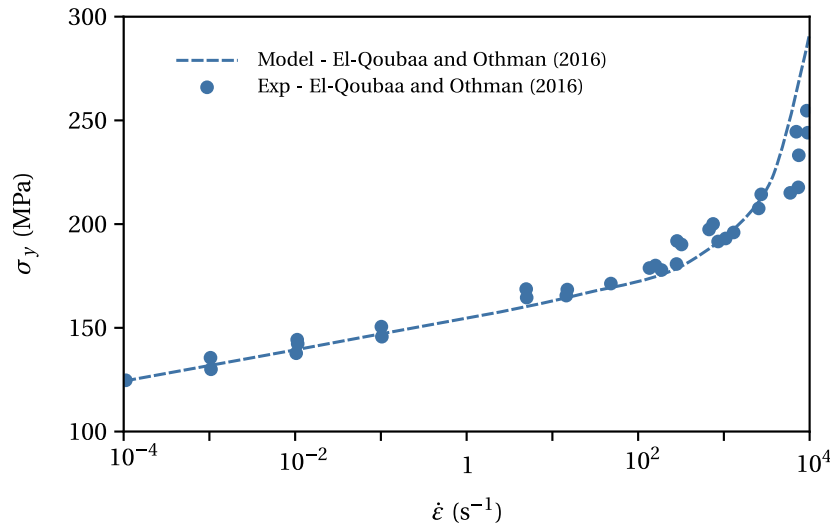
Figure 3.6: Yield stress, σ_y, as function of the strain rate, $\dot{\varepsilon}$, for PEEK at room temperature. Model and experimental results taken from El-Qoubaa and Othman (2016).

An increase in bulk crystallinity will lead to a stiffer response and increased strength as evident in the results of Ayoub and coworkers (Ayoub et al., 2011) and Bedoui and coworkers (Bedoui et al., 2006) for polyethylenes with degrees of crystallinity by weight at room temperature ranging from 15 to 72% (see Figure **??**). However, the relationship between stiffness and crystallinity appears to be nonlinear. That said, Schrauwen and coworkers (Schrauwen et al., 2004) tests in uniaxial compression samples of both PET and PE containing more similar degrees of crystallinity among the samples, 0%, 21.75%, and 29.7% and 68.4%, 72.3%, and 76.6%, respectively, and no stiffness differences are observed. However, the yield strength increases noticeably (see Figure 3.7(b)). The results of Kurtz and coworkers (Kurtz et al., 2002) on UHWPE also support a positive correlation between the degreee of crystallinity and both stiffness and yield strength. The same authors (Kurtz et al., 1999, 2002) also explore the effect of cross-linking due to radiation combined with changes in crystallinity due to thermal treatments. A decrease in the elastic modulus and the yield stress with the irradiation dose and the temperature of the thermal treatment is reported.
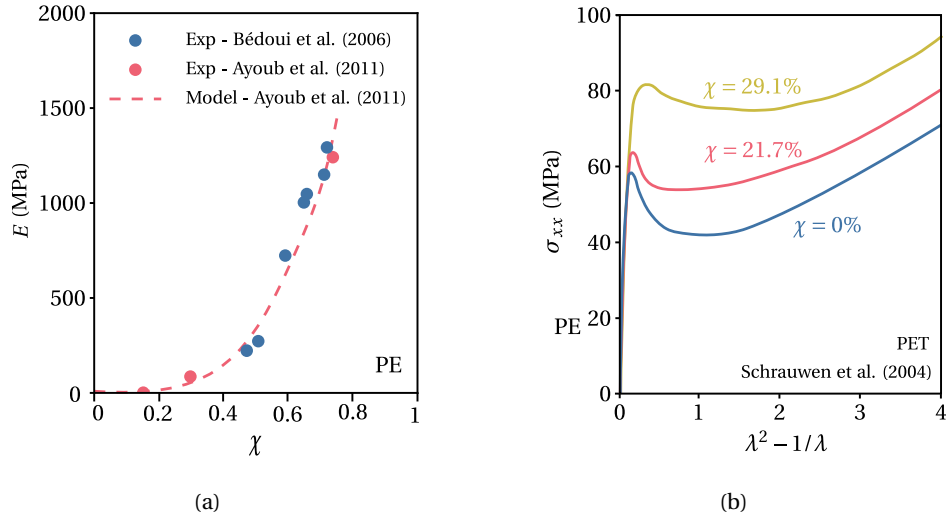
Figure 3.7: Effect of the bulk crystallinity on (a) the Young modulus, E, and on the (b) yield strength of a semi-crystalline polymer.

Schrauwen and coworkers (Schrauwen et al., 2004) further report that the yield stress is proportional to the lamellar thickness. However, based on results for PE, Argon (Argon, 2013) mentions that this linear dependence is only observed for lamellae of conventional thickness in the range of 10 nm to 15 nm. This dependence eventually breaks down, with the yield strength remaining constant for thicknesses from 20 nm to 170 nm. Also, for some polymers, an increase in molecular weight leads to an increase of tensile strength. This behavior is explained by an increase in chain entanglements with rising molecular weight (Callister and Rethwisch, 2014).

Regarding the effect of the mesostructure on the response of a semi-crystalline polymer, one can compare the behavior of isotropic (spherulitic) and oriented (fibrilar) PE when subject to uniaxial tension. As shown in Na et al. (2006), the latter possesses a higher yield strength and begins to strain harden immediately after yielding, while the former resists at an approximately constant stress.

Finally, the critical strains at which the Hookean range ends or yield is observed are independent of the temperature and strain rate in the ranges considered by Hobeika and coworkers (Hobeika et al., 2000), i.e., 23 °C to 100 °C and $10 \times 10^{-4}\,\mathrm{s}^{-1}$ to $10 \times 10^{-2}\,\mathrm{s}^{-1}$, in PE and PEVA. In addition, both bulk crystallinity and molecular weight appear to have no impact on the location of these transition points.

Post-yield   There may be some intrinsic strain softening after yielding, i.e., a decrease in stress with strain. The results in Schrauwen et al. (2004) show that after yield is reached, there is a sharp decrease in stress for completely amorphous PET above its glass transition temperature. The drop becomes broader and less pronounced as crystallinity increases to values of 21.7% and 29.1%. The same authors present PE results that show no strain softening for a degree of crystallinity of 76.6%. Minor strain softening is visible at lower crystallinity values for the same polymer. PP softens mildly as well, despite having a crystallinity of around 70% in the samples studied. These results were obtained under uniaxial compression, however, no softening is visible

after yield in the results of Truss and coworkers (Truss et al., 1981) obtained for PE in torsion. G'sell and coworkers (G'Sell et al., 1983) present results of pure shear experiments in which HDPE exhibit mild strain softening at 23 °C while PP and PA66 show none.

The presence of strain softening can, nevertheless, change with the strain. G'sell and Jonas (G'Sell and Jonas, 1981) present experimental results where the strain rate alternates between $10^{-3}\,\mathrm{s}^{-1}$ and $10^2\,\mathrm{s}^{-1}$. This makes possible the observation of stress transients at different strain levels, when the strain rate switches between the predetermined strain rates. An unusual behavior is detected in semi-crystalline polymers below the glass transition temperature, such that for lower strains a "normal" transient, i.e., one corresponding to no strain softening, is observed, while at higher strains an "inverse" transient, i.e., one coinciding with strain softening, is detected. The latter type of transient is observable in glassy polymers when the same experiment is performed at any strain level. The results of Nanzai (Nanzai, 1990) for poly(methyl methacrylate) (PMMA) support this claim regarding the transient behavior of glassy polymers. According to G'sell and Jonas (G'sell and Jonas, 1979), an "inverse" transient happens when there are different conditions necessary for the initiation and the propagation of yielding. Frost and Ashby (Frost and Ashby, 1982) mention that such transients are observed in "hard" materials, where dislocations are not readily available, such as lithium floride crystals (Gilman, 1959; Johnston, 1962) or diamond (Alexander and Haasen, 1969).

Despite the existence of intrinsic strain softening, its experimental observation is made difficult by two different phenomena: thermal softening and plastic instabilities. The results presented thus far were obtained at strain rates slow enough to allow for isothermal evolution. However, as the strain rate increases, a phenomenon known as "temperature softening" occurs, causing a similar decrease in stress with strain due to an increase in temperature. This rise in temperature is a result of the difficulty in offloading the heat generated by the plastic work in such a short period of time, making the process adiabatic. According to Furmanski and coworkers (Furmanski et al., 2013), this effect should be considered at strain rates greater than $0.01\,\mathrm{s}^{-1}$ and strains greater than 15%. Cundiff and coworkers (Cundiff et al., 2022), for example, report uniaxial compressive tests for PA 6 where temperature-induced strain softening may be observed.

Plastic instabilities, i.e., the growth of a locally thinned region in a material upon application of stresses, must also be considered when the intrinsic response of the material is sought. They are a function of the geometry and loading conditions of the loaded body, in addition to its intrinsic constitutive behavior (Ward and Sweeney, 2004). While uniaxial compressive loading of cylindrical specimens, generally, doesn't lead to heterogeneous deformation, this is not the case for uniaxial tension experiments, which often, but not always, lead to necking (see the comparison between isotropic and oriented PE in Na et al. (2006)), or simple shear experiments, which may lead to shear banding (G'Sell et al., 1983). There are, nonetheless, experimental methods which allow for the use of uniaxial tensile tests in the determination of intrisic material behavior. The video-controlled technique in (G'Sell et al., 1992) is one example, as is the SEÉ method (Lauro et al., 2010; Balieu et al., 2015), which uses full-field data from digital correlation measurements of heterogeneous displacement fields.

For a material whose stress response depends only on the strain, a maximum in the nominal stress implies the formation of a neck (Ward and Sweeney, 2004). There are also other equivalent criteria, such as Considère's criterion for necking. Polymers,

however, exhibit a strain rate dependence, and thus, because necking is associated with a local increase in strain rate such a strong dependence can inhibit necking even when the nominal stress reaches a maximum. For these materials, the existence of a maximum in the nominal stress is only a necessary condition (Ward and Sweeney, 2004). In fact, according to Brooks and coworkers (Brooks et al., 1995), a double yield phenomenon is observed in polyethylenes ranging from LDPE to HDPE. Lucas and coworkers (Lucas et al., 1995) report similar results for linear polyethylenes and well-characterized ethylene copolymers of narrow molecular weight and composition distributions. Hao and coworkers (Hao et al., 2022b) mention that this phenomenon has also been observed on polyamide (PA), polytrimethyleneterephthalate (PTT), and polybutyleneterephthalate (PBT). The maximum force observed at the first yield point under certain conditions is therefore associated with a homogeneous strain-softening process within the materials and not with the development of the neck (i.e., a geometrical instability), which occurs at the second yield point (see Figure 3.8). These experimental results make clear that such complex yielding processes are not always observed.
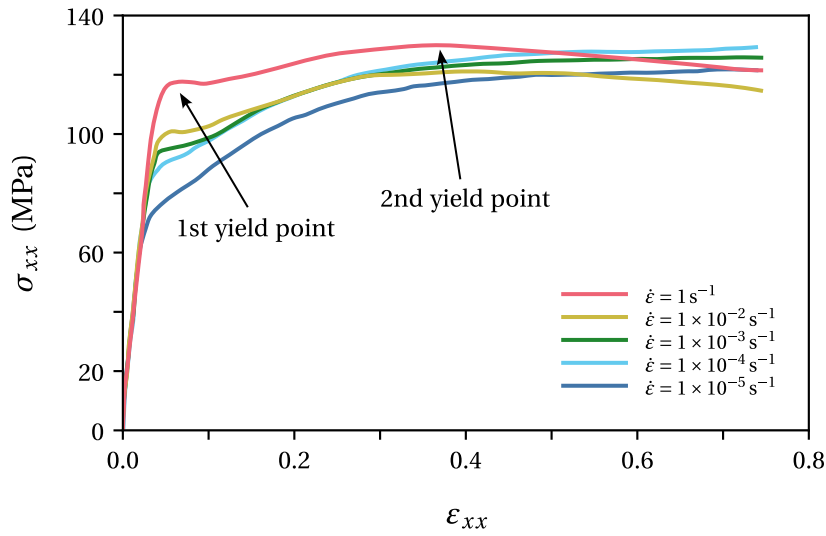
Figure 3.8: Stress-strain curve for nylon 101 exhibiting double yield. Adapted from Khan and Farrokh (2006).

Ye et al. (2015) reports that for HDPE, even with measurements made on a relatively small strain rate range (smaller than 1 decade), the necking phenomenon depends on the strain rate. In particular, they found that the strain localization is more pronounced with higher strain rates near the yield point.

After necking occurs—usually at the maximum load, but not always, as in the case of double yield—the material resists by reorienting the polymer chains so that the deformation is not limited to the necking zone, as in ductile materials (Callister and Rethwisch, 2014). As the specimen thins from the initial cross-section to the drawn cross-section, the shoulders of the neck–this phenomenon is called cold drawing (see Figure 3.9). The existence of a finite or natural draw ratio, i.e., a strain deformation corresponding to the stable propagation of the neck, is an important aspect of polymer deformation because a stabilized neck is not always formed (Ward and Sweeney, 2004).

The neck's stable propagation occurs when the neck area has hardened sufficiently, allowing other sections of the specimen to meet the necking criteria. If this is the case, Considéré's criterion for necking can be used to determine it.

Necking with cold drawing   Necking without cold drawing
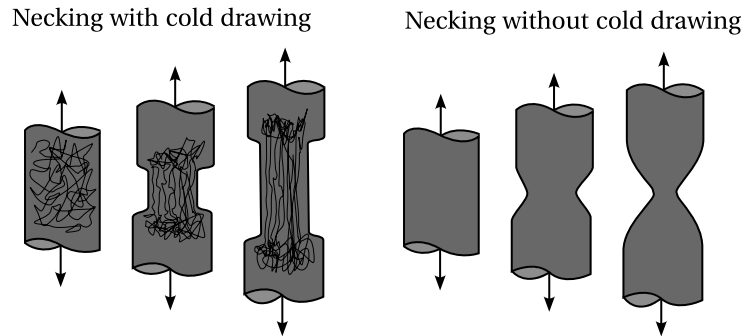
Figure 3.9: Schematic depiction of two tension experiments. One where there is formation of a neck and stabilization, corresponding to cold drawing, and the other with neck formation but no neck stabilization, such that cold drawing is not observed.

Another important aspect regarding the plasticity of semi-crystalline polymers is that, in contrast to metals, permanent volumetric strains can be detected in addition to elasticity-related volumetric strains. These effects, found both in tension and compression, cannot be explained by Hooke's elasticity and correspond to an irreversible contraction or dilation of the material (Cangemi and Meimon, 2001; Polanco-Loria et al., 2010).

Cangemi and Meimon (Cangemi and Meimon, 2001) report the existence of plastic dilation in compression for semi-crystalline polymers. In contrast, glassy polymers show a very weak contraction. According to the same authors' results for PA11, the effect of plasticity on volumetric strain is felt when a strain of 0.03 is reached. Until then, the material contracts, after which a significant volume increase is observed. An increase in confining pressure was also investigated, and the authors discovered that it resulted in a qualitatively similar evolution of the volumetric strain, though it was more pronounced in magnitude, before attaining approximately the same value after a strain of 0.16 is reached. Tensile tests were also performed by the authors, during which the volume strain increases globally, due to the elastic response of the material. As the material approaches the plastic domain, the total volume strain is slighly reduced and then increases again at the end of the test. Qualitatively identical results were obtained by other authors for PA11 (Marchal, 1996).

Damage, or void growth, is one of the mechanisms responsible for these observations. However, according to Polanco-Loria and coworkers (Polanco-Loria et al., 2010), an increase in volume in semi-crystalline polymers may also be associated with crystalline deformation. This happens because the molecules are organized in a rather dense manner in the crystalline phase, and thus the specific volume is likely to increase when the crystalline lamellae break up. In fact, after a compression test in which the specimens showed net plastic expansion for the majority of the test, Kitagawa and Yoneyama (Kitagawa and Yoneyama, 1988) made thin cuttings of semi-crystalline polymer samples (PP, POM, and PE) for observations in a polarized light microscope. No cracks or crazes were found. This point expresses

the peculiarity of plastic volume expansion in semi-crystalline polymers, which may be related to the complexity of their microstructures as well as their two-phase nature (Cangemi and Meimon, 2001).

Steady state flow   After the transient described above is cleared and before strain hardening starts to become noticeable, there is a period of steady state flow, in which the polymer flows at a constant stress function of the temperature and the strain rate. Both Kurtz and coworkers (Kurtz et al., 2002), for UHWPE, and G'sell and Jonas (G'sell and Jonas, 1979), for HDPE, found a reduced strain rate dependence coinciding with a small coefficient fiting a power law relationship between the stress and the strain rate comparable to metals. The first authors point out, however, based on their results for UHWPE, that the strain rate sensitivity increases significantly with temperature.

Strain hardening   Semi-crystalline polymers, if ductile enough, will exhibit strain hardening, which can be quite dramatic at higher strains. Orientation hardening at large deformation due to molecular alignment is the main source of strain hardening (Ahzi et al., 2003). In addition to molecular alignment, crystal orientation may also contribute to the strain hardening observed in semi-crystalline polymers (Abdul-Hameed et al., 2014).

The results presented by G'Sell and Jonas (G'Sell and Jonas, 1981) at constant strain rate show that semi-crystalline polymers such as HDPE, LDPE, PA6 and PA66 show marked strain hardening at $22\,^{\circ}\mathrm{C}$ and a strain rate of $10^{-3}\,\mathrm{s}^{-1}$. Based on the previously mentioned compressive tests, Schrauwen and coworkers (Schrauwen et al., 2004) conclude that crystallinity and lamellar thickness have no effect on the strain hardening of semi-crystalline polymers, in constrast with the melt cooling procedure and subsequent heat treatments. This suggests that the mesostructure may have an effect on the polymer's strain hardening behavior. See this

Failure   The maximum strain at rupture for semi-crystalline polymers can be very large, as evidenced by the results of G'Sell and coworkers (G'Sell and Jonas, 1981; G'Sell et al., 1983). HDPE can reach strains of more than 2 in tensile tests and more than 10 in shear tests. This is significantly greater than what glassy polymers like PVC and PC can achieve.

Experimental results   Table 3.2 compiles a sample of the available experimental results in the literature concerning constant strain rate experiments on semi-crystaline polymers.

Table 3.2: Experimental results concerning constant strain rate experiments.

Author	Strain rate (s^{-1})	Temperature (°C)	Pressure (MPa)	Max strain	Loading mode	Material
G'Sell and Jonas (1981)	2×10^{-4} to 10^{-1}	22	Ambient	1.5 - 2	Uniaxial tension	HDPE
G'Sell and Jonas (1981)	10^{-3}	22	Ambient	1.7	Uniaxial tension	LDPE, HDPE, PA6, PA66, PTFE
Truss et al. (1981)	9×10^{-4}	20	10^{-1} to 4×10^2	0.16	Torsion	Rigidex xxx
Popelar et al. (1990)	10^{-5} to 10^{-1}	23, 77	Ambient	0.25	Uniaxial tension	MDPE, HDPE
G'sell and Dahoun (1994)	5×10^{-4}	25	Ambient	2	Uniaxial tension	HDPE
Hiss et al. (1999)	10^{-4} to 10^{-2}	Room	Ambient	2	Uniaxial	HDPE
Hiss et al. (1999)	5×10^{-3}	Room	Ambient	1.75 to 2	Uniaxial tension	HDPE, LDPE, PEVA
Hobeika et al. (2000)	10^{-4} to 10^{-2}	23 to 110	Ambient	1.8	Uniaxial tension	HDPE, LDPE, PEVA
Beijer and Spoormaker (2000)	3×10^{-7} to 10^{-1}	43	Ambient	0.25	Uniaxial	HDPE
Schrauwen et al. (2004)	3×10^{-3}	Room	Ambient	0.9	Uniaxial compression	PE
Na et al. (2006)	10^{-3} to 10^{-2}	Room	Ambient	1	Uniaxial	Oriented HDPE
Drozdov (2007)	5×10^{-4} to 3×10^{-2}	Room	Ambient	0.2	Uniaxial tension	LDPE
Drozdov (2007)	5×10^{-4} to 10^{-1}	Room	Ambient	0.2	Uniaxial compression	LDPE
Brown et al. (2007)	10^{-4} to 3×10^3	−75 to 100	Ambient	0.5	Uniaxial compression	HDPE, PEX, UHWPE
Ayoub et al. (2010)	5×10^{-4} to 10^{-2}	Ambient	Ambient	2.5	Uniaxial	HDPE
Zeng et al. (2010)	3×10^{-2} to 10^{-1}	90	Ambient	1.5	Uniaxial tension	PE, PA6
Ayoub et al. (2011)	10^{-4} to 10^{-2}	Ambient	Ambient	1.8	Uniaxial tension	PE copolymers
Furmanski et al. (2013)	10^{-3} to 1	−80 to 20	Ambient	0.6	Uniaxial compression	HDPE, UHMWPE
Bergström (2015)	2×10^{-3} to 10^{-2}	-	Ambient	0.5	Uniaxial tension	PTFE
Bergström (2015)	2×10^{-4} to 2×10^{-2}	-	Ambient	0.35	Uniaxial	HDPE
Arieby et al. (2017)	10^{-3}	Ambient	Ambient	1.6	Uniaxial tension	HDPE

3.2.2 Stress relaxation, creep and dynamic mechanical analysis experiments

The stress relaxation, creep, and dynamic mechanical analysis experiments are all pertinent experiments to characterize the time-dependent behavior of a material. In particular, the semi-crystalline polymers exhibit a time-dependent behavior that sets them apart, for example, from metals at temperatures far below their melting point. This section will first focus on isothermal measurements, then on isochronal measurements.

The stress relaxation experiment involves applying a constant strain to the material, yielding its so-called relaxation modulus as the corresponding stress response. Polymeric systems, as a rule, display a decreasing relaxation modulus with time. A sharp drop is however not noticeable in highly semi-crystalline and glassy polymers, which exhibit stress relaxation moduli in the order of Pa, as depicted in Figure 3.10(a). Semi-crystalline polymers with a lower crystalline content exhibit a primary viscoelastic transition from a glasslike to a leathery consistency as a decrease in the stiffness from the order of 10×10^9 Pa to 10×10^7 Pa, as shown in Figure 3.10(a). s with a degree of crystallinity between 5% to 10% are termed by Tobolsky (Tobolsky, 1960) as very slightly crystalline polymers. This is similar to the behavior of cross-linked amorphous polymers, since individual molecules may thread in and out of crystalline regions that act as multiple cross-links (Ferry, 1980; G'Sell and Jonas, 1981). See, for example, the results of Faucher (Faucher, 1959) comparing the relaxation behavior of amorphous and crystalline polypropylene.

This change in the material's response with time is commonly referred to as a transition from a glasslike to a rubberlike (or leatherlike, if a stiffer response is observed) behavior. However, it is a viscoelastic transition, not the transition verified at the glass transition temperature, in which the thermodynamic state of the material changes. The thermodynamical state of the material remains unchanged in this case, with this particular behavior traceable to the manner in which the kinetic units flow. Their flow can be described as a thermally activated process where the energetic barriers preventing their motion are cleared with the help of random thermal fluctuations. The kinetic units have to "wait" until a large enough thermal variation puts them over the hump and they begin moving. Thus, for very short times, the response of the material will be stiffer, as the kinetic units do not have enough time to flow. As time goes on, more and more kinetic units will be able to move, leading to a softer response. Hence, in time dependent materials, the ratio of the time it takes for a material to adjust to applied stresses or deformations, the relaxation time, t_c, and the characteristic time scale of an experiment (or a computer simulation), t_p, probing the response of the material is especially important. The Deborah number is the dimensionless quantity defined as this ratio, such that flow will happen when (Ward and Sweeney, 2004; Arzhakov, 2019)

$$\text{De} = \frac{t_c}{t_p} \approx 1. \tag{3.1}$$

A constant stress is imposed in a creep experiment, for example, by dead-loading (Wilding and Ward, 1981), and an increase in strain is expected over time. This strain response is the so-called creep compliance of the material. Glassy polymers and highly crystalline polymers exhibit similar behaviors, with very slow increases in creep compliance with time at the longest times of observation, as do low crystallinity

polymers and crosslinked polymers, which exhibit a viscoelastic transition via an increase in compliance as time progresses (Ferry, 1980) (see Figure 3.10(b)).
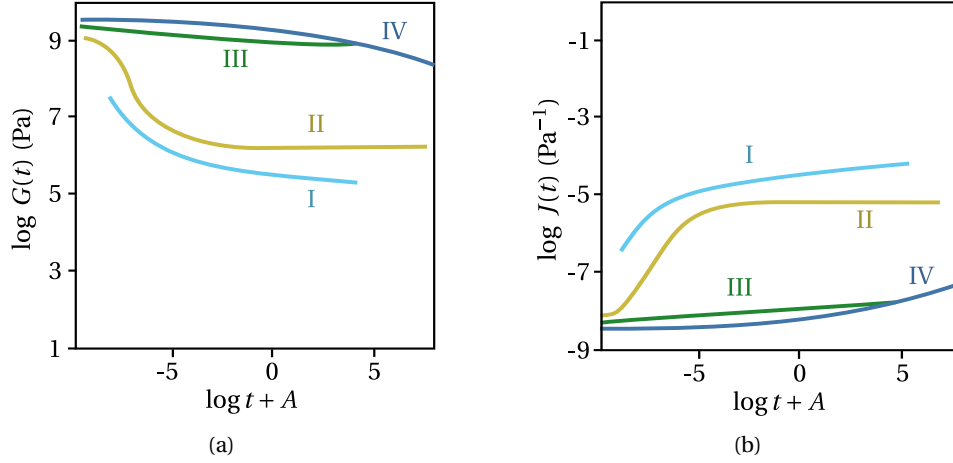
Figure 3.10: Typical viscoelastic properties of a very lightly crosslinked polymer (I), a slightly crystalline or lightly crosslinked polymer (II), a glassy polymer (III) and a highly crystalline polymer: (a) relaxation modulus, G. (b) creep compliance, J. A is an appropriate horizontal shift constant. Adapted from Ferry (1980).

A dynamic mechanical analysis (DMA) employs either a strain- or stress-driven steady-state harmonic oscillation and records the corresponding stress or strain response, respectively. For a strain-driven experiment, the quantities of interest are the storage and loss moduli, defined as the stress response in phase and out phase relative to the strain divided by the strain amplitude, and the loss tangent, which is the tangent of the phase shift between the strain and the stress. Loss and storage compliances can be defined in a similar way when considering a stress-driven experiment. Their physical interpretation is suggested by their respective names, as they are measures of the energy stored and lost per cycle. For a perfectly elastic material, one would expect no loss and, thus, for the stress and the strain to be in phase. On the other hand, a completely viscous material would exhibit a 90-degree phase shift, dissipating all the energy supplied to the system as heat. Depending on the frequency, a real material will exhibit an intermediate behavior. When $\omega\, t_c \approx 1$, i.e., De ≈ 1, for some deformation mechanism with a relaxation time of t_c, there will be an increase in the viscous character of the material, hence leading to a drop in the storage modulus, and maxima in loss modulus and loss tangent (often, not exactly at the same frequency) (Ferry, 1980).

The storage modulus and compliance are approximately mirror images of the stress relaxation modulus and creep compliance, since a dynamic measurement at frequency ω is qualitatively equivalent to a transient one at $t = 1/\omega$. The glassy and crystalline polymers have values arround 0.1 for the tangent loss and may present several maxima associated with various deformation mechanisms (Ferry, 1980). Most metallic alloys employed in engineering applications possess tangent losses one to two orders of magnitude smaller (Ashby, 1999). See Figure 3.11 for the loss and storage modulus of highly and lightly crystalline polymers.

Ferry (Ferry, 1980) collects some experimental results illustrating the nonlinear
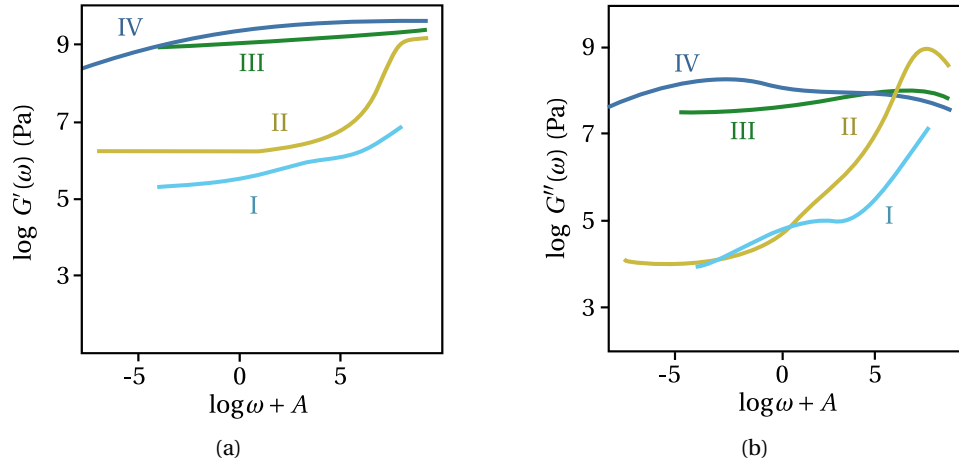
Figure 3.11: Typical viscoelastic properties of a very lightly crosslinked polymer (I), a slightly crystalline or lightly crosslinked polymer (II), a glassy polymer (III), and a highly crystalline polymer: (a) storage modulus, G'. (b) loss modulus, G''. A is an appropriate horizontal shift constant. Adapted from Ferry (1980).

behavior of semi-crystalline polymers. See Section 4.1 for a more thorough discussion on what is the expected linear behavior for a time-dependent material. In a stress relaxation experiment, linear behavior implies coinciding curves when the relaxation modulus divided by the strain is plotted for different strain levels. However, for tensile stress relaxation of PE single crystal mats, the ratio of stress to strain decreases more rapidly with time at higher extensions, in the range of $\epsilon = 0.0003$ to 0.003; the degree of nonlinearity increases markedly with decreasing temperature in the range of $40\,°\mathrm{C}$ to $10\,°\mathrm{C}$. Nonlinear creep recovery of polyethylene has also been reported. It is demonstrated that after a partial stress relaxation at constant strain for various times and strain magnitudes, recovery is much slower at large strains but somewhat faster for shorter durations of the initial strain. In this system, strains less than 0.01% appear to be required for a linear behavior. Nonlinear behavior when subject to sinusoidal deformations with large amplitudes has also been investigated. Finally, Ben Hadj Hamouda and coworkers (Ben Hadj Hamouda et al., 2007) report the existence of two regimes of creep deformation for medium density ethylene-butene copolymers (MDPE).

Remark 3.2 | Types of non-linear behavior

According to Malkin (Malkin, 1995) there are three types of non-linearity in the constitutive response of a material.

1. *geometrical, stationary, or weak non-linearity:* characterized by permanent material constants and unchanging relaxation properties. The neo-Hookean behavior of rubbers is one such example;

2. *physical, kinetic, or strong non-linearity:* explained by changes in the inherent structure of a material due to deformation and characterized by

changing material constants and relaxation properties with deformation. The hysteresis in repeated deformations of rubbers (the Mullins effect) and crystalline polymers;

3. *phase, thermodynamic or rupture non-linearity:* explained by phase or relaxation transitions induced by deformation and characterized by change in the physical state of the material and radical changes in its relaxation spectrum. The transition of linear polymers from a rubbery to a glassy state is one example.

The results previously discussed were obtained at a constant temperature and are thus isothermal. By running tests at different temperatures it is often possible to extend the time/frequency range of the experimental results by employing the method of reduced variables, also known as the time-temperature superposition principle or the thermorheological simple postulate (Ferry, 1980; Christensen, 2013). It consists of an appropriate horizontal and vertical shift of experimental results obtained at different temperatures to construct a single isothermal master curve. A physical justification for the applicability of this procedure regarding the horizontal shift can be given in terms of the thermally activated processes that underlie the deformation mechanisms responsible for the relaxation transitions (Arzhakov, 2019). There are several models for the horizontal shift, perhaps the most well-known being the site model theory and the Williams, Landel, and Ferry (WLF) equation (Ward and Sweeney, 2004; Furmanski et al., 2013). A more detailed discussion of the models available is given in Section 4.4.1. A suitable vertical shift can be achieved through the multiplication by $T_0 \rho_0 / T \rho$, where the subscript 0 denotes a reference state and T and ρ are the temperature and density, respectively. Its use is justified due to the entropy-spring nature of the stored elastic energy in the flexible chain theory (Ferry, 1980). An application of the time-temperature superposition principle can be found in Popelar et al. (1990), where a master curve is built for a polyethylene employing both horizontal and vertical shifts.

Isochronal results are obtained when the mechanical experiments described in this section are performed at different temperatures and plotted at the same time or frequency. These are, in fact, the most common type of available data on semi-crystalline polymers (Ferry, 1980). It should be noted that the system's structure changes with temperature, and thus an isothermal plot is, in some respects, more closely and simply related to the distribution of relaxation times than an isochronal plot (Hoffman et al., 2007). For example, there are relaxation behaviors that cannot be measured in low crystallinity samples of PCTFE, as it begins to crystallize before the corresponding temperature is reached (Hoffman et al., 2007).

Focus is given here to results obtained through DMA, although most observations apply to stress relaxation results as well as creep results. The most important information gathered from these experiments is the temperature of the relaxation transitions at a given frequency. Starting with low-crystallinity polymers helps clarify the discussion of relaxation transitions in semi-crystalline polymers. In fact, for a completely amorphous polymer glass, there will be two important transitions: the alpha and beta transitions. The alpha transition is tightly connected to the glass transition[1], and it is the main viscoelastic transition, while the beta transition is

---

[1]The glass transition is a thermodynamic transition that also implies a structure change in terms of a decrease in the free volume in addition to the cooperative motion of the polymer molecules associated with the alpha viscoelastic transition (Arzhakov, 2019).

another transition happening generally at a lower temperature (Arzhakov, 2019). Which of these happens at higher temperatures may change at high enough frequencies (Matsuoka, 1996). According to Arzhakov (Arzhakov, 2019), the elementary kinetic unit responsible for these transitions is a macromolecule segment, with the beta transition being linked to the quasi-independent, localized displacement of the segments (intramolecule), and the alpha transition, to these quasi-independent modes acquiring a cooperative, correlated character (intermolecule) (Bershtein and Yegorov, 1985; Matsuoka, 1996).   As the extent of crystallinity decreases and amorphous domains (large enough to allow configurational rearrangements of longer chain segments) appear in semi-crystalline polymers, the motions responsible for these two transitions gradually resemble those seen in the amorphous state in the transition zone of viscoelastic behavior (Ferry, 1980).

The previously used notation for alpha and beta transitions applies only to amorphous polymers.   In general, semi-crystalline polymer transitions are also classified using the Greek alphabet, but without taking into account the character of the molecular motions corresponding to the transition or the phase in the polymer where it occurs.   The transitions are named alphabetically, beginning with alpha in descending order of temperature, resulting in a sometimes confusing literature in which naming is not standardized.   Here, the naming convention will follow the suggestion in Arzhakov (2019), using increasing Roman numerals for relaxations verified at increasing temperatures.

Starting at the lowest temperatures, increasing the crystal content of the polymer has little effect on the temperature at which Relaxation I is verified, resulting in similar loss moduli and loss tangent profiles. See the results:

- for PET (β relaxation) by Takayanagi presented in Ward and Sweeney (2004) with degrees of crystallinity of 5, 34 and 50%, corresponding to $-60\,°C$ at $138\,Hz$ (see Figure 3.12(a));

- for PCTFE (γ relaxation) in McCrum (1962) with degrees of crystallinity of 27, 42 and 80%, corresponding to $-40\,°C$ at $1\,Hz$;

- for PE in Khanna et al. (1985) with degrees of crystallinity of ~45% (linear LDPE), ~48% (conventional LDPE) and ~67% (HDPE), corresponding to $-110\,°C$ at $1\,Hz$ (see Figure 3.12(b));

- for PP in McCrum (1959) with different unspecified degrees of crystallinity, corresponding to $-30\,°C$ at $1\,Hz$.

However, the temperature at which the next transition, Relaxation II, is verified varies with crystallinity. See the shift to higher temperature in the loss modulus, G'', of PET samples with increasing crystallinity in Figure 3.12(a). For the PE samples studied in Khanna et al. (1985), the temperature at which relaxation II is observed varies between $-27\,°C$ and $-10\,°C$.   With increasing crystallinity, this relaxation becomes broader and less pronounced, eventually dissapearing (see Figure 3.12). Relaxation I and II happen in the bulk amorphous phase of the semi-crystalline polymers, and the corresponding motions of the kinetic units are the ones responsible for the β and α transitions in the completely amorphous polymers.   The disappearance of the relaxations II with the increase in crystallinity is tied to the shrinking of the amorphous domains, and decrease in the number of longer kinetic units responsible for the relaxation. On the other hand, the relaxations I are connected to the motions

of smaller kinetic units, like the β transition in the amorphous polymers, and hence are not affected in the same way by the increase in crystallinity.

The appearance and increase in size of the crystalline phase will lead to the appearance of a third transition, Relaxation III, at higher temperatures. This transition is connected to motions on the surface of the crystal lamellae, and the temperature at which it is verified varies with their thickness (Khanna et al., 1985; Hoffman et al., 2007). Hoffman and coworkers (Hoffman et al., 2007) present a detailed model of the motions connected to each of the transitions in PCTFE and PE. Ward and Sweeney (Ward and Sweeney, 2004) also provide an explanation based on the deformation mechanism available with increasing crystallinity for the "disappearance" of Relaxation II in PE.

According to Arzhakov (Arzhakov, 2019), by employing etching techniques that remove the amorphous phase, it can be gathered that the relaxation transitions described so far originate in kinetic units found in the amorphous phase of the polymer. There is, however, sometimes a fourth relaxation, connected to the kinetic units in the crystalline phase, which may imply the melting of some of the crystallites. This transition appears to be visible in the results of Panowicz and coworkers (Panowicz et al., 2021) for PET. It seems, however, not to be noticeable in the other experimental results mentioned so far. Hoffman and coworkers (Hoffman et al., 2007) also mention the existence of a cryogenic transition, present in some polymers, such as isotactic propylene (iPP).
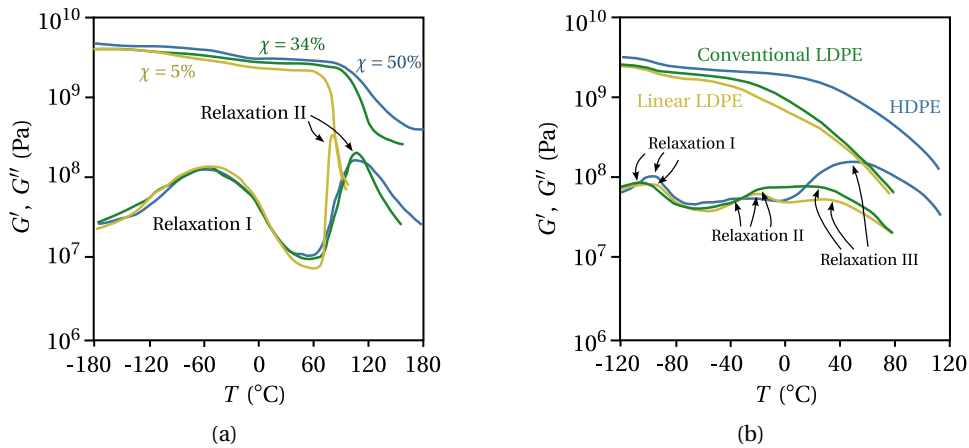
Figure 3.12: Dynamic mechanical analysis results for (a) PET with degrees of crystallinity of 5%, 34% and 50% at 138 Hz, obtained by Takayanagi (Ward and Sweeney, 2004), and for (b) PE samples, linear LDPE (~45%), conventional LDPE (~48%), and HDPE (~67%), at 1 Hz, obtained by Khanna et al. (1985).

As an example of a semi-crystalline polymer that doesn't fit exactly into the classification scheme just provided, see the results of McCrum (McCrum, 1959) for PTFE with crystallinities ranging from 48% to 92%. The relaxation observed at the lower temperatures ($\approx -100\,°C$) disappears with the increase in crystallinity. In addition, there is a crystalline first-order transition ($\approx 25\,°C$), corresponding to the change in crystalline structure of the polymer, and a third relaxation at higher temperatures ($125\,°C$) that merges with the second when the crystallinity increases. According to Calleja and coworkers (Calleja et al., 2013), the two relaxations observed

at the lowest and highest temperatures correspond to the relaxation of kinetic units in the amorphous phase of the polymer. The first is the "mobile amorphous fraction," which can relax at low temperatures, and the second is the "rigid amorphous fraction," which is composed of macromolecular segments found at the boundaries between crystalline and amorphous domains. Because of the close proximity of the crystallites, these macromolecular segments have more restricted mobility, and mechanical relaxation occurs at higher temperatures.

3.2.3   Reversible and irreversible deformation

The decomposition of the deformation of semi-crystalline polymers into elastic and plastic portions remains to be discussed. When applied to metals at temperatures far from their melting points, an elastic deformation pertains to the seemingly instantaneous part of the deformation that is recovered upon unloading. If the metal yields, there will be some plastic deformation that remains after unloading, which is irreversible. This decomposition is not as clear in the case of time-dependent materials, such as polymers, because there may be deformation that is not immediately recovered upon unloading but is recovered as time passes. It results in a definition of the irreversible part of the deformation, which is dependent on the observation time, i.e., some deformation may be irreversible during the experiment but potentially reversible if the observation was extended in time.

To clarify which part of the deformation is reversible and which is irreversible, the most useful mechanical experiments are the free shrinkage and step cycle tests. The former consists in straining the sample employing a constant strain rate, and releasing the load as some predefined strain is reached. The latter also begins as a constant strain rate experiment, but after a prescribed time interval has passed, the strain rate is reversed until the stress response reaches zero. Once it does, the strain rate is reversed again and enforced for the same time interval as before. The cycle is repeated until failure or a maximum strain is reached. During the unloading phases of an applied cyclic deformation process, the response is characterized by a nonlinear recovery driven by the release of stored internal energy (Bergström, 2002).

Strobl and coworkers (Hiss et al., 1999; Hobeika et al., 2000; Hong et al., 2004a,b; Na et al., 2006) performed a very detailed study on polyethylenes which includes the results of both free shrinkage and step cycle experiments. The decomposition of the constant strain rate stress-strain curve is based on the reversible and irreversible parts of the deformation as gathered from these experiments.

Consider the results of step-cycle experiments first. For strains less than 0.025, the polymer is perfectly elastic, and all deformation is immediately recovered. As the strain exceeds this limit, some deformation will not be recovered immediately. Reaching 0.1, the proportion of reversible strain increases relative to the irreversible strain. The former, on the other hand, plateaus once the strain exceeds 0.6 and begins to decrease once the strain reaches 1.

So far, only near-immediate recovery has been considered using data from step-cycle tests. To gain a better understanding of the reversible or irreversible deformation decomposition in semi-crystalline polymers, consider the results of free shrinkage experiments. In the results described in Hiss et al. (1999), where the deformation was observed for 10 minutes, the amount recovered for the same prestrain is greater than in a step-cycle experiment, as expected. Similarly, reversible deformation appears to peak around a strain of 0.6, with low-density polyethylene (LDPE) exhibiting a plateau until a strain of 1 is reached. A distinct plateau is not as

visible in high density polyethylene (HDPE) and poly(ethylene-co-vinyl acetate) (PEVA). However, above a strain of 0.6, all experiments show an increase in the amount of irreversible strain. Bartczak and coworkers (Bartczak et al., 1992) also report that HDPE samples deformed under uniaxial compression show large amounts of strain recovery upon releasing the load. They are partly instantaneous and partly over a period of a few hours (<24 h).

Finally, Hiss and coworkers (Hiss et al., 1999) report that increasing the temperature in a free shrinkage experiment allows for the recovery of more deformation. In fact, if the strain does not reach 1 and the temperature used is close to the melting point, almost all of the deformation is recovered. If the deformation exceeds one, some permanent deformation will remain even after this treatment. Similarly, Arridge and coworkers (Arridge et al., 1977) report that ultra-oriented polyethylene fibers obtained by drawing to approximately 30 times their original length contract on heating to a length near the original. Furthermore, the same authors investigated the forces that cause this contractile behavior by monitoring the stress in the fiber while keeping its length constant. Between room temperature and 110 °C the stress decreases as the temperature rises, and this behavior is reversible. At 120 °C, there is an irreversible increase in stress, followed by a reversible linear dependence of stress on absolute temperature, indicating elastic entropic forces. Finally, there are two or three small irreversible stress jumps between 124 °C and 130 °C, as well as a large irreversible stress increase at around 132 °C, which corresponds to the region of large-scale retraction. As the fiber relaxes and eventually melts, there is a decay in the stress response. A fiber allowed to relax in this manner below the melting point differs from a drawn fiber in that it does not exhibit contractile behavior on subsequent heating over a similar temperature range. Furthermore, despite having a lower tensile modulus after cooling, the modulus and density will rise to values close to their initial counterparts during storage.

3.3 Thermal analysis techniques

To fully characterize the thermomechanical behavior of semi-crystalline polymers, information about their thermal behavior must be gathered. This can be obtained from experiments such a dilatometry, differential scanning and laser flash tests (Blumm et al., 2010). The dilatometry experiment consists in tracking the change in volume in a range of temperatures, furnishing the linear thermal expansion of the material. In principle, the glass transition can be observed in these experiments as a change in the slope of the thermal expansion versus temperature curve. This is not, however, the case for the results of Blumm and coworkers (Blumm et al., 2010) concerning PTFE. What is readily apparent in the results of the same author is the transition in the crystal structure of the polymer, visible as a step in the curve. The evolution of the linear thermal expansion in the remainder of the temperature range is approximately linear, ranging from $500 \times 10^{-6}\,\text{K}^{-1}$ at $-100\,°\text{C}$ to $2000 \times 10^{-6}\,\text{K}^{-1}$ at $100\,°\text{C}$.

The thermal expansion coefficient can also be found through pressure volume temperature (PVT) experiments, as shown in Olasz and Gudmundson (2005) for cross-linked polyethylene (XLPE). The sample is immersed in mercury and enclosed in a piezometer cell for the experiment. The cell is contained within a pressure vessel in which hydrostatic pressure can be applied. After reaching equilibrium at any constant temperature and pressure, the change in specific volume relative to a reference state is

recorded. Measurements were performed from $10\,\mathrm{MPa}$ to $200\,\mathrm{MPa}$, at $10\,\mathrm{MPa}$ increments, and at temperatures ranging from $25\,°\mathrm{C}$ to $250\,°\mathrm{C}$, at approximately $10\,°\mathrm{C}$ increments. This allows the determination of the linear expansion coefficient and the bulk modulus as a function of the temperature. The values found range from around $300 \times 10^{-6}\,\mathrm{K}^{-1}$ at $50\,°\mathrm{C}$ to $1300 \times 10^{-6}\,\mathrm{K}^{-1}$ at $130\,°\mathrm{C}$. These values, as those reported above for PTFE, are an order of magnitude larger than those reported elsewhere for thermoplastics, in general, from $50 \times 10^{-6}\,\mathrm{K}^{-1}$ to $250 \times 10^{-6}\,\mathrm{K}^{-1}$ (Ashby, 1999). Leaving aside these differences, it is at least an order of magnitude larger than metals and ceramics. That said, in general, it does not often lead to thermal stresses, $\Delta\sigma$, as large as in metals, since for polymers $\Delta\sigma = \alpha E \approx 0.1$, while for metals $\Delta\sigma = \alpha E \approx 1$ (Ashby, 1999).

Differential scanning calorimetry is an experimental method of thermal analysis that is widely used to study thermal transitions, i.e., solid-solid transitions as well as solid-liquid and various other transitions and reactions. The experiment is performed by supplying the necessary heat to a test sample as well as a calibrated sample so that a given temperature rate of change is achieved for both. Excluding the temperatures at which transitions happen, a material with a larger heat capacity will require more energy. If exothermic heat flow is considered, the glass transition will appear as a step, cold crystallization as a dip, and the melting of crystalline structures as a peak, with the heat capacity of the material being what is measured if these features are removed (Lukas and LeMaire, 2009).

Pope (Pope, 1976) obtains three types of endotherms when studying the melting behavior of samples of oriented low-density polyethylene (LDPE) as a function of annealing temperature and time, subsequent heat treatment, and irradiation dose. These correspond to the primary melting of the lamellae, the melting of the reorganization products during the scan, and the melting of material crystallized during cooling from the original annealing temperature. The effect of ionizing radiation on the melting behavior of high-density and low-density polyethylene is also examined with data obtained by differential scanning calorimetry by Zoepfl and coworkers (Zoepfl et al., 1984). The data provided by Blumm and coworkers (Blumm et al., 2010) for PTFE makes apparent that the solid-solid transition occurs at $23.5\,°\mathrm{C}$, connected to change in crystalline structure of the polymer, and that the melting of the crystalline phase at $337.3\,°\mathrm{C}$, both as peaks in the results. In the experimental results provided by Panowicz and coworkers (Panowicz et al., 2021) for PET in the form of exothermic heat flow, the glass transition is apparent as a step around $90\,°\mathrm{C}$, and the melting of crystallites formed during secondary and primary crystallization as dips, the latter much larger than the former.

Regarding the experimental determination of the specific heat capacity of semi-crystalline polymers employing DSC, Blumm and coworkers (Blumm et al., 2010) report an almost constant value, which ranges from arround $1000\,\mathrm{J\,kg^{-1}\,K^{-1}}$ at $0\,°\mathrm{C}$ to $1500\,\mathrm{J\,kg^{-1}\,K^{-1}}$ at $300\,°\mathrm{C}$. This agrees with the value of $\rho C_p \approx 3 \times 10^{6}\,\mathrm{J\,m^{-3}\,K^{-1}}$, which according to Ashby (Ashby, 1999) is true for all solids, employing considerations from statistical mechanics.

Finally, Blumm and coworkers (Blumm et al., 2010) also supply the thermal diffusivity of PTFE found by employing laser flash techniques. In addition to the change in the crystalline structure of the material already mentioned, the glass temperature is also detectable as a step. The values of the thermal diffusivity ranged from $0.24\,\mathrm{mm}^2/\mathrm{s}$ to $0.13\,\mathrm{mm}^2/\mathrm{s}$, between $-110\,°\mathrm{C}$ and $140\,°\mathrm{C}$. The authors combine the heat capacity, density, and thermal diffusivity measurements to compute the

thermal conductivity of the polymer, which is approximately constant across the range of temperatures studied, $0.31 \, \mathrm{W \, m^{-1} \, K^{-1}}$, except for the moment when the aforementioned solid-solid transition occurs. Both values of thermal diffusivity and conductivity for PTFE are in line with values reported in Ashby (1999) for other polymers and markedly lower than for ceramics and metals. Taking into account the relatively large values of the linear thermal expansion and the low thermal conductivity, polymers are more subject to heat distortion. This is because they combine a longer time to arrive at a uniform temperature with larger changes in size due to temperature differences when compared, for example, with metals.

Chapter 4

State of the art in thermomechanical semi-crystalline polymer modeling

The main goal of this chapter is to report on the semi-crystalline polymer modeling state of the art. The departure point is infinitesimal thermoviscoelasticity, as it is one of the simplest models available to describe time-dependent materials. A thorough exposition of its inadequacies in describing semi-crystalline polymers is supplied, motivating the introduction of more complex models. Nonlinear generalizations are considered by specifying nonlinear laws for the elastic and viscous elements in rheological models originating from infinitesimal viscoelasticity. Only properties of a homogenized single phase are taken into account in these models, employed chiefly in the description of plastic polymers. These are the most commonly available models in the literature, and a detailed overview is provided in this chapter. The caveats regarding the generalization to three dimensions and large deformations are explained, as well as how to introduce temperature into that description.

Following that is a description of models that distinguish between the crystalline and amorphous phases while only considering bulk crystallinity and no additional geometrical information. Finally, multiscale models with micro and mesostructure considerations are described.

4.1 Infinitesimal thermo-viscoelasticity

Given the modeling objectives specified in Chapter 3, infinitesimal viscoelasticity presents itself as a satisfactory starting point. Depending on the model, it can capture strain recovery, creep, stress relaxation, and the transient behavior under monotonic loading–these are essential features to describe the mechanical behavior of a semi-crystalline polymer.

Infinitesimal thermo-viscoelasticity, as presented in Christensen (2013), fits into the framework of materials with fading memory framework (see Section 2.3). It is

assumed that strains, $\boldsymbol{\varepsilon}$, are small, as well as the temperature difference with respect to some reference temperature, $\Delta T = T - T_0$. Employing the Stone-Weierstrass and Riesz representation theorem, the expression found for the free energy, discarding third-order effects, is

$$
\begin{aligned}
\rho \psi(t) = &\int_{-\infty}^{t} \boldsymbol{D}(t-\tau) : \frac{\partial \boldsymbol{\varepsilon}(\tau)}{\partial \tau} d\tau + \int_{-\infty}^{t} \beta(t-\tau) \frac{\partial \Delta T(\tau)}{\partial \tau} d\tau \\
&+ \frac{1}{2} \int_{-\infty}^{t} \int_{-\infty}^{t} \frac{\partial \boldsymbol{\varepsilon}(\eta)}{\partial \eta} : \boldsymbol{G}(t-\tau, t-\eta) : \frac{\partial \boldsymbol{\varepsilon}(\tau)}{\partial \tau} d\tau d\eta \\
&- \int_{-\infty}^{t} \int_{-\infty}^{t} \boldsymbol{\varphi}(t-\tau, t-\eta) : \frac{\partial \boldsymbol{\varepsilon}(\tau)}{\partial \tau} \frac{\partial \Delta T(\eta)}{\partial \eta} d\tau d\eta \\
&- \frac{1}{2} \int_{-\infty}^{t} \int_{-\infty}^{t} m(t-\tau, t-\eta) \frac{\partial \Delta T(\tau)}{\partial \tau} \frac{\partial \Delta T(\eta)}{\partial \eta} d\tau d\eta, \quad (4.1)
\end{aligned}
$$

where $\boldsymbol{D}$, β, $\boldsymbol{G}$, $\boldsymbol{\varphi}$ and m are appropriate functions describing material properties. In particular, the last three quantities are the counterparts in infinitesimal thermoviscoelasticity to the stiffness tensor, the coefficient of thermal stress, and the specific heat at constant deformation, respectively, in infinitesimal thermoelasticity.

The constitutive relations found concerning stress and entropy are

$$
\boldsymbol{\sigma}(t) = \int_{-\infty}^{t} \boldsymbol{G}(t-\tau, 0) : \frac{\partial \boldsymbol{\varepsilon}}{\partial \tau} d\tau - \int_{-\infty}^{t} \boldsymbol{\varphi}(0, t-\tau) \frac{\partial \Delta T(\tau)}{\partial \tau}, \tag{4.2}
$$

$$
\rho s(t) = \int_{-\infty}^{t} \boldsymbol{\varphi}(t-\tau, 0) : \frac{\partial \boldsymbol{\varepsilon}}{\partial \tau} + \int_{-\infty}^{t} m(t-\tau, 0) \frac{\partial \Delta T(\tau)}{\partial \tau}. \tag{4.3}
$$

Regarding dissipation, its magnitude is of second order and, as such, can be discarded in this infinitesimal theory. This implies a small perturbation away from thermodynamic equilibrium.

The stress-strain relationship for the isothermal case is given by a convolution integral, coinciding with the description of a linear time-invariant system (LTI), as

$$
\boldsymbol{\sigma}(t) = \int_{0}^{t} \boldsymbol{G}(t-\tau) : \frac{\partial \boldsymbol{\varepsilon}(\tau)}{\partial \tau} d\tau, \tag{4.4}
$$

where $\boldsymbol{G}$ is the relaxation modulus of the material.

Furthermore, in some cases, this description is equivalent to an ordinary differential equation involving stress, strain, and their corresponding time derivatives. Often, these can be identified with the behavior of linear rheological models, which provide a visual counterpart and help in the interpretation of the model. These are one-dimensional mechanical models containing diverse arrangements of linear springs and dashpots. For an in-depth discussion on the connection between LTIs and ordinary differential equations, see Ciampa et al. (2019).

In general, the relaxation modulus can also be written as (Malkin and Isayev, 2017)

$$
G(t) = G_{\infty} + \varphi(t), \tag{4.5}
$$

where G_{∞} is the equilibrium modulus and φ is the relaxation function. Taking into account its physical meaning, the latter must be a decreasing function of time tending to zero as $t \to \infty$. The functions of such type can always be presented by the following integral

$$
\varphi(t) = \int_{0}^{\infty} H(\theta) e^{-t/\theta} d\theta, \tag{4.6}
$$

where θ denotes the relaxation time, and H is a function of the distribution of the relaxation times, the so-called relaxation time spectrum.

For example, considering the so-called Burgers material, the relaxation modulus, G, is given by (Malkin and Isayev, 2017)

$$G(t) = G_1 e^{-t/\theta_1} + G_2 e^{-t/\theta_2}, \tag{4.7}$$

where θ_i is the ith relaxation time so that the constitutive relation in the one-dimensional case is also given by

$$\sigma + \left(\frac{\eta_1}{G_1} + \frac{\eta_2}{G_2}\right)\dot{\sigma} + \frac{\eta_1\eta_2}{G_1 G_2}\ddot{\sigma} = (\eta_1 + \eta_2)\dot{\varepsilon} + \frac{\eta_1\eta_2(G_1 + G_2)}{G_1 G_2}\ddot{\varepsilon}, \tag{4.8}$$

where η_i is the viscosity of the ith dashpot, G_i is the stiffness of the ith spring, and $\dot{\bullet}$ denotes the derivative with respect to time. Given the definition in Equation (4.6), the relaxation time spectrum for the Burgers material is

$$H(\theta) = G_1\delta(\theta - \theta_1) + G_2\delta(\theta - \theta_2), \tag{4.9}$$

where δ is the δ-Dirac function. See Figure 4.8 for the corresponding rheological model.

Furthermore, the ordinary differential equations describing these models can be transformed into a state space representation, where the system's state is described through state variables. Also, for a Burgers material, an equivalent description can be established as

$$\sigma = G_1\varepsilon_{e,1} + G_2\varepsilon_{e,2}, \tag{4.10}$$

$$\dot{\varepsilon}_{e,1} = -\frac{\eta_1}{G_1}\varepsilon_{e,1} + \dot{\varepsilon}, \tag{4.11}$$

$$\dot{\varepsilon}_{e,2} = -\frac{\eta_2}{G_2}\varepsilon_{e,2} + \dot{\varepsilon}, \tag{4.12}$$

$$\tag{4.13}$$

where $\varepsilon_{e,i}$, $i = 1, 2$, is the strain in the ith spring and an internal variable of the constitutive model. Their evolution can be tied to transient effects, such as the ones observed at the beginning of the monotonic loading at a constant strain rate in the case of a Burger material (see Figure 4.1(a)). Figures 4.1(b) and 4.1(c) illustrate the response of the Burgers material to a constant strain and a constant stress, respectively, followed by release illustrating the ability of the model to capture the phenomena of strain recovery, creep, and recovery.

Linearity It is worth noting that infinitesimal thermoviscoelasticity is linear, in the sense that the response to the sum of two inputs is the sum of the responses to each of the inputs (see Figure 4.2). In the context of viscoelasticity, this principle is called the Boltzmann-Volterra superposition principle (Ward and Sweeney, 2004). Thus, in the one-dimensional case, for discrete increases in strain $\Delta\varepsilon_i$ at instants τ_i, $i = 1, 2, 3, \ldots$, the stress is given by

$$\sigma(t) = \Delta\varepsilon_1 G(t - \tau_1) + \Delta\varepsilon_2 G(t - \tau_2) + \Delta\varepsilon_3 G(t - \tau_3) + \cdots \tag{4.14}$$

If the increases in strain are assumed infinitesimal, the constitutive law found for the stress is the convolution integral in Equation (4.4). This is intrinsically connected to
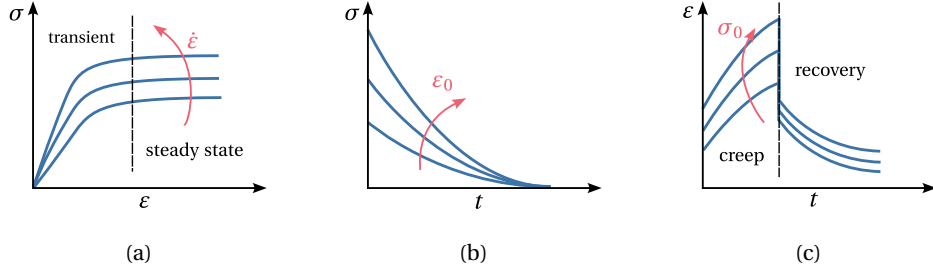
Figure 4.1: Schematic response of the Burgers material in (a) a constant strain rate experiment, (b) a stress relaxation experiment and a (c) creep experiment with recovery.

the fact that the rate equations for the state variables are ordinary differential equations (see Equation (4.10) for the Burgers material) and that as a material property, the relaxation modulus is only a function of time and not of strain, strain rate or stress (see Equation (4.7) for the Burgers material). The consequences of this linear behavior for the material's response in relevant mechanical experiments are discussed shortly.
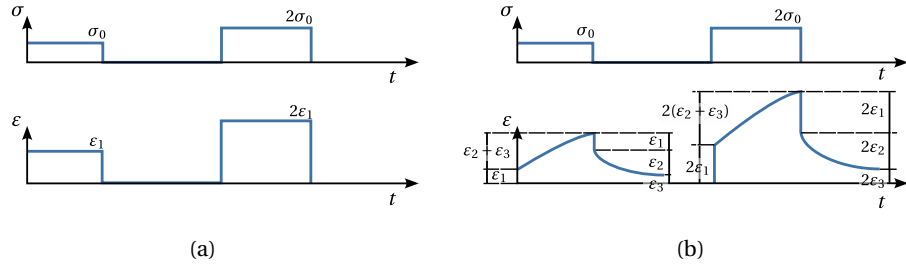
Figure 4.2: Stress driven linear response of (a) an elastic, and (b) a viscoelastic material. Adapted from Ward and Sweeney (2004).

Limitations of infinitesimal viscoelasticity   Infinitesimal viscoelasticity has, however, some significant limitations. The first among them is the use of infinitesimal strains in the constitutive description of the material. Semi-crystalline polymers, such as HDPE, can frequently achieve true strains in axial tests that exceed 1.5, far surpassing what could be considered small deformations (G'Sell and Jonas, 1981).

Furthermore, the Boltzmann superposition principle is frequently violated, and there is an energy exchange between the different relaxation modes, implying that the relaxation modulus depends on the strain, strain rate, and stress (Malkin and Isayev, 2017). Semi-crystalline polymers exhibit a nonlinear behavior that can be detected in a variety of mechanical experiments. References to experimental results depicting this behavior can be found in Section 3.2.2. A comparison between a linear response and possible nonlinear responses to the most common mechanical experiments is provided to understand the deficits of infinitesimal viscoelasticity.

Firstly, consider a set of constant strain rate experiments at different strain rates. At some point (see Equation (4.5)), a steady state will be reached, meaning $\dot{\boldsymbol{\alpha}} = 0$, and

the corresponding response in an infinitesimal viscoelastic model is either constant (liquid) or linear (solid) in the strain. At any rate, for a given strain, the stress varies linearly with the strain rate and is proportional to the relaxation time, corresponding to so-called Newtonian viscosity (Matsuoka, 1996) (see Figure 4.3(a)). Both of these facts are not always observed in practice. For example, HDPE displays a significant strain hardening, as shown, e.g., in the experimental results of G'Sell and Jonas (1981), which is not linear in the strain, i.e., the stiffness varies with the strain (see Figure 4.3(b)). Also, the stress corresponding to the steady state as a function of the strain rate often follows a power law (see, e.g., G'sell and Jonas (1979)) coinciding with so-called non-Newtonian viscosity (see Figure 4.3(a)). Besides this, Matsuoka (Matsuoka, 1996) emphasizes that the steady state stress grows unbounded with the strain rate according to infinitesimal viscoelasticity, which makes no physical sense. Also, some semi-crystalline polymers exhibit more or less abrupt changes in flow behavior at a given stress, which is akin to plastic yield in rate-independent plasticity (Bergström, 2015).

(a) (b)
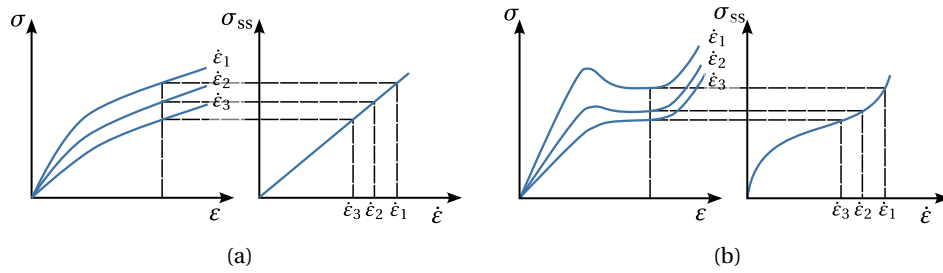
Figure 4.3: Stress-strain curve and steady state stress-strain rate curve for (a) an infinitesimal viscoelastic material (linear) and a (b) a nonlinear material.

The expected linear behavior in a stress relaxation experiment is to obtain the same stress response up to a multiplicative constant, which is the initial strain. Likewise, in a creep experiment, the strain response divided by the stress is equal for experiments at different stress levels. Another nonlinear feature observed in semi-crystalline polymers is the dependence of the relaxation modulus and creep compliance on the strain and stress, in addition to time. The recovery may also display nonlinear features, that is, the strain recovered ε_r will also depend on the initial strain ε_0 and on how long the sample was strained, t_0, yielding completely different $\varepsilon/\varepsilon_0$ versus $\log t/t_0$ curves (Ferry, 1980).

4.2 Finite linear viscoelasticity

The infinitesimal viscoelastic model can be derived assuming that the stress depends only on the "magnitude" of the deformation history to the first order (see Coleman and Noll (1961) or Christensen (2013)). This is automatically satisfied if only small strains are considered. However, Coleman and Noll (Coleman and Noll, 1961) point out that finite deformations can also be considered, as long as the motion is slow enough when compared with the material's rate of "forgetting." The stress-strain constitutive relation is still described as a convolution integral (see Equation (4.4)) and may be frequently described by ordinary differential equations, where instead of the infinitesimal strain tensor, a strain measure compatible with finite strains, e.g., the Green-Lagrange strain tensor, is employed. This approach to viscoelasticity allows for

finite strains. However, it is still linear with respect to the strain measure, not the displacement, since the former are nonlinear functions of the latter, thus, respecting the Boltzmann superposition principle and keeping the relaxation spectrum depending only on time. As such, this model does display most of the required nonlinear effects observed in semi-crystalline polymers described in the previous chapter. In addition, since the dissipation is a second-order effect, the state of the material remains close to thermodynamical equilibrium, so the dissipation does not contribute as a source in the heat conduction equation (Equation (2.14)).

4.3   Single integral models

Another approach that seeks to generalize the results of infinitesimal viscoelasticity is based on the integral constitutive equation for the stress as a function of the strain in Equation (4.4). These models include nonlinear phenomena while considering only small strains (Ward and Sweeney, 2004). For example, the model of Pipkin and Rogers is given by (Ward and Sweeney, 2004)

$$\sigma(t) = \int_{-\infty}^{t} R(t-\tau, \varepsilon(\tau)) \frac{\partial \varepsilon}{\partial \tau} \, d\tau, \tag{4.15}$$

where R is a nonlinear stress relaxation modulus depending on time and strain, incorporating nonlinear effects into the material's infinitesimal viscoelastic constitutive description.

A list of models of this type, including the models of Leaderman, Pipkin and Rogers; Schapery; and Bernstein, Kearsley and Zapas (BKZ), can be found in Ward and Sweeney (2004) and Malkin and Isayev (2017). According to Ward and Sweeney (Ward and Sweeney, 2004), Smart and Williams (Smart and Williams, 1972) assessed the three models' performance when applied to the tensile stretching of polypropylene and poly(vinyl chloride) fibers, but only up to modest strains (4%). At these strains, the BKZ model proved to be of limited interest, while the Pipkin and Rogers model, albeit simpler than Schapery's theory, yielded a somewhat inferior result. Moreover, Turner (Turner, 1966) concludes about single integral models that viscoelastic behavior, in general, cannot be discussed simply in terms of a stress-strain-time relationship and a modified superposition integral.

With particular relevance to modeling semi-crystalline polymers, Popelar (Popelar et al., 1990) modeled MDPE and HDPE employing Schapery's nonlinear viscoelasticity with good results. The experimental tests used for validation included constant strain rate uniaxial traction tests with strain rates ranging from $10^{-5} \, \text{s}^{-1}$ to $10^{-1} \, \text{s}^{-1}$, temperatures ranging from $23\,^\circ\text{C}$ to $77\,^\circ\text{C}$, and a maximum strain of 0.25.

Regarding the free energies corresponding to these stress-strain constitutive relationships, Gurtin and Hrusa (Gurtin and Hrusa, 1988) present a discussion on the topic. This class of models will not be discussed further in this text since, due to their formulation in terms of convolution integrals, they are not particularly appropriate for application in computational mechanics based on the FEM.

4.4   Descriptions based on rheological models with nonlinear elements

A viscoelastic constitutive model fit for large strains and capable of capturing the required nonlinear behaviors can often be achieved by specifying nonlinear laws for the behavior of the viscous and elastic elements in a rheological model. In what follows, well-established laws for both viscous and elastic elements are presented. The kinematic decomposition required to generate a large strain three-dimensional model and the introduction of the temperature field are discussed. Finally, the most relevant models from the literature following this approach are presented.

4.4.1   Viscous elements

As pointed out by Frost and Ashby (Frost and Ashby, 1982), plastic flow is a kinetic process. Therefore, the strength of a solid depends on both strain and strain rate, in addition to the temperature. This observation runs counter to the valuable concept of yield strength, below which there is no flow and above which flow is fast. According to the same authors, this would only be strictly true at absolute zero. The corresponding theoretical flow stress is often called the mechanical threshold or athermal strength. Furthermore, flow below that mechanical threshold is due to thermally activated kinetic processes, i.e., their rate depends on the thermal fluctuations of the kinetic units. For the sake of completeness, it should be mentioned that there are kinetic processes that become relevant when the loading exceeds the mechanical threshold, coinciding with very high strain rates, and which do not necessitate thermal activation to occur (Kocks et al., 1975)[1]. These are beyond the scope of the present work.

To better understand how thermal fluctuations allow for flow, consider that, at a given temperature, the kinetic units of a solid material perform thermally driven oscillations of random magnitude near an equilibrium position. If the motion of the kinetic units coincides with their permanence near that equilibrium state, the behavior of the solid is elastic. On the other hand, flow happens when the , H_0, bounding the equilibrium state is cleared. This energy is the energy of activation at $0\,\mathrm{K}$, when no force is acting on the material (Kocks et al., 1975). Employing the Boltzmann distribution from statistical mechanics to calculate the probability of a thermal fluctuation providing enough energy to overcome the energy barrier, the rate of transition between states is given in the form of the Arrhenius equation, written in this context as

$$k = A \exp\left(-\frac{H_0}{k_B T}\right), \tag{4.16}$$

where k_B is Boltzmann's constant, A is the pre-exponential factor, H_0 is the height of the energy barrier. The pre-exponential term can be interpreted as the rate of attempts to move over the transition state (Atkins and de Paula, 2010). According to Kocks and coworkers (Kocks et al., 1975), it is related to one of two extreme frequencies: either the "atomic" frequency, i.e., the frequency of uncorrelated atomic motions, or the kinetic unit ground frequency, correlated with the overcoming of many obstacles at the same

---

[1]In the context of polycrystalline materials, where slip is the primary deformation mechanism thermally activated deformation below the mechanical threshold corresponds to so-called jerky glide and deformation above the mechanical threshold to continuous glide (Kocks et al., 1975).
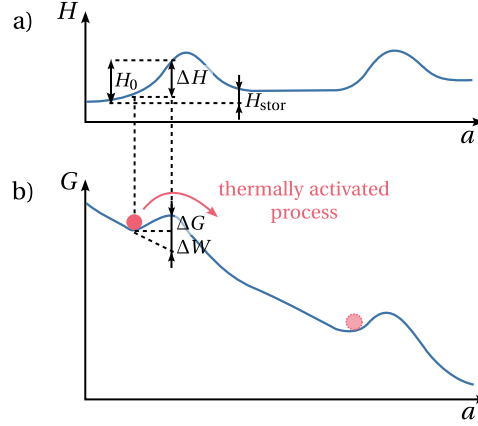
Figure 4.4: Transition of a kinetic unit between two states. a) Free energy, H, b) Free enthalpy, G, where a is the area swept by the kinetic unit.

time. The inverse of this rate, i.e.,

$$\theta = \frac{1}{A} \exp\left(\frac{H_0}{k_B T}\right), \tag{4.17}$$

is the relaxation time of the process.

To include the effect of applying a stress, τ, to the material, consider firstly that it leads to a new equilibrium position for the kinetic unit (see Figure 4.4). Taking into account the work provided by the stress before flow happens, the total free energy necessary to overcome the obstacle, H_0, is now smaller and equal to ΔH. The free Gibbs energy, also known as free enthalpy, ΔG, is the missing portion of energy that a thermal oscillation must supply for flow to happen. It is, however, not equal to ΔH, since during flow the stress will supply further work, ΔW, which must be discounted from the total energy required to overcome the kinetic unit's obstacle to motion. Thus, $\Delta G = \Delta H - \Delta W$. Without factoring in the thermal fluctuations, the motion would occur only if the work supplied by the stress was larger than the energy barrier. Moreover, if the free energy of the kinetic unit is greater after crossing the barrier, the plastic work is not entirely dissipated, and some energy remains latent in the material, H_{stor}. On the other hand, the free enthalpy of the kinetic unit is always lower after crossing the barrier; otherwise, there would be no greater probability of crossing in one direction than the other (see Figure 4.4). For more details, see Kocks et al. (1975).

Following the procedure outlined by Eyring (Eyring, 1936), the shearing force acting on the system and its effect on the flow of the kinetic units can be considered. Its presence will lead to a different rate of jumps in the forward and backward directions, which in energetic terms means lowering the energy of the final state and increasing the energy of the initial state. Assuming similar activation volumes, and subtracting the rate of kinetic units moving against the shearing force from those moving along with the shearing force, τ, the strain rate obtained is

$$\dot{\gamma} = \dot{\gamma}_0 \exp\left(-\frac{\Delta H}{k_B T}\right) \sinh\left(\frac{\nu \tau}{k_B T}\right), \tag{4.18}$$

where ν is the so-called activation volume, and it can be identified with the product of the area swept out by the mobile unit in moving from one local free energy minimum

to the next, and the resolved component of the distance moved by the kinetic unit in
the direction of the applied stress.

According to the same author, $\nu\tau$ is much smaller for an ordinary flow than $k_B T$.
Thus, the expression for Newtonian viscous flow is recovered as

$$\dot{\gamma} = \frac{\dot{\gamma}_0 \nu}{k_B T} \exp\left(-\frac{\Delta H}{k_B T}\right)\tau = \frac{1}{\eta}\tau, \tag{4.19}$$

where η is the viscosity. On the other hand, for plastic flow, where τ is large, the flow
rule is

$$\dot{\gamma} = \dot{\gamma}_0 \exp\left(-\frac{\Delta H - \nu\tau}{k_B T}\right) = \dot{\gamma}_0 \exp\left(-\frac{\Delta G(\tau)}{k_B T}\right), \tag{4.20}$$

which coincides with a negligible rate in the backward direction, and where $\nu\tau$ is
identified with the activation work such that $\Delta G = \Delta H - \nu\tau$. The contribution of
hydrostatic pressure can also be accounted for in this framework in a similar way to
the shearing force, i.e.,

$$\dot{\gamma} = \dot{\gamma}_0 \exp\left(-\frac{\Delta H - \nu\tau + \Omega p}{k_B T}\right), \tag{4.21}$$

where Ω is the activation volume corresponding to the hydrostatic pressure. This
relationship can be justified in terms of experimental results, where the stress
response of polymers shows a pressure dependence, in part due to the low bulk
moduli of polymers (≈ 5 GPa, compared with metals ≈ 100 GPa). A suitable expression
for the effective stress on the kinetic units is a linear combination of shear stress and
hydrostatic pressure, similar to the Mohr-Coloumb yield criterion (Ward and Sweeney,
2004). The expressions show that higher shear stresses lead to higher flow rates, with
the hydrostatic pressure having the reverse effect.

According to Fotheringham and Cherry (Fotheringham and Cherry, 1978), the
activation volumes in the forward and backward directions are not necessarily the
same. However, note that this is irrelevant when describing plasticity, as only one
activation volume must be considered. In fact, more general rate equations for
thermally activated flow can be found in Brinkman and Schwarzl (1957) or Kocks et al.
(1975).

The experimental determination of the parameters in these models is discussed,
e.g., in Evans and Rawlings (1969), Conrad (1970) and Kocks et al. (1975), through the
use of differential tests, changes of strain rate in a constant strain rate test, or stress
level steps in a creep experiment.

Roberston (Robertson, 1966) presents an alternative to the Eyring model
applicable to glassy polymers. The author considers a molecular model in which the
shear-stress field is introduced as a bias on the rotational conformation of backbone
bonds. The temperature at which the maximum fraction of flexed bonds is observed is
estimated and inserted into the WLF equation to compute the corresponding viscosity,
and hence the equation for the strain rate. Comparisons with results for PS and PMMA
are provided. Duckett and coworkers (Duckett et al., 1970) also employ this model to
fit the responses of PMMA and PET.

El-Qoubaa and Othman (El-Qoubaa and Othman, 2016) provide an implicit flow
rule while seeking to model the yield stress of PEEK as a function of the strain rate and
the temperature. The equation proposed is

$$\tau = \frac{k_B T}{\nu(\dot{\gamma}, T)} \ln\left(\frac{\dot{\gamma}}{\dot{\gamma}_0}\right), \tag{4.22}$$

where the activation volume, v, depends on the strain rate and the temperature according to

$$v(\dot{\gamma}, T) = v_0(T) \exp\left(-\sqrt{\frac{\dot{\gamma}}{\dot{\gamma}_c(T)}}\right), \tag{4.23}$$

$$v_0(T) = v_1 + v_2 \left(\frac{T}{T_g}\right)^n, \tag{4.24}$$

$$\dot{\gamma}_c(T) = \dot{\gamma}_1 \exp(qT), \tag{4.25}$$

T_g is the glass transition temperature, and τ_1, m, r, v_0, v_1, n, $\dot{\gamma}_1$ and q are material constants. The authors find a good agreement between the model and experimental data.

The models described so far are often termed velocity-controlled, as they assume that yield (see Remark 3.1) will occur when the strain rate of the viscous element, identified with the movement of kinetic units, is equal to the impressed rate of deformation (Fotheringham and Cherry, 1978). These models can also be thought of as specifying that the presence of stress causes an increase in pre-existing flow processes in the material, such that the stress corresponding to their flow equals the loading stress (Ward and Sweeney, 2004).

Notice that despite mentioning the existence of deformation mechanisms corresponding to the motion of kinetic units, the models presented in the previous paragraphs do not attempt to model the specific physical events directly. Alternatively, in the case of nucleation-controlled models for polymer plastic flow, the free enthalpy is directly modeled to determine the energy required in the nucleation and motion of the kinetic units (Fotheringham and Cherry, 1978; Ward and Sweeney, 2004).

Argon (Argon, 1973) proposes a model for plastic deformation of glassy polymers where the deformation mechanism is the buckling of the polymer chains via the action of a pair of opposed kinks. The expression found for the free enthalpy is

$$\Delta G(\tau) = \frac{3\pi\mu\omega^2 a^3}{16(1-\nu)}\left[1 - \left(\frac{\tau}{\hat{\tau}}\right)^{5/6}\right], \tag{4.26}$$

where μ and ν are the shear modulus and Poisson coefficient, respectively, $\hat{\tau}$ is the athermal strength defined as

$$\hat{\tau} = \frac{0.077\mu}{1-\nu}, \tag{4.27}$$

ω is the net angle of rotation of the molecular segment between the initial and activated configurations, and a is the mean molecular radius. The relationship between the athermal strength and the shear modulus in Equation (4.27) can be used to establish the temperature dependence of the athermal strength (Hao et al., 2022a). In the case of amorphous polymers, however, Ward and Sweeney (Ward and Sweeney, 2004) mention that computer simulations of polymer chains at the atomic level on both glassy atactic polypropylene and polycarbonate did not yield a dominant deformation mechanism that should be the target of modeling.

Turning to semi-crystalline polymers, the picture changes in the sense that, as reviewed in the previous chapter (Chapter 3), the plastic behavior of the material is tightly linked to deformation mechanisms in the crystalline phase. There is extensive modeling of plastic behavior in polycrystalline solids with direct identification of the

kinetic units as dislocations in the crystal[2]. According to Kocks and coworkers (Kocks et al., 1975), their motion can be modeled as in Equation (4.20), where

$$\dot{\gamma}_0 = b\rho_m L \nu_G, \tag{4.28}$$

where b is the Burgers vector[3] with dimensions of length, ρ_m is the mobile dislocation density with dimensions of dislocation length per unit volume, L the mean path of a mobile dislocation between inception and arrest at an obstacle and ν_G the frequency factor associated with the attempt rate of the nucleation process. At still moderate stresses, the average velocity is mainly controlled by thermally activated processes where the dislocations wait until a thermal fluctuation allows them to clear the obstacle.

Argon (Argon, 2013) presents the three relevant modes of dislocation nucleation in polymer lamellae as the nucleation of a monolithic straight screw-dislocation line from the edge of a lamella (mode A), nucleation of a screw-dislocation half loop from the narrow edge of a lamella (mode B), and nucleation of an edge-dislocation half loop from the wide face of a lamella (mode C). The respective free enthalpies for each mode are

$$\Delta G_A(\tau) = \frac{\mu b^2}{4\pi} \ln\left(\frac{\hat{\tau}}{\tau}\right), \tag{4.29}$$

$$\Delta G_B(\tau) = \frac{\mu b^2}{4\pi} \frac{1 - (\tau/\hat{\tau})^{2/3}}{(\tau/\hat{\tau})^{1.25}}, \tag{4.30}$$

$$\Delta G_C(\tau) = \frac{\mu b^3}{1 - \nu} \frac{1 - (\tau/\hat{\tau})^{1/3}}{(\tau/\hat{\tau})^{1.15}}. \tag{4.31}$$

Expressions for the mobile dislocation density are also presented by the same author as

$$\rho_m = \frac{\chi p N \lambda}{\lambda \Lambda^2}, \tag{4.32}$$

where λ is the length of the dislocation produced, p the probability of a successful nucleation event at a site, χ is the level of crystallinity, and $N = 2\Lambda/h$ is the number of possible nucleation sites in the representative volume $\lambda \Lambda^2$ allocated to a lamella, and h is the interplanar spacing. The mobile dislocation density, ρ_m, or the ideal shear force, $\hat{\tau}$, can also be taken as an internal variable and made to evolve according to a rate equation. See Klahn et al. (1970) and Kocks et al. (1975) for thorough discussions on modeling the deformation mechanisms in crystalline solids.

For an amorphous or semi-crystalline polymer, Equations (4.20) and (4.28) can still be employed, with a slightly different interpretation for the quantities involved and keeping in mind that the kinetic units are not as precisely defined as in the case of crystalline solids. Thus, the strain rate is still given by

$$\dot{\gamma} = b\rho_m \bar{v}_m, \tag{4.33}$$

i.e., by the product of the density of kinetic units responsible for the deformation, ρ_m, the amount of displacement per kinetic unit, b, and their average velocity, $\bar{v}_m$. This

---

[2]A dislocation loop can be defined as the demarcation line, in one slip plane, between an area that has slipped and a surrounding area that has not (Kocks et al., 1975).

[3]The Burgers vector is a vector that represents the magnitude and direction of the lattice distortion resulting from a dislocation in a crystal lattice.

velocity is approximately given by

$$\bar{v}_m = L v_G \exp\left(-\frac{\Delta G(\tau)}{k_B T}\right),$$

(4.34)

where L is the mean free path of the kinetic unit, v_G is the rate of attempts to move over the obstacle impeding its motion, and the Arrhenius term is the probability that the thermal fluctuations will supply the energy necessary to overcome the obstacle (G'Sell and Jonas, 1981; Gilman, 1992).

Finally, one must keep in mind that both the nucleation and velocity-controlled models produce similar expressions, but their interpretations differ (Fotheringham and Cherry, 1978).

The deformation mechanism discussed so far concern the motion of kinetic units by themselves. However, some kinetic processes are cooperative, occurring only when several kinetic units act in unison. In fact, Cherry and Holmes (Cherry and Holmes, 1969) mention that the fitted values to the activation volume in Eyring's model are too large to agree with their corresponding physical interpretation (see Equation (4.18).) To model this situation, Fotheringham and Cherry (Fotheringham et al., 1976; Fotheringham and Cherry, 1978) assume that n kinetic units, all following the Eyring model, are needed to substantiate a deformation mechanism. The expression found for the flow rate is

$$\dot{\gamma} = \dot{\gamma}_0 \sinh^n\left(\frac{v\tau}{2kT}\right)\exp\left(-\frac{n\Delta H}{kT}\right),$$

(4.35)

where the notation employed retains its meaning from the previous paragraphs, and a temperature below the glass transition temperature is assumed. Richeton and coworkers (Richeton et al., 2005) seek to model the yield stress of amorphous polymers, extending the cooperative model to temperatures above the glass transition temperature. They achieve this by proposing

$$\dot{\gamma} = \dot{\gamma}_0 \exp\left(\frac{\ln 10 \cdot c_1^g (T - T_g)}{c_2^g + T - T_g}\right)\sinh^n\left(\frac{v\tau}{2kT}\right)\exp\left(-\frac{\Delta H}{kT_g}\right),$$

(4.36)

for temperatures above T_g, where c_1^g and c_2^g are the WLF parameters (Ward and Sweeney, 2004). These authors (Richeton et al., 2007) also compare the models of Eyring (see Equation (4.18)), Argon (see Equation (4.26)) and their cooperative model in the prediction of PMMA's and PC's yield stress.

Other models, however, do not fit neatly into the scheme outlined above. Power laws are fairly common empirical laws for the flow rule (Brown and Ashby, 1980). They are given, for example, as (Bergström, 2015)

$$\dot{\gamma} = \dot{\gamma}_0 \left(\frac{\tau}{\hat{\tau}}\right)^m,$$

(4.37)

where m is a material parameter and $\hat{\tau}$ a reference stress. Perzyna (Perzyna, 1963), e.g., proposes

$$\dot{\gamma} = \frac{1}{\mu}\left(\frac{\langle \tau - \hat{\tau} \rangle}{\hat{\tau}}\right)^{1/\epsilon},$$

(4.38)

to describe the rate sensitivity of plastic materials, where $\langle \bullet \rangle$ denotes the ramp function, defined as $\langle x \rangle = (|x| + x)/2$, and μ and ϵ are material parameters. Another law available

for the strain rate is (Kelly and Gillis, 1974; Bodner and Partom, 1972)

$$\dot{\gamma} = \dot{\gamma}_0 \exp\left(-\left(\frac{\hat{\tau}}{\tau}\right)^n\right), \tag{4.39}$$

where n is a material parameter. According to Bodner and Partom (Bodner and Partom, 1972), this last set of laws are suggested by both direct measurements and theoretical considerations of the average velocity of mobile dislocations as a function of the applied stress in polycrystalline solids (see Equation (4.28)).

Yet another model available in the literature, based on reptation (Doi and Edwards, 1978), is described by Bergström and Boyce (Bergström and Boyce, 1998, 2001). The flow is due in part to the Brownian motion of the polymer chains, in addition to thermally activated events, yielding the following flow rule

$$\dot{\gamma} = C_1 (\lambda_{\text{chain}} - 1 + \xi)^{C_2} \left(\frac{\tau}{\hat{\tau}}\right)^m, \tag{4.40}$$

where λ_{chain} is the chain stretch and C_1, C_2, m and $\hat{\tau}$ are material parameters. The constant $\xi \approx 0.01$ is introduced to eliminate the singularity at $\lambda_{\text{chain}} = 1$.

According to de Souza Neto and coworkers (de Souza Neto et al., 2008), more flow rules can be generated by multiplying several simpler laws, including those already provided. For example, assuming that $\dot{\gamma}$ is a function of the stress, time, and temperature, one can write

$$\dot{\gamma} = \dot{\gamma}(\tau, t, T) = f_\sigma(\tau) f_t(t) f_T(T), \tag{4.41}$$

where f_τ, f_t and f_T are possibly experimentally defined functions.

Structure variables So far, all the constitutive descriptions provided for the strain rate neglect the material's thermomechanical history. As already discussed in Section 2.3, a set of appropriate internal variables, in this context, also called structure variables (see Kocks et al. (1975) and Frost and Ashby (1982)), is employed to capture the contribution of the material's history to its thermomechanical response. Thus, the implicit assumption so far is either that the structure remains constant during flow, i.e.,

$$\boldsymbol{\alpha} = \boldsymbol{\alpha}_0, \tag{4.42}$$

or that it has reached a steady state, i.e.,

$$\dot{\boldsymbol{\alpha}} = \mathbf{0}. \tag{4.43}$$

Either of these hypotheses is often unreasonable and fails to explain the nonlinear behavior of polymers. This shortcoming is evident in the ability to capture the shape of the transient in a constant strain rate test, be it the characteristic strain softening of many glassy polymers or the double yield of various semi-crystalline polymers. The most common targets of modeling are the athermal strength, $\hat{\tau}$, and the mobile dislocation density, ρ_m, (see Equations (4.20) and (4.28)).

Regarding the athermal strength $\hat{\tau}$, two natural assumptions are that it may depend on the plastic strain γ and time. Thus, by the chain rule, one finds

$$\dot{\hat{\tau}} = h\dot{\gamma} - r, \tag{4.44}$$

where $h \equiv \partial\hat{\tau}/\partial\gamma|_t$ corresponds to a hardening rate and $r \equiv -\partial\hat{\tau}/\partial t|_\gamma$ denotes a recovery or, in the case of polymers, also an aging rate. Hardening is expected if there is an increase in the number of obstacles to the motion of the kinetic unit (Kocks et al., 1975; Hasan and Boyce, 1995). The minus sign in the recovery/aging rate definition is introduced to enforce a decrease in the athermal strength connected to either recovery or aging. That said, Boyce and coworkers (Boyce et al., 1988) conclude that aging in PVC may increase its strength.

Bodner and Partom (Bodner and Partom, 1975) propose

$$\hat{\tau} = \hat{\tau}_1 + (\hat{\tau}_0 - \hat{\tau}_1)\exp\left(-\frac{m}{\hat{\tau}_0}w^p\right), \tag{4.45}$$

where $\hat{\tau}_0$ and $\hat{\tau}_1$ are the initial and final athermal strengths, respectively, and m is a material property. Compared with the original text, a multiplicative factor $((n+1)/n)^{1/n}$ is neglected as it tends to 1 for large n. In the one-dimensional case, the plastic work, w^p, is defined as $\int \tau\dot{\gamma}\,dt$. The corresponding rate equation can be written as (Zaïri et al., 2007)

$$\dot{\tau} = m\left(\frac{\hat{\tau}_1 - \hat{\tau}}{\hat{\tau}_0}\right)\dot{w}^p. \tag{4.46}$$

Zaïri and coworkers (Zaïri et al., 2007) propose similar rate equations for partial contributions, $\hat{\tau}^{(1)}$ and $\hat{\tau}^{(2)}$, to the athermal strength, $\hat{\tau}$, when modeling glassy polymers. The former concerns the hardening effect of the network alignment, such that the corresponding rate equation is defined as

$$\dot{\tau}^{(1)} = m\left(\frac{\hat{\tau}^{(1)} - (1-\alpha)\hat{\tau}_0^{(1)}}{\hat{\tau}_0^{(1)}}\right)\dot{w}^p, \tag{4.47}$$

where m is material parameter, $\hat{\tau}_0^{(1)}$ is the initial athermal strength and α a hardening parameter. In turn, the latter accounts for the effect of strain softening, with the corresponding rate equation given as

$$\dot{\tau}^{(2)} = p\left(\frac{\hat{\tau}_1^{(2)} - \hat{\tau}^{(2)}}{\hat{\tau}_1^{(2)}}\right)\dot{w}^p, \tag{4.48}$$

where p is a material parameter and $\hat{\tau}_1^{(2)}$ is a final partial athermal strength, such that

$$\dot{\tau} = \dot{\tau}^{(1)} + \dot{\tau}^{(2)}. \tag{4.49}$$

The solution to both equations can be found by substituting the appropriate values into Equation (4.46).

Note that the use of plastic work instead of the plastic strain in the definition of the rate equations just discussed is often equivalent. This is because the mapping between the two can be made one-to-one such that $\hat{\tau}(\gamma) = \tilde{\tau}(w^p) \equiv \hat{\tau}(w^p(\gamma))$. See de Souza Neto et al. (2008) for the complete derivation.

Boyce and coworkers (Boyce et al., 1988) propose an entirely similar rate equation for the athermal strength in a glassy polymer. The corresponding strain softening is described as

$$\dot{\tau} = h\left(1 - \frac{\hat{\tau}}{\hat{\tau}_1(T,\dot{\gamma})}\right)\dot{\gamma}, \tag{4.50}$$

employing, however, the strain rate as the "driving force" behind its change. The initial structure is represented by the value of $\hat{\tau}$ at the upper yield point, $\hat{\tau}_0$, h is the slope of the yield drop with respect to the strain, $\hat{\tau}_1$ is the value of $\hat{\tau}$ reached at the steady state, i.e., the "preferred" structure, and, as indicated, $\hat{\tau}_1$ may depend on temperature and strain rate. This choice for the rate equation of the athermal strength enables modeling the distinctive glassy polymer strain softening.

In their attempt to model semi-crystalline polymers, Ahzi and coworkers (Ahzi et al., 2003) propose

$$\dot{\hat{\tau}} = \frac{\hat{\tau}}{n}\left(\frac{\hat{\tau}_0}{\hat{\tau}}\right)^n \dot{\gamma}, \tag{4.51}$$

as the rate equation for the athermal strength $\hat{\tau}$, where $\hat{\tau}_0$ is the corresponding initial value and n is a hardening coefficient.

Seeking to model the effect of manufacturing-induced voids in polymer-based composites, Chowdhury and coworkers (Chowdhury et al., 2008) present an extension of Equation (4.50). It describes the transition from a pre-defined initial yield stress, $\hat{\tau}_0$, to a peak yield stress, $\hat{\tau}_1$, followed by strain softening to a saturated state, $\hat{\tau}_2$. The corresponding rate equation is

$$\dot{\hat{\tau}} = H_1(\gamma)\left(1 - \frac{\hat{\tau}}{\hat{\tau}_1}\right)\dot{\gamma} + H_2(\gamma)\left(1 - \frac{\hat{\tau}}{\hat{\tau}_2}\right)\dot{\gamma}, \tag{4.52}$$

with the smooth Heaviside-like functions H_i, $i = 1, 2$ given by

$$H_1(\gamma) = -h_1\left\{\tanh\left(\frac{\gamma - \gamma^p}{f\gamma^p}\right) - 1\right\}; \quad H_2(\gamma) = h_2\left\{\tanh\left(\frac{\gamma - \gamma^p}{f\gamma^p}\right) + 1\right\}, \tag{4.53}$$

where h_1 and h_2 are the hardening (softening) parameters, f the smoothing factor and γ^p the plastic strain at the peak yielding point. This approach is also pursued by Hao and coworkers (Hao et al., 2022a), where a fourth athermal shear stress $\hat{\tau}_3$ is considered, connected to the yield of the crystalline phase in a semi-crystalline polymer. According to the authors, this property can depend on temperature, strain rate, crystallinity, and humidity. The rate equation for the athermal strength $\hat{\tau}$ is given similarly to Equation (4.52) as

$$\dot{\hat{\tau}} = H_1(\gamma)\left(1 - \frac{\hat{\tau}}{\hat{\tau}_1}\right)\dot{\gamma} + H_2(\gamma)\left(1 - \frac{\hat{\tau}}{\hat{\tau}_2}\right)\dot{\gamma} + H_3(\gamma)\left(1 - \frac{\hat{\tau}}{\hat{\tau}_3}\right)\dot{\gamma}, \tag{4.54}$$

The corresponding smooth functions, H_i, $i = 1, 2, 3$, are given by

$$H_1(\gamma) = -h_1\left\{\tanh\left(\frac{\gamma - \gamma^{p,1}}{f\gamma^{p,1}}\right) - 1\right\}, \tag{4.55}$$

$$H_2(\gamma) = h_2\left\{-\tanh\left(\frac{\gamma - \gamma^{p,1}}{f\gamma^{p,1}}\right)\tanh\left(\frac{\gamma - \gamma^{p,2}}{f\gamma^{p,2}}\right) + 1\right\}, \tag{4.56}$$

$$H_3(\gamma) = h_3\left\{\tanh\left(\frac{\gamma - \gamma^{p,2}}{f\gamma^{p,2}}\right) + 1\right\}, \tag{4.57}$$

where h_1, h_2 and h_3 are the hardening (softening) parameters, f is the smoothing factor, (chosen as 0.3), $\gamma^{p,1}$ is the plastic strains at the peak yielding point, and $\gamma^{p,2}$ is the

low yield point just before the yielding of the crystal structure takes place. This last parameter may depend on both the strain rate and the temperature according to the authors.

In G'Sell and Jonas (1981), the authors discuss modeling the density of kinetic units instead of the strength of the obstacles impeding their motion. They aim to capture the strain softening/inverse transient in glassy polymers, also verified for semi-crystalline polymer at large strains. They propose that whenever a polymer experiences a strain rate increase or decrease, the density of kinetic units changes linearly over a particular strain interval until it reaches the new equilibrium value characteristic of the new strain rate.

Multiple groups of kinetic units The motion of several different kinetic units contributes to the material's flow behavior, as discussed in the previous chapter (Chapter 3). Ree and Eyring (Ree and Eyring, 1955) assume that they can be classified based on an average relaxation time that varies significantly between them. A single group is also made up of many types of kinetic units with different relaxation times but can be adequately described by an average value for the group. Assuming that each group behaves according to the previously described Eyring model, the shear stress is expressed as follows

$$\tau = \sum_{k=1}^{n} x_k \tau_k = \sum_{k=1}^{n} x_k \frac{k_B T}{v_k} \sinh^{-1}\left(\frac{\dot{\gamma}}{\dot{\gamma}_0} \exp\left(\frac{\Delta H}{k_B T}\right)\right), \tag{4.58}$$

where x_k is the area fraction swept by the kth kinetic unit during its movement.

Roetling mentions that the Ree-Eyring model with two flow groups describes the tensile yield strength of PMMA, below the glass transition temperature (Roetling, 1965), and iPP, above the glass transition temperature (Roetling, 1966), well in the strain rate range of $10^{-5}\,\mathrm{s}^{-1}$ to $1\,\mathrm{s}^{-1}$. The author suggests a connection between the α and β relaxation transitions and these two flow groups.   Other authors have successfully captured the strain rate and temperature dependence of the yield strength of glassy polymers using the Ree-Eyring model and variations thereof (Bauwens et al., 1969; Bauwens, 1972; Bauwens-Crowet, 1973; Haussy et al., 1980).

This approach of Ree and Eyring allows for the inclusion of different deformation mechanisms in the model. It can be interpreted as a rheological model where dashpots arranged in parallel materialize different deformation mechanisms, coinciding with rheological models such as those discussed in Section 4.4.6. Furthermore, using the fraction of area swept by each kinetic unit to weigh their contribution to the total stress is analogous to popular approaches in semi-crystalline polymer modeling, where crystallinity is incorporated similarly (see Section 4.6).

Generalization to three-dimensions The models discussed so far concern one-dimensional flow, i.e., laws for the scalar strain rate $\dot{\gamma}$. For three-dimensional models apt to describe large deformations, it is necessary to provide a macroscopic flow rule, i.e., a law prescribing the spatial velocity gradient $\boldsymbol{L}$.

Consider the flow rule for the Newtonian fluid without the pressure term to see how this might be accomplished in the isotropic situation,

$$\boldsymbol{D} = \mathsf{S} : \boldsymbol{\sigma}, \quad \boldsymbol{W} = \boldsymbol{0}, \tag{4.59}$$

where **S** is the appropriate compliance tensor, defined as

$$\mathbf{S} = \frac{1}{2\eta}\left(\mathbf{I}_S - \frac{1}{3}\boldsymbol{I}\otimes\boldsymbol{I}\right) + \frac{1}{9\kappa}\boldsymbol{I}\otimes\boldsymbol{I},\tag{4.60}$$

where η and κ are the dynamic and bulk viscosity, and $\mathbf{I}_S$ is the fourth-order symmetric identity tensor. Equation (4.59) can be rewritten as

$$\boldsymbol{D} = \frac{\|\boldsymbol{s}\|}{2\eta}\frac{\boldsymbol{s}}{\|\boldsymbol{s}\|} + \frac{\sigma_m}{3\kappa}\boldsymbol{I}.\tag{4.61}$$

To establish the connection with the one-dimensional flow rules already presented, consider a pure shear flow with a strain rate equal to $\dot{\gamma}$. The shear stress found from Equation (4.61) is

$$\tau = \eta\dot{\gamma}.\tag{4.62}$$

τ is identified with $\|\boldsymbol{s}\|$ to generalize from pure shear to a three-dimensional stress state. Thus one can substitute $\|\boldsymbol{s}\|/\eta = \dot{\gamma}_{\text{dev}}$, and $\sigma_m/\kappa = \dot{\gamma}_{\text{vol}}$, found employing a similar logic, yielding

$$\boldsymbol{D} = \frac{\dot{\gamma}_{\text{dev}}}{2}\boldsymbol{N}_{\text{dev}} + \frac{\dot{\gamma}_{\text{vol}}}{3}\boldsymbol{N}_{\text{vol}},\tag{4.63}$$

where

$$\boldsymbol{N}_{\text{dev}} = \frac{\boldsymbol{s}}{\|\boldsymbol{s}\|}, \quad \boldsymbol{N}_{\text{vol}} = \boldsymbol{I},\tag{4.64}$$

and $\dot{\gamma}_{\text{dev}}$ is found from the laws described in previous paragraphs, with $\tau = \|\boldsymbol{s}\|$ and $p = \text{tr}(\boldsymbol{\sigma})/3$. So far, no laws were suggested for the volumetric strain rate, $\dot{\gamma}_{\text{vol}}$. When included, it is often chosen to coincide with the Newtonian fluid (see Equation (4.61)). Most often, the factors 1/2 and 1/3 in Equation (4.59) are neglected, perhaps because the flow rule contains a leading term that absorbs the missing elements during calibration.

4.4.2 Yield criteria

The yield stress is not as clearly defined for polymers as for metals far below their melting point. This difficulty in the definition of yield stress occurs because, for many polymers, flow is detected at all stress levels and does not start at some characteristic yield stress. See Remark 3.1 for a more detailed clarification.

Notwithstanding, a yield criterion, Φ, can still be used to set the flow rule, defining the flow potential Ψ appropriately. Choosing the flow potential equal to the yield surface, $\Psi = \Phi$, the flow direction is computed as

$$\boldsymbol{D} = \dot{\gamma}\boldsymbol{N} = \dot{\gamma}\frac{\partial\Phi}{\partial\boldsymbol{\sigma}},\tag{4.65}$$

being perpendicular to the yield surface in the stress domain. The choice of $\dot{\gamma}$ in rate-independent plasticity is made to satisfy the loading-unloading conditions

$$\dot{\gamma} \geq 0, \quad \Phi(\boldsymbol{\sigma}, \boldsymbol{A}) \leq 0, \quad \Phi(\boldsymbol{\sigma}, \boldsymbol{A})\dot{\gamma} = 0.\tag{4.66}$$

However, in the present context, an explicit expression for $\dot{\gamma}$ like the ones presented in Section 4.4.1 should be used.

Ghorbel (Ghorbel, 2008) provides a detailed description of the yield criteria employed to describe polymers. The most common criteria are the von Mises, Mohr-Coloumb, Drucker, and Raghava yield (Balieu et al., 2014) criteria.

4.4.3 Elastic elements

The elastic elements employed in the models under discussion typically fit into two classes: linear elasticity and rubber-like elasticity. The former are based on the equation for isotropic linear elasticity in small deformations, given by

$$\boldsymbol{\sigma} = \mathbf{D} : \boldsymbol{\varepsilon}, \tag{4.67}$$

where $\mathbf{D}$ is the isotropic elastic modulus defined as

$$\mathbf{D} \equiv 2G\mathbf{I}_S + \left(K - \frac{2}{3}G\right) \boldsymbol{I} \otimes \boldsymbol{I}, \tag{4.68}$$

where G is the shear modulus, K is the bulk modulus, $\boldsymbol{I}$ is the second order identity tensor and $\mathbf{I}_S$ is the symmetric identity[4]. A possible way to extend this model to large deformations is to use, for example, the Hencky strain tensor, $\boldsymbol{\varepsilon}^{(0)} \equiv \ln \boldsymbol{V}$, where $\boldsymbol{V}$ is the left stretch tensor, instead of the infinitesimal strain tensor. Taking into account that the respective conjugate is the Kirchhoff stress tensor, $\boldsymbol{\tau}$, the so-called Hencky model defines the following stress-strain constitutive relation

$$\boldsymbol{\tau} = \mathbf{D} : \boldsymbol{\varepsilon}^{(0)}. \tag{4.69}$$

This can also be achieved by employing as the strain measure the Green-Lagrange strain tensor, $\boldsymbol{E}^{(2)} \equiv (\boldsymbol{U}^2 - \boldsymbol{I})/2$, the so-called Saint-Venant-Kirchhoff model

$$\boldsymbol{S} = \mathbf{D} : \boldsymbol{E}^{(2)}, \tag{4.70}$$

taking into account that the appropriate stress conjugate is the second Piola-Kirchhoff stress tensor, $\boldsymbol{S}$.

In modeling plastic polymers, models based on non-Gaussian statistical theory for rubber-like elasticity are the most common choice (Holzapfel, 2000). Even so, for reference, the Neo-Hookean model's expression of stress is

$$\boldsymbol{\sigma} = \lambda_0 J^{-1} \ln J \boldsymbol{I} + \mu_0 \left(\boldsymbol{b} - \boldsymbol{I}\right), \tag{4.71}$$

where λ_0 and μ_0 are material properties and $\boldsymbol{b}$ is the left Cauchy-Green strain tensor.

The most widely used model is the eight-chain model of Arruda and Boyce (Arruda and Boyce, 1993; Arruda et al., 1995), which takes into account the deformation behavior of elastomer microstructures. It is assumed that the macromolecules, or chain molecules are, on average, located along the diagonals of a unit cell in the principal stretch space. The expression found for the stress is

$$\boldsymbol{\sigma} = \frac{N k_B T}{3J} \frac{\lambda^{\text{lock}}}{\overline{\lambda^*}} \mathscr{L}^{-1} \left(\frac{\overline{\lambda^*}}{\lambda^{\text{lock}}}\right) \text{dev}[\boldsymbol{b}^*] + K[J-1]\boldsymbol{I}, \tag{4.72}$$

where N, λ^{lock} and K are material parameters, $\boldsymbol{b}^* \equiv (J)^{-2/3}\boldsymbol{b}$, $\overline{\lambda^*} \equiv [\text{tr}(\boldsymbol{b}^*)/3]^{1/2}$, and the Langevin function is defined by

$$\mathscr{L}(\beta) = \coth \beta - \frac{1}{\beta}. \tag{4.73}$$

---

[4]The symmetric identity $\mathbf{I}_S$ is defined as $(\mathbf{I}_S)_{ijkl} = \frac{1}{2}(\delta_{ik}\delta_{jl} + \delta_{il}\delta_{jk})$ where δ_{ij} is the Kronecker delta, such that $\mathbf{I}_S : \boldsymbol{A} = \boldsymbol{A} : \mathbf{I}_S = \text{sym}(\boldsymbol{A})$, with $\boldsymbol{A}$ being a second order tensor.

As the chain stretch hits its limiting value, this choice for functional dependency results
in an asymptotically increasing stress.

A three-chain model can also be adopted as proposed by Wang and Guth (Wang
and Guth, 1952). The expression for the principal components of the stress is

$$\sigma_i = \frac{Nk_BT}{3J}\lambda^{\text{lock}}\left[\lambda_i\mathscr{L}^{-1}\left(\frac{\lambda_i}{\lambda^{\text{lock}}}\right) - \frac{1}{3}\sum_{j=1}^{3}\lambda_j\mathscr{L}^{-1}\left(\frac{\lambda_j}{\lambda^{\text{lock}}}\right)\right]. \tag{4.74}$$

Another alternative is presented by Edward and Vilgis (Edwards and Vilgis, 1986),
postulating the free energy as

$$\psi_{EV}(\lambda_1,\lambda_2,\lambda_3) = \frac{1}{2}N_c\left\{\frac{\sum_{i=1}^{3}\left(1-\alpha^2\right)\lambda_i^2}{1-\alpha^2\bar{Z}\lambda_i^2} - \log\left(1-\alpha^2\sum_{i=1}^{3}\lambda_i^2\right)\right\} +$$

$$+ \frac{1}{2}N_s\left[\sum_{i=1}^{3}\left\{\frac{\lambda_i^2(1+\eta)\left(1-\alpha^2\right)}{\left(1+\eta\lambda_i^2\right)\left(1-\alpha^2\sum_i\lambda_i^2\right)} + \log\left(1+\eta\lambda_i^2\right)\right\} - \log\left(1-\alpha^2\Sigma\lambda_i^2\right)\right], \tag{4.75}$$

where λ_i are the principal stretches, α is a measure of the inextensibility and η of the
slippage, N_c is the number of crosslinks and N_s the number of slip links. The stress is
found from the constitutive relation in Equation (2.5).

4.4.4   Caveats regarding the generalization to three-dimensions and large deformations

Before proceeding, some comments about developing a fully three-dimensional large
strain model based on a one-dimensional rheological model are in order. When
considering only infinitesimal strains, the strain applied to elements in series is added
together, whereas elements in parallel are subjected to the same strain. For example,
for the model in Figure 4.5, the strain across the elements on the first branch is
decomposed additively, $\boldsymbol{\varepsilon} = \boldsymbol{\varepsilon}^e + \boldsymbol{\varepsilon}^p$, being the same across both branches. A suitable
kinematic decomposition must be chosen to achieve an appropriate generalization to
three dimensions and large deformations.   The basis for this choice is the
multiplicative elastoplastic decomposition of the deformation gradient (de Souza Neto
et al., 2008)

$$\boldsymbol{F} = \boldsymbol{F}^e\boldsymbol{F}^p, \tag{4.76}$$

where $\boldsymbol{F}$ is the deformation gradient and superscripts e and p correspond to the
elastic and plastic parts. In practice, elements in parallel will experience the same
strain gradient, whereas elements in series will divide the deformation using a
multiplicative decomposition. See Figure 4.5 for reference. Since, in general, the
deformation gradients are not commutative, the choice for the order is relevant.

Focusing on a decomposition between an elastic, denoted here by e, and a viscous
element, denoted here by p, the application of the decomposition in Equation (4.76)
to the definition of the spatial velocity gradient (see Section 2.1) yields

$$\boldsymbol{L} = \boldsymbol{L}^e + \boldsymbol{F}^e\boldsymbol{L}^p(\boldsymbol{F}^e)^{-1}, \tag{4.77}$$
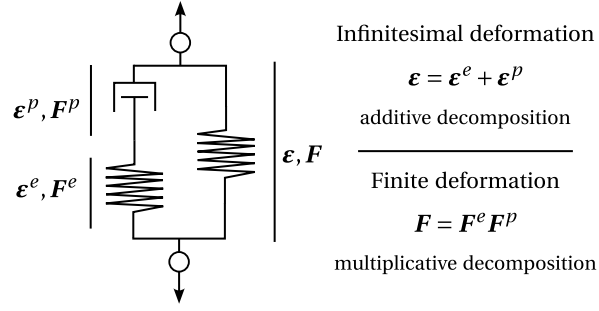
Figure 4.5: Additive and multiplicative strain decomposition corresponding to infinitesimal and finite deformations, respectively.

where $\boldsymbol{L}^e$ and $\boldsymbol{L}^p$ are defined as

$$\boldsymbol{L}^e = \boldsymbol{F}^e (\boldsymbol{F}^e)^{-1}, \tag{4.78}$$

$$\boldsymbol{L}^p = \boldsymbol{F}^p (\boldsymbol{F}^p)^{-1}. \tag{4.79}$$

The constitutive description is most often supplied as a law for $\boldsymbol{D}^p$ and $\boldsymbol{W}^p$, where

$$\boldsymbol{D}^p = \mathrm{sym}(\boldsymbol{L}^p), \quad \boldsymbol{W}^p = \mathrm{skew}(\boldsymbol{L}^p). \tag{4.80}$$

A common approach is (de Souza Neto et al., 2008)

$$\bar{\boldsymbol{D}}^p \equiv \boldsymbol{R}^{eT} \boldsymbol{D}^p \boldsymbol{R}^e = \dot{\gamma}_{\mathrm{dev}} \boldsymbol{N}_{\mathrm{dev}} + \dot{\gamma}_{\mathrm{vol}} \boldsymbol{N}_{\mathrm{vol}}, \tag{4.81}$$

$$\bar{\boldsymbol{W}}^p \equiv \boldsymbol{R}^{eT} \boldsymbol{W}^p \boldsymbol{R}^e = \boldsymbol{0}, \tag{4.82}$$

with $\boldsymbol{R}^e$ defined by the polar decomposition theorem as $\boldsymbol{F}^e = \boldsymbol{R}^e \boldsymbol{U}^e$. This yields the plastic spatial velocity gradient

$$\boldsymbol{L}^p = \boldsymbol{R}^{eT} (\dot{\gamma}_{\mathrm{dev}} \boldsymbol{N}_{\mathrm{dev}} + \dot{\gamma}_{\mathrm{vol}} \boldsymbol{N}_{\mathrm{vol}}) \boldsymbol{R}^e, \tag{4.83}$$

and the elastic spatial velocity gradient

$$\boldsymbol{L}^e = \boldsymbol{L} - (\dot{\gamma}_{\mathrm{dev}} \boldsymbol{N}_{\mathrm{dev}} + \dot{\gamma}_{\mathrm{vol}} \boldsymbol{N}_{\mathrm{vol}}). \tag{4.84}$$

An alternative description can be given as

$$\frac{1}{2} \pounds_v \boldsymbol{b}^e = -(\dot{\gamma}_{\mathrm{dev}} \boldsymbol{N}_{\mathrm{dev}} + \dot{\gamma}_{\mathrm{vol}} \boldsymbol{N}_{\mathrm{vol}}) \boldsymbol{b}^e, \tag{4.85}$$

where $\pounds_v \boldsymbol{b}^e$ is the Lie derivative of $\boldsymbol{b}^e$ with respect to the velocity field $\boldsymbol{v}$.

One can also and prescribe a law for $\boldsymbol{D}^p$ directly (Boyce et al., 1988),

$$\boldsymbol{D}^p = \dot{\gamma}_{\mathrm{dev}} \boldsymbol{N}_{\mathrm{dev}} + \dot{\gamma}_{\mathrm{vol}} \boldsymbol{N}_{\mathrm{vol}}, \tag{4.86}$$

$$\boldsymbol{W}^p = \boldsymbol{0}, \tag{4.87}$$

or follow Bergström (Bergström, 2015)

$$\tilde{\boldsymbol{D}}^p \equiv \mathrm{sym}((\boldsymbol{F}^e)^{-1} \boldsymbol{L}^p \boldsymbol{F}^e) = \dot{\gamma}_{\mathrm{dev}} \boldsymbol{N}_{\mathrm{dev}} + \dot{\gamma}_{\mathrm{vol}} \boldsymbol{N}_{\mathrm{vol}}, \tag{4.88}$$

$$\tilde{\boldsymbol{W}}^p \equiv \mathrm{skew}((\boldsymbol{F}^e)^{-1} \boldsymbol{L}^p \boldsymbol{F}^e) = \boldsymbol{0}, \tag{4.89}$$

which is equivalent to Equation (4.81) elastoplastic isotropy (de Souza Neto et al., 2008) is assumed.

4.4.5 Inclusion of the thermal field

Including temperature-dependent material parameters is insufficient to consider the thermal field when employing constitutive descriptions based on rheological models. The first missing feature of such a model would be that a change in temperature, with null stress, would not lead to a contraction or dilation. Similarly, a temperature change while preventing expansion/contraction would lead to zero stress. To fix this omission, an additional thermal configuration can be considered, e.g.,

$$\boldsymbol{F} = \boldsymbol{F}^{\text{mech}} \boldsymbol{F}^{\text{th}}, \tag{4.90}$$

where $\boldsymbol{F}^{\text{mech}}$ and $\boldsymbol{F}^{\text{th}}$ are the deformation gradients concerning only the mechanical and temperature fields, respectively. Note that the reverse order for the deformation gradients can be considered, as well as decompositions where the thermal deformation gradient is applied between elastic and plastic deformation gradients (Arruda et al., 1995).

When employing the models described so far, consider that an increase in the temperature with no mechanical loading applied leads to a null stress response from the "mechanical part," thus, its corresponding deformation gradient will be unitary, making the total deformation gradient equal to the thermal deformation gradient, $\boldsymbol{F} = \boldsymbol{F}^{\text{th}}$. Taking inspiration from infinitesimal thermoelastic theory, one can write

$$\boldsymbol{F}^{\text{th}} = (1 + \alpha(T)\Delta T)\boldsymbol{I}. \tag{4.91}$$

Lu and Pister (Lu and Pister, 1975) suggest, however,

$$\boldsymbol{F}^{\text{th}} = \upsilon(T)\boldsymbol{I}, \tag{4.92}$$

where υ is a scalar-valued function of temperature, reflecting intrinsic thermal expansion characteristics of the material of the body

$$\upsilon(T) = \exp\left[\int_{T_0}^{T} \alpha(T^*) \, dT^*\right], \tag{4.93}$$

where α is the coefficient of linear thermal expansion, allowed to depend on the temperature. In particular, if α is independent of temperature, Equation (4.93) reduces to

$$\upsilon(\Delta T) = \exp(\alpha \Delta T). \tag{4.94}$$

Further, if the conditions for infinitesimal thermal strain are satisfied, i.e., $\alpha \Delta T \ll 1$, one finds Equation (4.91).

Looking at the energy balance equation (Equation (2.14)), the internal dissipation and the Gough-Joule effect still need to be added to the present analysis. In the one-dimensional rheological model, the dissipation is due to the linear dashpots,

$$\mathscr{D}_{\text{int}}^{i} = \sigma^{i}\dot{\gamma}^{i}, \tag{4.95}$$

where $\dot{\gamma}^{i}$ and σ^{i} are the strain rate and stress in the dashpot i. In three dimensions, this rational yields

$$\mathscr{D}_{\text{int}}^{i} = \chi_{\text{d}}\boldsymbol{\sigma}_{i} : \boldsymbol{D}^{i}, \tag{4.96}$$

where $\boldsymbol{\sigma}^{i}$ is the Cauchy stress tensor across the ith viscous elements and $\boldsymbol{D}^{i}$ the corresponding rate of deformation tensor. $\chi_{\text{d}} \in [0,1]$ is a constant dissipation factor,

commonly chosen in the range $\chi_d \approx 0.85$ to 0.95 for metals (Simo and Miehe, 1992a) and equal to 1 for polymers (Okereke and Akpoyomare, 2019; Hao et al., 2022b). The possibility of $\chi_d < 1$ materializes the fact that some plastic work may be stored in the material.

The thermoelastic Gough-Joule effect can be written as

$$\mathscr{H}^e = -\rho_0 T \frac{\partial \boldsymbol{P}}{\partial T} : \dot{\boldsymbol{F}}, \tag{4.97}$$

discarding the contribution from the dissipation, following Simo and Mihe (Simo and Miehe, 1992a) – compare with the full equation for the elastoplastic Gough-Joule effect (Equation (2.12)).

The considerations given in this section are rendered useless if the model is formulated employing a free energy which depends also on the temperature, e.g., those models described in Anand et al. (2009); Ames et al. (2009).

4.4.6   Models available in the literature

The next set of models corresponds to generalizations of various infinitesimal viscoelastic models that use the previously described nonlinear elements in the corresponding rheological models.

Generalization of the Maxwell model   The Maxwell model is given as

$$\sigma + \frac{\eta}{E}\dot{\sigma} = \eta\dot{\varepsilon}, \tag{4.98}$$

corresponding to the rheological model in Figure 4.6. An early improvement to

Figure 4.6: Rheological model corresponding to the Maxwell model.

describe the large-strain behavior of elastomers is presented by Smith (Smith, 1962). The Bodner-Partom material model (Bodner and Partom, 1975) is another generalization of the same constitutive description. It can simulate the behavior of a visco-elastoplastic material under small strains and arbitrary loading history. The elastic element obeys Hooke's law, and the flow rule is given by Equations (4.86) and (4.39), with the athermal strength evolving according to Equation (4.46). The model can describe a rate-sensitive response and hardening. However, it cannot display strain recovery. Based on this work, the rate equations in Equation (4.49) for $\hat{\tau}$, in conjunction with a power law (see Equation (4.37)) have been used in models describing poly(methyl methacrylate) (PMMA), a glassy polymer, by Zaïri and coworkers (Zaïri et al., 2005, 2007, 2008), to describe HDPE by Zhang and Moore (Zhang and Moore, 1997), and to describe PC by Frank and Brockman (Frank and Brockman, 2001). It has also been used to model the behavior of metallic alloys at high temperatures (de Souza Neto et al., 2008).

In the same vein, Ben Hadj Hamouda and coworkers (Ben Hadj Hamouda et al., 2007) employ a Double Inelastic Deformation (DID) model—whose background is

described in detail by Cailletaud and Saï (Cailletaud and Saï, 1995). Formulated in
small strains, an additive split is assumed between a linear strain and two viscoplastic
strains, corresponding to the deformation mechanism in the amorphous and
crystalline phases. Each viscoplastic strain follows a power law (see Equation (4.37))
with a von Mises yield criterion, accounting also for nonlinear kinematic hardening.
The authors use it to model the response of MDPE subject to constant strain rate
uniaxial tension experiments, as well as stress relaxation and dip tests. Balieu and
coworkers (Balieu et al., 2014) also present a model that can be interpreted as a
nonlinear Maxwell model. It is formulated employing hypoelasticity, with the plastic
flow rule deduced from Raghava's criterion modified to include an isotropic damage
variable representing the micro-voids and micro-cracks developed in the material.
The law for the strain rate is a power law (see Equation (4.37)), and the authors
employ an integral-type nonlocal damage model to describe mineral-filled
semi-crystalline polymers.

Standard Linear Solid   The following set of models are generalizations of the so-called
standard linear solid model. In the context of infinitesimal viscoelasticity, it can be
expressed in equivalent ways in its Maxwell or its Kelvin-Voigt representation, as shown
in Figure 4.7 with the constitutive differential equations for the stress and the strain
given as

$$\sigma + \frac{\eta}{E_2}\dot{\sigma} = E_1\varepsilon + \frac{\eta\left(E_1 + E_2\right)}{E_2}\dot{\varepsilon}, \quad \text{(Maxwell representation)}, \tag{4.99}$$

$$\sigma + \frac{\eta}{E_1 + E_2}\dot{\sigma} = \frac{E_1 E_2}{E_1 + E_2}\varepsilon + \frac{E_1\eta}{E_1 + E_2}\dot{\varepsilon}, \quad \text{(Kelvin-Voigt representation)}, \tag{4.100}$$

where in both equations, the terms containing the strain, ε, are the stress response in
equilibrium.
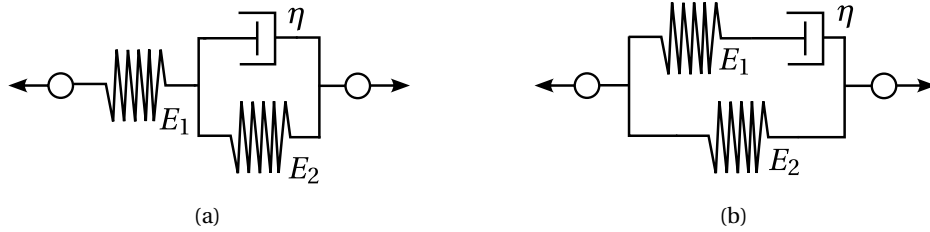
Figure 4.7: Rheological model for the standard linear solid: (a) Maxwell representation;
(b) Voigt representation.

The viscoplasticity theory based on overstress (VBO) was introduced by Cernocky
and Krempl (Cernocky and Krempl, 1980) and is based on the standard linear solid.
The so-called overstress is the difference between the full stress and the equilibrium
part, which is allowed to be a nonlinear function of the strain. Thus, Equation (4.99)
and (4.100) can be written as

$$\sigma - f(\varepsilon) = M\dot{\varepsilon} - K\dot{\sigma}, \tag{4.101}$$

where f may be a nonlinear function of the strain, and M and K are general functions
of the stress, the strain, and their derivatives. It has been used to successfully model

metals (Liu and Krempl, 1979; Yao and Krempl, 1985) as well as polymers, such as polypropylene (Kitagawa et al., 1989), polyethylene (Kitagawa and Takagi, 1990), nylon 66, polyetherimide, poly(ether ether ketone) (Krempl and Ho, 2000), and polyphenylene oxide (PPO) (Colak, 2005). More advanced versions of this approach include kinematic and isotropic hardening and strain softening through appropriate internal variables (Krempl and Ho, 2000; Ho and Krempl, 2002).

Concerning the generalization of the Maxwell representation, Simo (Simo, 1987) and Reese and Govindjee (Reese and Govindjee, 1998) consider nonlinear elastic elements in the rheological model. The first author employs the analytical solution for the ordinary differential equations describing the standard linear solid model, yielding a representation for the isochoric part of the stress as a convolution integral, i.e.,

$$S = Jp C^{-1} + J^{-2/3} \operatorname{dev}[H], \tag{4.102}$$

$$H = \int_0^t (\iota + (1 - \iota) e^{-(t-\tau)/T}) \frac{d}{d\tau} \left\{ \operatorname{dev} \left[\frac{\partial \bar{\psi}_{\mathrm{EQ}}(\bar{E}(\tau))}{\partial \bar{E}} \right] \right\} d\tau, \tag{4.103}$$

where ι is a parameter such that $\iota = 0$ coincides with the Maxwell model for the isochoric part of the stress and $\iota = 1$ to the elastic solid, θ is the relaxation time, $\bar{E}$ is the Green-Lagrange strain tensor computed from the volume-preserving part of the deformation gradient $\bar{F} \equiv J^{-1/3} F$, and $\bar{\psi}_{\mathrm{EQ}}$ is the equilibrium term in the free energy.

On the other hand, Reese and Govindjee (Reese and Govindjee, 1998) opt for a rate equation for the elastic left Chauchy-Green strain tensor coinciding with a Newtonian fluid (see Equation (4.61) and (4.85)), employing a multiplicative split for the deformation gradient. Accordingly, the second Piola-Kirchhoff stress tensor is given as

$$S = S_{EQ} + S_{NEQ} = \underbrace{2 \frac{\partial \psi_{EQ}}{\partial C}}_{S_{EQ}} + \underbrace{2 (F^i)^{-1} \cdot \frac{\partial \psi_{NEQ}}{\partial C^e} \cdot (F^i)^{-T}}_{S_{NEQ}} = 2 \frac{\partial \psi}{\partial C}, \tag{4.104}$$

where S_{EQ} and S_{NEQ} are the stresses corresponding to equilibrium and non-equilibrium, respectively. Appropriate choices for the free energy Ψ yield different nonlinear elastic elements.

Polanco-Loria and coworkers (Polanco-Loria et al., 2010) present their generalization, which allows for hyperelastic-viscoplastic response due to intermolecular resistance and entropic hyperelastic response due to the re-orientation of molecular chains. The stress in the Maxwell branch is determined from an isotropic compressible Neo-Hookean material (see Equation (4.71)). At the same time, the flow in the dashpot is controlled by Raghava's yield criterion, which is pressure sensitive (see Section 4.4.2). A non-associative viscoplastic flow potential is employed, allowing for volumetric plastic strain. Finally, the eight-chain model gives the deviatoric part of the stress on the other branches, including a volumetric part similar to the one shown in Equation (4.71) for the Neo-Hookean model. The authors validated their models against experimental results obtained for polypropylene samples.

That said, the most popular thermoplastic models are generalizations of the Voigt version of the standard solid. Halsey and coworkers (Halsey et al., 1945) present one of the earliest contributions considering an Eyring dashpot as the viscous element in an attempt to model the behavior of fibers. Likewise, Haward and Thackray (Haward and Thackray, 1968) proposed one of the first models for thermoplastic polymers below the glass transition temperature. The elastic element in the Maxwell branch is still a

linear spring. However, the elastic element parallel to it is a Langevin spring, while the viscous element is an Eyring dashpot. The model is formulated assuming small strains and is restricted to one-dimensional loading.

Later, Boyce and coworkers (Boyce et al., 1988) generalized this model to three dimensions, among other additions. A multiplicative kinematic split between the elastic and inelastic deformation is enforced, as described in Section 4.4.4. The linear spring is generalized to three dimensions and large deformation employing the Hencky model (see Equation (4.69)), with shear and bulk moduli being temperature dependent. The thermally activated process is now nucleation controlled by employing the model proposed by Argon (Argon, 1973) (see Equation (4.26)) with the addition that the athermal strength $\hat{\tau}_0$ is replaced by an internal variable, $\tilde{\tau}$, which is given by $\tilde{\tau} = \hat{\tau} + \alpha p$, where $p = -\sigma_m$ and α is a material property. The rate equation for the athermal strength, $\hat{\tau}$, is chosen according to Equation (4.50), such that the distinctive strain softening of glassy polymers is captured. The model does not account for volumetric flow. Lastly, the three-chain model gives the stress in the other elastic element (see Equation (4.74)), responsible for the strain hardening. For other contributions exploring this model while employing different rubber-like elasticity models see, e.g., Arruda and Boyce (1993); Arruda et al. (1995); Wu and Van Der Giessen (1993); Buckley and Jones (1995); Sweeney and Ward (1995). In fact, the most widely used model of this type is the so-called Arruda-Boyce model (Arruda and Boyce, 1993; Arruda et al., 1995), which employs an eight-chain model for the rubber-elastic element.

Also expanding on the model of Boyce, Parks, and Ahzi (Boyce et al., 1988) (BPA model), Chowdhury and coworkers (Chowdhury et al., 2008) propose a very similar model in the context of manufacturing-induced voids in polymer-based composites, formulated, however hypoelastically. The model was later validated on epoxy resins by Poulain and coworkers (Poulain et al., 2014). As in the BPA model, the athermal strength (Equation (4.26)) is taken as an internal variable following a different rate equation (Equation (4.52)). This choice allows a smoother strain softening. Also, the response of the rubber-elastic element is now a linear combination of the response obtained from a three-chain model (Equation (4.74)) and an eight-chain model (Equation (4.72)). Hao and coworkers (Hao et al., 2022a) propose a very similar model, where the rate equation for the athermal strength is given by Equation (4.54), rendering a model able to capture the double yield phenomenon in semi-crystalline polymers. The last authors also take into account the thermomechanical aspects of polymer modeling, accounting for the self-heating, thermal softening, and temperature-dependent properties. They validate their model against experimental results obtained on epoxy, nylon101, and PA6.

Burgers material Another common material model in infinitesimal viscoelasticity is the so-called Burgers material, which incorporates viscous flow into the standard linear solid model. It also accepts two equivalent descriptions as

$$\sigma + \left(\frac{\eta_1}{E_1} + \frac{\eta_2}{E_2}\right)\dot{\sigma} + \frac{\eta_1\eta_2}{E_1 E_2}\ddot{\sigma} = (\eta_1 + \eta_2)\dot{\varepsilon} + \frac{\eta_1\eta_2(E_1 + E_2)}{E_1 E_2}\ddot{\varepsilon} \quad \text{(Maxwell representation)},$$

$$\tag{4.105}$$

$$\sigma + \left(\frac{\eta_1}{E_1} + \frac{\eta_2}{E_1} + \frac{\eta_2}{E_2}\right)\dot{\sigma} + \frac{\eta_1\eta_2}{E_1 E_2}\ddot{\sigma} = \eta_2\dot{\varepsilon} + \frac{\eta_1\eta_2}{E_1}\ddot{\varepsilon} \quad \text{(Kelvin-Voigt representation)}, \tag{4.106}$$
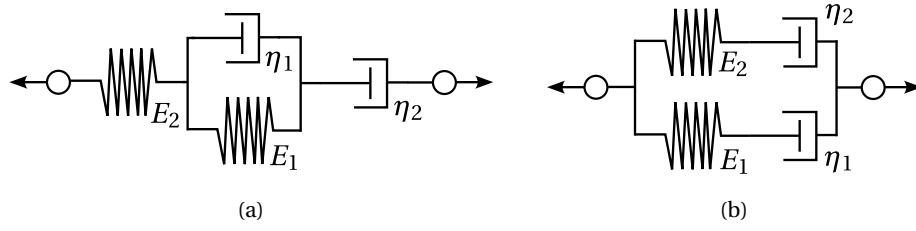
Figure 4.8: Rheological model for the Burgers material. a) Maxwell representation. b) Voigt representation.

in the context of small strains. See Figure 4.8 for the corresponding rheological models.

Bardenhagen and coworkers (Bardenhagen et al., 1997) propose a three-dimensional viscoplastic model for polymeric materials, which is a generalization of the Maxwell representation of the Burgers material. One of the branches is a three-dimensional large strain hypoelastic generalization of the Maxwell model. The other branch employs an associative hypoelastic elastoplastic model with the von Mises criterion as the yield criterion, including an isotropic hardening function. The authors provide a comparison with experimental results.

Boyce and coworkers (Boyce et al., 2000) also present a model generalizing the Maxwell representation of the Burgers material. One of the branches contains an elastic element following Hencky's model (see Equation (4.69)) and an Eyring dashpot, in the same way as the model already described in Boyce et al. (1988). In the other branch, the elastic element follows the eight-chain model (see Equation (4.72)), while the dashpot is similar to the Bergström-Boyce model (see Equation (4.40)). It is used by the authors to model poly(ethylene terephthalate) above the glass transition temperature, accounting for strain-induced crystallization. This is achieved by neglecting the last dashpot if the stretch is larger than a given value, which depends on the plastic strain rate and the temperature.

Kletschkowski and coworkers (Kletschkowski et al., 2002) present another description fitting into this class of material models. One of the Maxwell branches is made of a linear elastic spring and its viscous element follows the cooperative model (see Equation (4.35)) for the strain rate. The other branch employs the endochronic viscoplasticity theory (Valanis, 1970). It resembles viscoelasticity with the caveat that time is replaced by an "inner" time, a function of the strain, hence the name endochronic. The authors employ this model in the description of filled PTFE.

Pouriayevali and coworkers (Pouriayevali et al., 2013) present a constitutive model to describe the quasi-static and high strain rate, large deformation response of semi-crystalline polymers, which can be seen as a generalization of the Kelvin-Voigt representation of the Burgers material. The elastic elements are hyperelastic, and their stress response is obtained from Equation (2.5), given a suitable free energy potential. Regarding the viscous elements, element one obeys von Mises yield criterion with the strain rate also given by Equation (4.38), and the other obeys Newton's viscosity law (see Equation (4.59)) neglecting the volumetric contribution. The corresponding free energy, including the dependency on the temperature, is also supplied. The authors validate their model through comparisons with Nylon 6.

The dual network fluoropolymer model is presented in Bergström and Hilbert (2005) as an extension of the Bergström and Boyce (Bergström and Boyce, 1998) and

Arruda and Boyce (Arruda et al., 1995) models, generalizing the Kelvin-Voigt representation of the Burgers material. The Arruda-Boyce eight-chain model gives the response of both springs (see Equation (4.72)), with the response of the second element taken as a scalar factor $s^{(2)}$, a specified material parameter, times the expression employed to describe the response of the first evaluated according to the deformation gradient across element 2. The kinematic decomposition is as expected from the discussion in Sections 4.4.4 and 4.4.5, including a thermal deformation gradient. The rate equations for $\dot{\gamma}_{\text{dev}}^{(1)}$ and $\dot{\gamma}_{\text{vol}}^{(1)}$ in Equation (4.88) in the viscous element 1 are given similarly to the Bergström-Boyce model (see Equation (4.40)) multiplied by a power law, function of the stress and the temperature. The volumetric strain rate is given by Equation (4.61). The strain rate for the viscous element 2, $\dot{\gamma}_{\text{dev}}^{(2)}$, is given by

$$\dot{\gamma}_{\text{dev}}^{(2)} = \begin{cases} ab\left(\varepsilon - \varepsilon_0\right)^{b-1}\dot{\varepsilon} & \text{if } \tau > \sigma_0 \\ 0 & \text{otherwise} \end{cases}, \tag{4.107}$$

where $\varepsilon = \|\boldsymbol{E}^{(0)}\|$, $a > 0$, $b > 0$ and $\sigma > 0$ are material parameters, $\tau = \|\boldsymbol{s}\|$, which is similar to a von Mises yield criterion.

Generalized Maxwell model A generalized Maxwell model is one that contains n Maxwell branches in parallel. In addition, a single branch with only an elastic element may also be considered. See Figure 4.9 for the corresponding rheological model. This framework includes Maxwell representations for the standard linear solid model and the Burgers material. Models with more than two branches are considered in the following section.
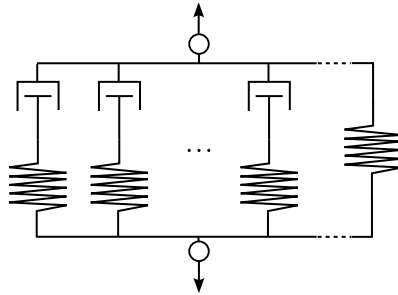
Figure 4.9: Rheological model for the generalized Maxwell model.

Holmes and coworkers (Holmes et al., 2006) present a large strain deformation elasto-viscoplastic material model for modeling semi-crystalline polymers. According to the authors, each of the branches in the model coincides with a mode of deformation, elastic, viscoelastic, and viscoplastic. Each of the elastic elements' response follows from the free energy potential chosen and the constitutive relation in Equation (2.5). The authors suggest employing an Ogden potential for the elastic and viscoelastic branches and a Saint Venant-Kirchhoff potential (see Equation (4.70)) for the viscoplastic contribution. The flow rule adopted follows the work of Brussele-Dupend and coworkers (Brusselle-Dupend et al., 2001, 2003) for semi-crystalline polypropylene, accounting for the inadequacies of the Eyring equation (see Equation (4.18)). Regarding the viscoplastic branch of the model, the strain rate is given by Equations (4.64) and (4.38).

Zeng and coworkers (Zeng et al., 2010) developed an elastoplastic constitutive model for semi-crystalline polymers under isothermal conditions between the glass transition temperature and the melting temperature under low-level strain rates, neglecting viscous effects. Each of the branches in the rheological model is based on physical considerations concerning the mesoscopic semi-crystalline structure. The foundational idea is a three-phase morphology depending on the average distance between crystalline blocks. The interaction is modeled as elastoplastic with linear hardening when the distance is small. For medium distances, the behavior is elastoplastic with perfect plasticity, and for large distances the material is modeled as following the eight-chain model (see Equation (4.72)). The authors validate the model against the results of uniaxial and biaxial experiments on polyamide 6 and polyethylene at different strain rates. The model parameters are easily calibrated using these uniaxial stress–strain experimental curves.

Okereke and Akpoyomare (Okereke and Akpoyomare, 2019) propose a model based on an elastic-viscoelastic-viscoplastic framework to predict the temperature and rate-dependent response of an incompressible semi-crystalline polymer. Three branches materialize it in a rheological model, two containing a viscous and an elastic element corresponding to the contribution of the mobile amorphous fraction, and the crystalline and rigid amorphous fractions, and another branch containing only an elastic element, representing the contribution of the entangled molecular network. The basis of this model is a one-process glass-rubber model for amorphous polymers (Buckley and Jones, 1995), adapted to the description of semi-crystalline polymers considering the α- and the β-processes, making it a two-process model. The authors connect these processes to the glass transition of the rigid amorphous and the mobile amorphous phases, respectively. The flow rule for both branches containing the viscous elements is given according to Equation (4.64), where the volumetric contribution is neglected, and the deviatoric strain rate is given by

$$\dot{\gamma}_{\text{dev, i}} = \dot{\gamma}_{T,j} \dot{\gamma}_{S,j} \dot{\gamma}_{\sigma,j} \dot{\gamma}_{0,j}, \quad j = \alpha, \beta, \tag{4.108}$$

where $\dot{\gamma}_{T,j}$ captures the influence of the temperature as

$$\dot{\gamma}_{T,j} = \exp\left(-\frac{\Delta H_j}{k_B T}\right), \tag{4.109}$$

and $\dot{\gamma}_{\sigma,j}$ captures the influence of the stress as

$$\dot{\gamma}_{\sigma,j} = \exp\left(\frac{\Omega \sigma_m}{k_B T}\right) \sinh\left(\frac{v\|\boldsymbol{s}\|}{2\sqrt{3}k_B T}\right), \tag{4.110}$$

according to Eyring's theory (see Equations (4.18) and (4.21)). The influence of the structure is taken into account through a fictive temperature, T_f, for each branch j as

$$\dot{\gamma}_{S,j} = \exp\left(\frac{C}{T_{f,j} - T_\infty}\right), \tag{4.111}$$

where C is the Cohen-Turnbull constant and T_∞ is the Vogel temperature. The pre-exponential factor is given by

$$\dot{\gamma}_{0,j} = \frac{G}{\tau_{0,j}^*} \frac{v}{k_B T} \exp\left(\left[\frac{\Delta H}{R \Delta T}\right]\left[\frac{C}{\Delta T_{f,j} - T_\infty}\right]\right), \tag{4.112}$$

where the superscript $*$ denotes a reference value and τ_0 is a relaxation time. The rate equation for the fictive temperature is given by

$$\dot{T}_{f,j} = (T - T_{f,j})\dot{\gamma}_{S,j}\dot{\gamma}_{T,j}\dot{\gamma}'_{0,j} + \kappa\|\boldsymbol{D}^{p,j}\|, \quad j = \alpha, \beta, \tag{4.113}$$

where κ is a material parameter and

$$\dot{\gamma}'_{0,j} = \frac{1}{\tau^*_{0,j}}\exp\left(\left[\frac{\Delta H}{R\Delta T}\right]\left[\frac{C}{\Delta T_{f,j} - T_\infty}\right]\right). \tag{4.114}$$

According to the authors, this choice of the rate equation for the fictive temperature incorporates into the model significant post-yield strain-softening observed in high-rate compression of propylene. The elastic elements in the branches contain viscous elements according to the Saint-Venant-Kirchhoff model (see Equation (4.70)), while the other elastic element follows the Edwards-Vilgis model (see Equation (4.75)).

The three network model is presented in Bergström (2015), being very similar to the models already presented based on a generalized Maxwell model. The springs follow the Arruda-Boyce eight-chain model (see Equation (4.72)) and the dashpots power laws (similar to Equation (4.37)). The effective shear stress is taken as an internal variable with a corresponding rate equation. A linear dependence on the temperature for the stress response of the elastic elements is also included. The same author also explores a parallel network model which consists in adding more Maxwell branches to the model following similar constitutive equations.

Hao and coworkers (Hao et al., 2022b) propose a model containing three branches to study the double yield phenomenon as well as the rate- and temperature-dependent thermomechanical response below the glass transition temperature of semi-crystalline polymers. The first branch contains an elastic element whose stress response follows Hencky's model (see Equation (4.69)). The corresponding viscous element obeys Equations (4.18) and (4.26) following the work of Boyce and coworkers (Boyce et al., 1988). The athermal strength is taken as an internal variable, and its rate equation is shown in Equation (4.52), following Chowdhury and coworkers (Chowdhury et al., 2008). The behavior of the elastoplastic branch coincides with rate-independent plasticity, and it is made up of an elastic element, also following Hencky's model (see Equation (4.69)), and a viscous element respecting a paraboloidal yield criterion. The yield criterion describing the yielding in the crystalline region is similar to the Drucker-Prager yield criterion with the strain rate/plastic multiplier $\dot{\gamma}$ found by taking into account the Kuhn-Tucker's loading-unloading consistency conditions. The same law as Chowdhury and coworkers (Chowdhury et al., 2008) is adopted for the rubber-like elastic responsible for the hardening response, combining a four-chain model (see Equation (4.74)) and an eight-chain model (see Equation (4.72)).

The hybrid model has been developed to model UHWPE (Bergström, 2002; Bergström et al., 2003) and employs the rheological model shown in Figure 4.10. The spring E is linear, following the Hencky model (Equation (4.69)), springs A and B follow the Arruda-Boyce eight-chain model (Equation (4.72)), employing the same expression except for a multiplicative constant s_B. This constant is treated in the model as an internal variable that evolves according to an equation similar to Equation (4.46). The rate of viscoplastic flow in the element P, $\dot{\gamma}^P$, is given by a power law (Equation (4.37)), as is the flow rate in the element B.
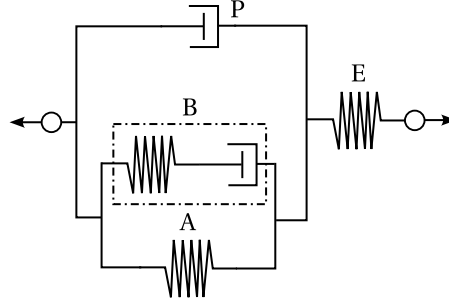
Figure 4.10: Rheological representation of the Hybrid model (Bergström, 2002; Bergström et al., 2003).

4.5   Models based on free energy

Yet another approach is to postulate a free energy that depends on the deformation gradient and the temperature, in addition to appropriate internal variables. Providing suitable rate equations for these variables, one can fully specify the constitutive description of a polymer. However, as described in the previous section, most of these models can be reinterpreted as generalizations of rheological models, employing much of the same laws already described. For some examples see Anand and Gurtin (2003); Ghorbel (2008); Anand et al. (2009); Ames et al. (2009); Pouriayevali et al. (2013).

4.6   Models considering bulk crystallinity

The following set of models considers different phases in semi-crystalline polymers, a crystalline phase, and an amorphous phase.   These adopt simple geometric considerations, which mostly only include bulk crystallinity. The simplest results of this kind are the Voigt and Reuss mixture rules (Ward and Sweeney, 2004).   It is assumed that the two phases, A and B, are laid out as layers (see Figure 4.11(a)), with the Voigt rule obtained assuming that the strain is the same in all composite layers, yielding

$$E_{\text{mix, Voigt}} = E_A \chi + E_B (1 - \chi),\tag{4.115}$$

for the modulus of the mixture, E_{mix}, with E_A and E_B denoting the modulus of each phase, and χ being the volume fraction of the phase A. This rule sets an upper limit to the stiffness of the composite material. If, on the other hand, it is assumed that the stress is the same in all composite layers (see Figure 4.11(b)), the modulus found for the mixture is

$$E_{\text{mix, Reuss}} = \frac{E_A E_B}{E_A \chi + E_B (1 - \chi)},\tag{4.116}$$

according to the so-called Reuss mixture rule. This choice corresponds to a lower bound for the stiffness of the composite material.

The work of Takayanagi and coworkers (Takayanagi et al., 1964) was the first to consider such an approach to model semi-crystalline polymers. The mixture rule employed is neither the Voigt nor the Reuss mixture rule since the phases are not arranged in layers. Instead, the amorphous phase is kept at the corner of the volume
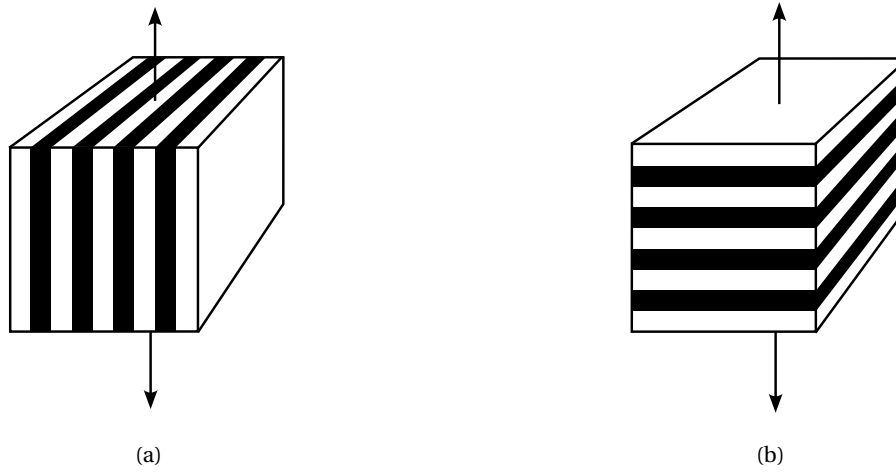
Figure 4.11: Arrangement of the two phase in a composite yielding (a) Voigt's mixture rule and (b) Reuss' mixture rule.

element, with dimensions φ and λ, as depicted in Figure 4.12. The quantity $\varphi\lambda$ is equal to the volume fraction of amorphous polymer, supplying an extra degree of freedom that can be correlated to the distribution of one phase in the other. A more homogeneous distribution of the amorphous phase leads to similar values for φ and λ, while inhomogeneities in either direction favor one or the other parameter. In Takayanagi et al. (1967), the authors employ similar techniques to model drawn samples of polyethylene (PE) and isotactic propylene (iPP), among other crystalline polymers.
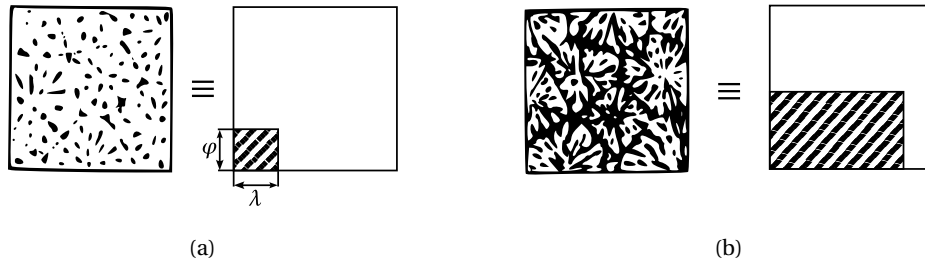
Figure 4.12: Mixture model of Takayanagi and coworkers (Takayanagi et al., 1964) for semi-crystalline polymers with crystallinities of about (a) 90% and (b) 50%, and their equivalent models. The black area denotes the non-crystalline region. Adapted from Takayanagi et al. (1964).

G'sell, Dahoun, and coworkers (G'sell and Dahoun, 1994; Dahoun et al., 1995) employ a mixture model using the Voigt composite model to combine the contributions from the amorphous (rubber-like) and the crystalline (viscoplastic) portions of the polymer. They assume a temperature above the glass transition temperature and attempt to describe HDPE and PEEK subject to uniaxial tension and pure shear. The response of the amorphous portion of the polymer is given according to the elastic rubber model in Wu and Van Der Giessen (1993). In contrast, the

behavior of the crystalline phase is modeled following Parks and Ahzi (Parks and Ahzi, 1990). It is based on a local-global interaction model established for polycrystalline metal (Molinari et al., 1987), considering the kinematically indeterminate component of the stress in a rigid-viscoplastic crystal due to the locally inextensible direction. They consider a fully crystalline HDPE and make predictions regarding the large deformation texture and the macroscopic stress-strain response.

Ahzi and coworkers (Ahzi et al., 2003) model PET at large strains, including strain-induced polymer crystallization above the glass transition temperature. The model is based on Boyce et al. (2000), considering two distinct resistances, an intermolecular (*A*) and network resistance (*B*). As in the base model, the network stress is captured by the Arruda-Boyce eight-chain model (see Equation (4.72)), and the viscous element follows the Bergström-Boyce model (see Equation (4.40)). The intermolecular resistance, however, is treated in a composite framework where the crystalline and amorphous phases are considered as two separate resistances coupled through either a Voigt or a Reuss-like mixture rule, which yield upper and lower bounds for the stiffness, respectively. The elastic elements corresponding to the crystalline and amorphous phases follow the Hencky model (see Equation (4.69)), and the viscous elements follow a model similar to the one proposed by Argon (see Equation (4.26)), where the athermal strength s_i in each phase evolves according to Equation (4.51).

Regarding applying the mixture rules to the intermolecular resistance, contributions come from the crystalline part, denoted by *c*, and the amorphous part, *a*, of the semi-crystalline polymer. These are combined according to the degree of crystallinity, χ, in two ways (see Figure 4.13):

- in parallel, such that the gradient acting in each element is equal and the Cauchy stress is supplied by

$$\boldsymbol{\sigma}_A = \chi \boldsymbol{\sigma}_A^c + (1-\chi)\boldsymbol{\sigma}_A^a; \tag{4.117}$$

- in series, such that the stress acting on both elements is the same and the plastic rate of deformation is given by

$$\boldsymbol{D}_A^p = \chi \boldsymbol{D}_A^{p,\,c} + (1-\chi)\boldsymbol{D}_A^{p,\,a}. \tag{4.118}$$

The crystallization rate is expressed following a non-isothermal phenomenological expression based on the modified Avrami equation

$$\dot{\chi} = \chi_\infty \frac{\dot{\varepsilon}_{\text{eq}}}{\dot{\varepsilon}_{\text{ref}}} m K_{\text{av}}(T)(-\ln(1-y))^{(m-1)/m}(1-y)\exp\left(\xi \frac{\text{tr}\boldsymbol{\sigma}}{G_{\text{comp}}}\right), \tag{4.119}$$

where χ_∞ is the maximum degree of crystallinity, m is the Avrami, ξ is a dimensionless model parameter, G_{comp} is the composite bulk modulus, $\dot{\varepsilon}_{\text{eq}}$ is the applied equivalent strain rate and $\dot{\varepsilon}_{\text{ref}}$ is taken as the maximum strain rate for which experimental results are available for the calibration of the model parameters. K_{av} is the transformation rate function, which is defined in the case of PET as

$$K_{\text{av}}(T) = 1.47 \times 10^{-3}\left[\frac{4\pi\text{Nu}}{3\chi_\infty}\right]^{1/3}\exp\left[-\left(\frac{T-141}{47.33}\right)\right] \quad (\text{s}^{-1},\, T \text{ in } °\text{C}), \tag{4.120}$$

with Nu the number density of nuclei initially present within the amorphous phase.
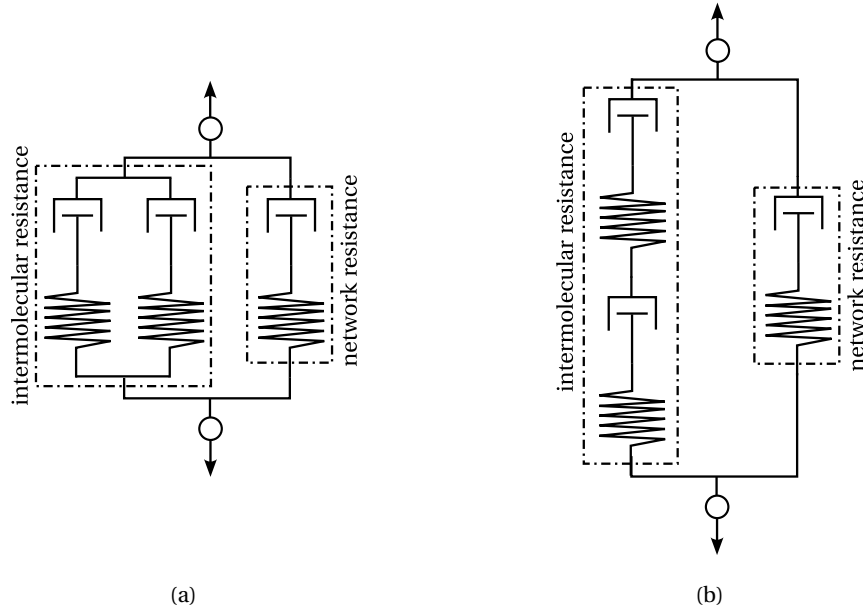
Figure 4.13: Mixture models considered by Ahzi and coworkers (Ahzi et al., 2003): (a) Parallel arrangement; (b) Series arrangement.

Strobl and coworkers (Hong et al., 2004a,b; Na et al., 2006) propose a somewhat similar description for polyethylene. They also consider two branches in a rheological model. The first is a Maxwell branch with a linear spring and an Eyring dashpot in series. The second is found through a Voigt mixture rule between rubber elastic and elastoplastic elements. Extensive experimental results on PEVA and PE support these choices.

Makradi and coworkers (Makradi et al., 2005) extend this model considering a self-consistent approach based on the Eshelby result. It amounts to the use of a Maxwell branch as the intermolecular resistance, where the properties of the elastic and viscous elements are appropriate equivalent properties. The stress corresponding to the intermolecular resistance is thus given according to the Hencky model (see Equation (4.69)), with the isotropic elastic moduli $\mathbf{D}$ following the self-consistent method proposed by Hill (Hill, 1965). The flow rule for the viscous element is given by Equation (4.64), neglecting the volumetric part. The strain rate, $\dot{\gamma}_{\mathrm{dev}}$, is defined as an average strain rate, $\dot{\bar{\gamma}}$, according to

$$\dot{\bar{\gamma}} = \frac{1}{V} \int_V \dot{\gamma} \, dV = \frac{1}{V} \sum_i V_i \dot{\gamma}_i, \tag{4.121}$$

where

$$\dot{\gamma}_i = \frac{1}{V_i} \int_{V_i} \dot{\gamma} \, dV_i, \tag{4.122}$$

with V_i denoting the volume of the ith phase and V representing the total volume. For each phase, the flow rule is also given by Equation (4.64), neglecting the volumetric part, with the strain rate in each phase following a power law (see Equation (4.37)). Thus, the average strain rate is also described by a power law, with an average strength

$\bar{s}$. It can be shown, taking into account Eshelby's results for an ellipsoidal inclusion, that

$$\frac{\dot{\gamma}_i}{\dot{\bar{\gamma}}} = \frac{5}{3} - \frac{2}{3}\frac{s_i}{\bar{s}}\left(\frac{\dot{\gamma}_i}{\dot{\bar{\gamma}}}\right)^{1/n}, \tag{4.123}$$

which, combined with Equation (4.121) and the corresponding power law, yields the average strain rate. The authors employ the same description for the evolution of the crystallinity as Ahzi et al. (2003), in addition to Flory's theory to predict the onset of crystallization as a function of the processing temperature and the extension of the polymer molecules. Later Regrain and coworkers (Regrain et al., 2009) extend the DID models to semi-crystalline models, employing a self-consistent scheme to consider the contribution of both phases.

Dusunceli and Colak (Dusunceli and Colak, 2008) extend the viscoplasticity theory based on overstress (VBO) to include crystallinity. This is achieved by describing both phases employing the VBO model and considering their contributions using a Voigt or a Reuss mixture rule. The authors validate their model using polyethylenes (UHWPE and XLPE) and PTFE.

Ayoub and coworkers (Ayoub et al., 2010, 2011) present a model very similar to Ahzi et al. (2003) and Boyce et al. (2000) to describe the mechanical behavior of HDPE. The inelastic mechanisms involve two parallel elements: a visco-hyperelastic network resistance acting in parallel with a viscoelastic–viscoplastic intermolecular resistance where the amorphous and crystalline phases are explicitly taken into consideration. The semi-crystalline polymer is considered as a two-phase composite similar to what has already been described. In the first contribution, both the crystalline and amorphous resistances are modeled employing the VBO model. Their contributions to the intermolecular resistance are incorporated through a Voigt mixture rule (see Equation (4.115)). In the second contribution, the elastic and viscous elements in crystalline and amorphous resistances are modeled employing Hencky's model (see Eqaution (4.69)) and a simplified version of Argon's model (see Equation (4.26)). They employ a modified Voigt mixture rule, where the contribution to the intermolecular resistance coming from the crystalline and amorphous phases are combined through

$$\boldsymbol{\sigma}_A = \chi^{\beta}\boldsymbol{\sigma}_c + (1-\chi)^{\beta}\boldsymbol{\sigma}_a, \tag{4.124}$$

where β is an appropriate exponent. Such an exponent is found from a fit of the Young modulus as a function of the degree of crystallinity, as shown in Figure **??**. When compared with the experimental results obtained for polyethylene samples containing degrees of crystallinity between 15 and 72%, the model can accurately capture the change in response with crystallinity before the strain hardening becomes evident. Different material parameters for each crystallinity are needed to capture the strain hardening at large strains (> 1). A similar model can be found in Abdul-Hameed et al. (2014), where the major difference is the substitution of the Maxwell branch in the network resistance for two branches, one corresponding to the amorphous contribution and the other to the crystalline contribution. They are combined as shown in Equation (4.124). This approach allows for a better fit across different degrees of crystallinity when strain hardening becomes evident and by employing the same material parameters. Very recently, Cundiff and coworkers (Cundiff et al., 2022) propose another model where the inclusion of the crystallinity is achieved through the modified Voigt mixture rule (see Equation (4.124)). Regarding the constitutive description of each phase, it employs much of the same laws found in Ahzi et al.

(2003) and Chowdhury et al. (2008). It describes strain rate crystallization through a rate equation similar to Equation (4.119).

Lastly, the two-phase model of Cangemi and Meimon for semi-crystalline polymers (Cangemi and Meimon, 2001) achieves the inclusion of the bulk crystallinity into the description of a semi-crystalline polymer in a different way. It is based on the continuum mixture theory such that according to the microstructure of semi-crystalline polymers, the free amorphous phase is assumed comparable to a fluid which saturates the complementary space to that of the solid structure, the crystalline phase plus the rigid amorphous phase.

4.7   Micromechanical models

In addition to bulk crystallinity, the final set of models includes some geometric considerations at the micro-scale. Accordingly, micromechanical modeling based on the laminar composite approach was proposed by Lee and coworkers (Lee, 1993; Lee et al., 1993). Using an eight-chain model, this model added a rigid-viscoplastic amorphous phase (see Equation (4.72)), and Sachs/Taylor hybrid interaction law was used to relate the mechanical properties of microscopic two-phase inclusion. In these models, a crystalline polymer is regarded as a polycrystalline aggregate of randomly distributed crystallites that plastically deform cooperatively. It does not consider the mesoscopic structure of the polymer.

According to Uchida and coworkers (Uchida and Tada, 2013), these models were then improved to more realistic elasto-viscoplastic models by Nikolov and coworkers (Nikolov and Doghri, 2000; Nikolov et al., 2002) and van Dommelene and coworkers (van Dommelen et al., 2003) Similarly, Guan and coworkers (Guan and Pitchumani, 2004) present a micromechanical analysis of the elastic properties of semi-crystalline thermoplastic materials.

Bedoui and coworkers (Bedoui et al., 2006) consider a micromechanical model applied to infinitesimal strains, concluding that the spherulitic mesostructure does not affect the response of the material at that level of strain. The phase of the amorphous part of the semi-crystalline polymers has a noticeable impact on the stiffness of the polymer. There is moderate agreement between the predictions and the experimental results.

Alternatively, Uchida and coworkers (Uchida and Tada, 2013) developed a large deformation finite element homogenization model of spherulitic HDPE. This contrasts with the previously described models because the interaction laws applied in these models have no geometric information, and equilibrium in the spherulite cannot be considered. Since Uchida and coworkers' model directly solves both the microscopic and mesoscopic displacement fields using an FE-based homogenization scheme, compatibility and equilibrium between adjacent microstructure in the spherulite are automatically satisfied. According to the authors, the former micromechanical-based model is suitable when the macroscopic response and texture evolution are required. Meanwhile, the homogenization-based model appropriate when strain and stress distributions in the spherulite are required. Regarding the size of the representative domain, Teixeira-Pinto and coworkers (Teixeira-Pinto et al., 2016) claim that it significantly exceeds the size of a single spherulite.

Page intentionally left blank.

tension

Chapter 5

Numerical results

This chapter presents two sets of results concerning the subject of thermomechanical modeling of semi-crystalline polymers. The first one is adapted from Vila-Chã et al. (2023) and pertains to the implicit partitioned solution of a thermomechanical problem involving the elastoplastic constitutive description of the material. The second pertains to the implementation and validation of state of the art constitutive models for semi-crystalline polymers.

5.1   Necking of a thermoelastoplastic circular bar

The thermomemechanical problem under analysis consists of the thermally triggered necking of a circular bar, as initially reported in Simo and Miehe (1992b) and replicated in Danowski (2014). The problem consists of a cylindrical bar of radius $r = 6.413$ mm and length $h = 53.334$ mm, subject to a prescribed axial displacement $\bar{u}_y = 8$ mm at both ends during $t_s = 8$ s. The supports at the tips allow the contraction of the specimen. The bar is initially at room temperature, $T_0 = T_\infty = 293$ K, and is subject to heat transfer by convection at all boundaries, with a heat transfer coefficient $h_c = 17.5 \times 10^{-3}$ Nmm^{-1}s^{-1}K^{-1}. The material is modeled by the constitutive model proposed by Simo and Miehe (Simo and Miehe, 1992b), and the material properties are given in Table 5.1.

The problem is analyzed using two-dimensional axisymmetric QUAD4-FBAR elements (de Souza Neto et al., 1996) for the mechanical problem and QUAD4 elements for the thermal problem. Figure 5.1 illustrates the problem setup, the finite element mesh employed in the 2D simulations, and distinct stages of deformation and temperature field during the prescribed elongation, evidencing the significant necking of the bar. Only one-quarter of the specimen is simulated, resulting in a finite element mesh with 1326 nodes and 1250 elements. Unless otherwise stated, this mesh is employed in the following analyses. The load is applied in a total of 80 equal magnitude increments and considering a constant incremental time step of $\Delta t = 0.1$ s. A quasi-static solution is computed for the mechanical problem using a backward Euler integration. The transient temperature field is integrated with the generalised-α method with $\rho_{\infty, T} = 1.0$.

Table 5.1: Material properties and initial and boundary conditions for the problem concerning the necking of a thermoplastic circular bar.

Material Properties			Effective value
Density	ρ	$(\text{Ns}^2\text{mm}^{-4})$	7.8×10^{-9}
Bulk modulus	κ	(Nmm^{-2})	164.206×10^3
Shear modulus	μ	(Nmm^{-2})	801.938×10^3
Conductivity	k	$(\text{Ns}^{-1}\text{K}^{-1})$	45
Heat capacity	$C_{\mathbf{F}}$	$(\text{mm}^2\text{s}^{-2}\text{K}^{-1})$	460×10^6
Coefficient of thermal expansion	α_T	(K^{-1})	10×10^{-6}
Dissipation factor	χ_{d}	(-)	900×10^{-3}
Initial yield stress at T_0	$\sigma_{y,0}$	(Nmm^{-2})	450
Linear hardening coefficient at T_0	H	(Nmm^{-2})	129.24
Saturation exponent	δ	(-)	16.93
Saturation yield stress at T_0	$\sigma_{y,\infty}$	(Nmm^{-2})	715
Thermal softening parameter ($\sigma_{y,0}$)	w_0	(K^{-1})	2×10^{-3}
Thermal softening parameter ($\sigma_{u,\infty}, H$)	w_h	(K^{-1})	2×10^{-3}
Boundary Conditions			
Radius of the cylindrical bar	r	(mm)	6.413
Length of the cylindrical bar	h	(mm)	53.334
Maximum displacement at both ends	$\bar{u}_y$	(mm)	8
Time to maximum displacement	t	(s)	8
Heat transfer coefficient	h_c	$(\text{Nmm}^{-1}\text{K}^{-1})$	17.5×10^{-3}
Initial Conditions			
Initial temperature	T_0	(K)	293
Reference value			
Temperature at outer radius (r)		(K)	
Longitudinal reaction forces		(N)	

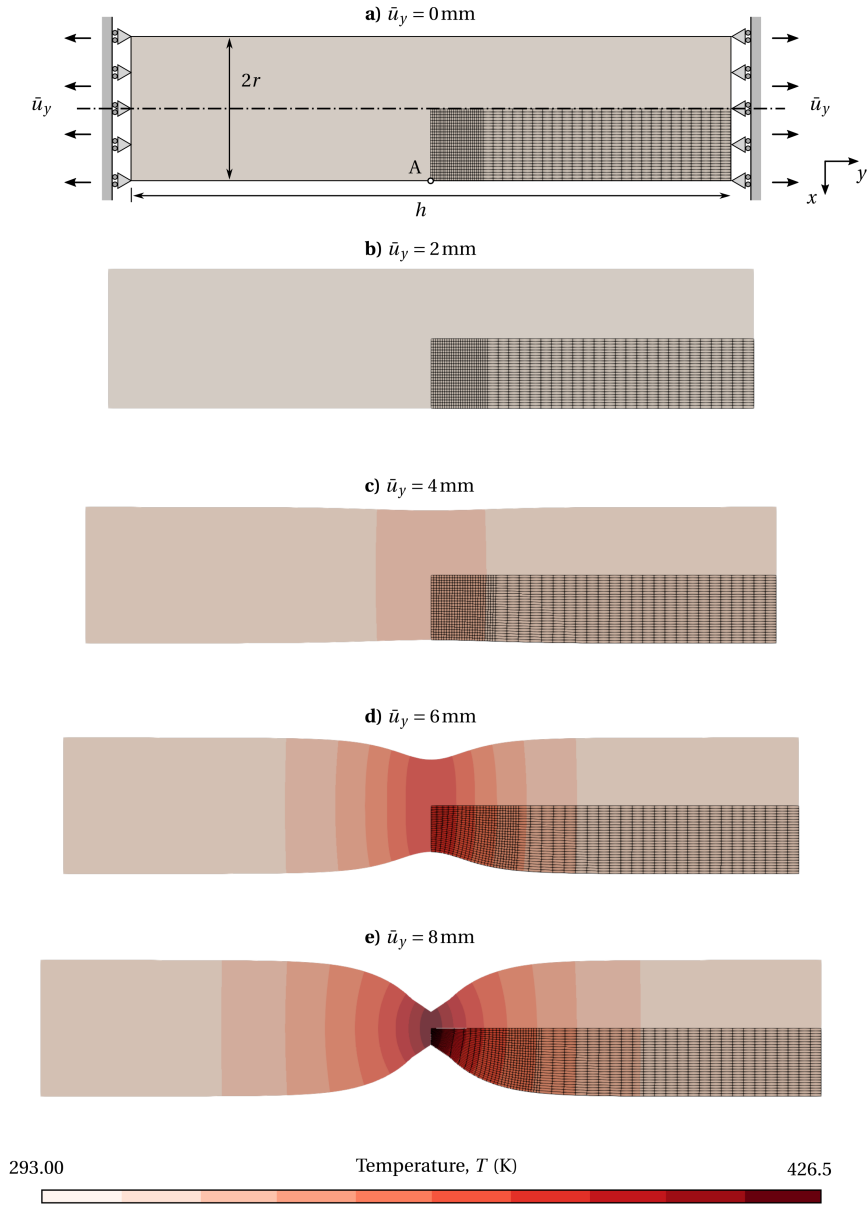Figure 5.1: Deformation of the thermally triggered necking of a thermoplastic circular bar and temperature field stages during the loading and axisymmetric finite element mesh. The results are obtained with QUAD4-FBAR elements for the mechanical problem and QUAD4 elements for the thermal problem, non-adiabatic boundary conditions, the inconsistent mechanical dissipation formulation, and the Fourier law based on constant k_0.

Validation of the numerical results

The reaction force at the supports and the neck surface temperature at point A are compared to results found in the literature to validate the computationally implemented solution procedure, as shown in Figure 5.1. The analysis's reference data may be found in Simo and Miehe (1992b). It should be noted that key distinctions between the current work and the reference lead to slightly different outcomes. Regarding the heat conduction law employed in each contribution, although the large deformation version of the Fourier law is adopted in both works, Simo and Miehe (Simo and Miehe, 1992b) considered the spatial thermal conductivity, k, as a fixed material parameter. In the present work, the material thermal conductivity, k_0, is interpreted as the fixed material parameter. In addition, Simo and Miehe (Simo and Miehe, 1992b) solved the coupled problem using an explicit scheme, while in the present work, an implicit scheme is considered. Lastly, regarding spatial discretisation, Simo and Miehe (Simo and Miehe, 1992b) employed mixed displacement-pressure QUAD8 elements.

The evolution of the reaction force and the neck surface temperature as a function of the prescribed displacement are shown in Figure 5.2. From a physical point of view,
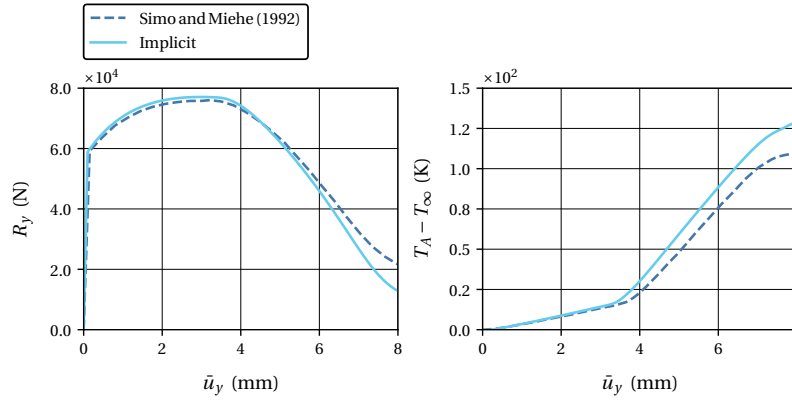

Figure 5.2: Evolution of the reaction force at the tips of the bar and the neck surface temperature with the prescribed displacement using QUAD4-FBAR elements for the mechanical problem and QUAD4 elements for the thermal problem.

the reaction forces show that the simulation occurs almost entirely in the elastoplastic regime. As previously mentioned, necking is automatically triggered, resulting in a significant reduction of the reaction force starting at approximately $\bar{u}_y = 4\,\text{mm}$, followed by a steep temperature rise due to the higher plastic dissipation around the necking region.

Inspecting Figure 5.2 from a validation perspective, the numerical results show a reasonable agreement with the literature. Regarding the reaction force at the supports, there is a good agreement for most of the displacement range examined, except for the largest values, where some discrepancy is observed. There are larger disparities in the neck surface temperature at point A, with noticeable differences for displacements larger than $\bar{u}_y \approx 3.5\,\text{mm}$. It is reasonable to assume that these may well stem from the aforementioned differences between the present work and Simo and Miehe (1992b).

Comparison of implicit solution methods

In this section, appropriate implicit methods for solving thermomechanical problems with thermoplastic constitutive behavior are compared. These are the fixed-point method, the Aitken relaxation method, two Broyden-like methods, both Type I, with $\beta = -1$ and $s = 1$ (coinciding with Broyden's method) or $s = 2$, a Newton–GMRES method, and MPE method in cycling mode with $p = 1$ and $q = 3$. The maximum displacement at both ends is restricted to 5 mm, applied in 5 s and 100 increments ($\Delta t = 0.05$ s) to prevent an excessive elongation of the elements in the finite element simulation. The coupling strength is correlated with the value of thermal softening parameters w_0 and w_h, set to be equal. Its effect on the implicit solution of the problem is an increased number of nonlinear iterations to solve the problem, as is illustrated in Figure 5.3. It depicts the number of nonlinear iterations needed to solve the coupled problem at each time step and the corresponding total number of residual evaluations as a function of the thermal expansion coefficient for the fixed-point method in the solution of the necking of a circular bar with $w_0 = w_h \in \{2 \times 10^{-3}, 4.89 \times 10^{-3}, 10^{-2}\}\,\mathrm{K}^{-1}$. A higher total number of nonlinear iterations per time step is necessary to solve the problem as w_0 and w_h increase, corresponding to a taller and broader peak in the number of iterations needed to solve the problem per time step. The coupling strength is the most intense when the necking begins, which occurs at different moments as w_0 and w_h vary. This peak is the main contributor to the difference in the total number of iterations taken to solve each problem with different softening parameters. Once again, the improvement in the efficiency achieved by the implicit methods under analysis is obtained by decreasing the number of nonlinear iterations needed to solve the problem when the coupling is the most challenging, as can be concluded from Figure 5.4. It shows the number of nonlinear iterations needed to solve the coupled problem at each time step and the total number of residual evaluations as a function of the thermal expansion coefficient for several implicit methods in the solution of the necking of a circular bar with $w_0 = w_h = 10^{-2}\,\mathrm{K}^{-1}$. On the other hand, when the coupling is not as demanding, the difference between the different methods is hardly noticeable.

It is pointed out that what is depticted in Figures 5.3 and 5.4 is the number of nonlinear iterations and not the number of residual evaluation per time step. Thus, for comparisons concerning the computational efficiency of the different methods under analysis, the information shown in Figure 5.5 is more appropriate, as it displays the total CPU time in seconds and the total number of residual evaluations as a function of the thermal softening parameters. The best performing methods are the Broyden-like methods, whose performance is very similar. They are followed by the Aitken relaxation and the MPE in cycling mode, also displaying a comparable efficiency. The Newton-GMRES method is the worse performing method considered, being around 20% slower than the Broyden-like methods and roughly on par with the fixed-point method. Moreover, it fails to converge for $w_0 = w_h = 2 \times 10^{-3}\,\mathrm{K}^{-1}$. Table 5.2 summarizes all the results previously discussed regarding the computational time each implicit method takes and the number of residual evaluations.

Figure 5.3: Number of nonlinear iterations needed to solve the coupled problem at each time step (continuous) and the total number of residual evaluations (dashed) as a function of the thermal expansion coefficient for the fixed-point method in the solution of the necking of a circular bar with $w_0 = w_h \in \{2 \times 10^{-3}, 4.89 \times 10^{-3}, 10^{-2}\}\mathrm{K}^{-1}$.
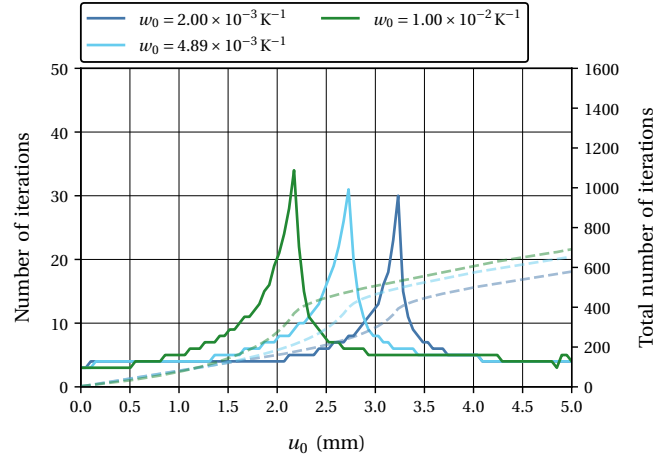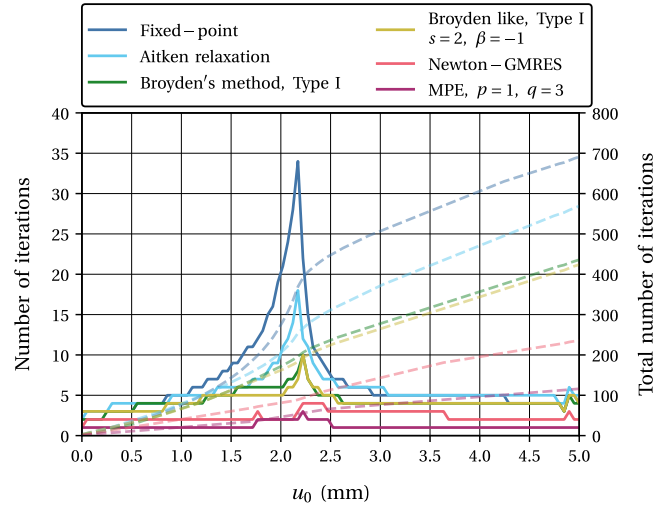

Figure 5.4: Number of nonlinear iterations needed to solve the coupled problem at each time step (continuous) and the total number of residual evaluations (dashed) as a function of the thermal expansion coefficient for several implicit methods in the solution of the necking of a circular bar with $w_0 = w_h = 10^{-2}\,\mathrm{K}^{-1}$.
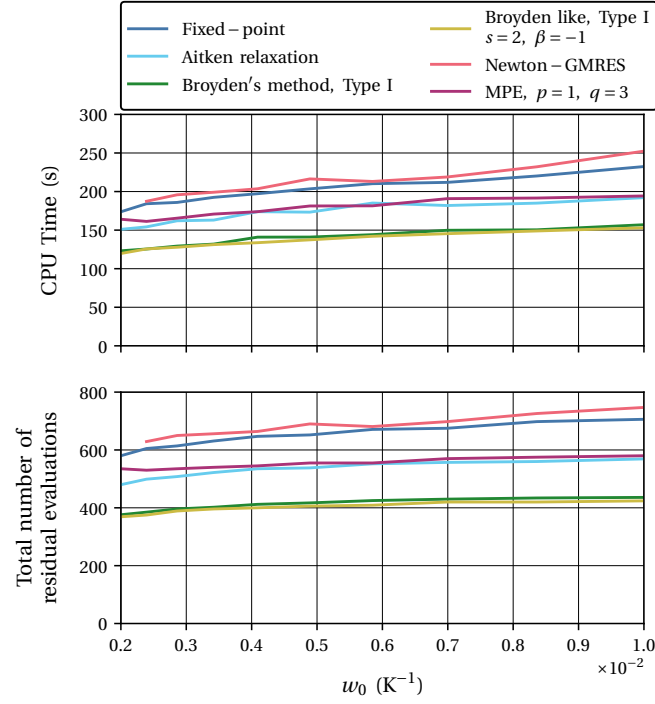
Figure 5.5: Total CPU time in seconds and the total number of residual evaluations as a function of the thermal softening parameters $w_0 = w_h$ in the solution of the necking of a thermoplastic circular bar with $w_0 = w_h = 2 \times 10^{-3}\,\mathrm{K}^{-1}$ to $10^{-2}\,\mathrm{K}^{-1}$.

Table 5.2: Total CPU time in seconds and the total number of residual evaluations as a function of the thermal softening parameters $w_0 = w_h$ in the solution of the necking of a thermoplastic circular bar with $w_0 = w_h \in \{2 \times 10^{-3},\ 4.89 \times 10^{-3},\ 10^{-2}\}\mathrm{K}^{-1}$. The best performances are highlighted in gray.

w_0 $(10^{-3}\,\mathrm{K}^{-1})$	CPU Time (s)			Nr Residual Evaluations		
	2	4.89	10	2	4.89	10
FXPT	1.74×10^2	2.04×10^2	2.32×10^2	580	652	706
AITK	1.51×10^2	1.73×10^2	1.92×10^2	480	538	569
BRDI	1.23×10^2	1.41×10^2	1.57×10^2	376	417	436
BRDI2	1.20×10^2	1.37×10^2	1.53×10^2	369	406	424
NEWT	NC	2.16×10^2	2.52×10^2	NC	690	747
MPE	1.64×10^2	1.81×10^2	1.94×10^2	535	555	580

5.2   State of the art in semi-crystalline polymer modeling

This section analyses two state-of-the-art constitutive models for semi-crystalline polymers. The first model is described in Hao et al. (2022a), and is applicable to polymer plastics in general, without explicitly considering the polymer's bulk crystallinity. Alternatively, the second model can be found in Abdul-Hameed et al. (2014), and considers the crystallinity of the polymer explicitly, attempting to describe the polymer at different crystallinities with only one set of material parameters. A more recent model proposed by Cundiff and coworkers (Cundiff et al., 2022) shares some of the same ideas regarding the inclusion of bulk crystallinity into the constitutive description of semi-crystalline polymers, allowing even strain-induced crystallinity. Despite being more recent, it is not explored here for two reasons: the effect of crystallinity is not extended to the network resistance responsible for strain hardening, and the authors do not validate the model at different degrees of crystallinity. The work in Abdul-Hameed et al. (2014) includes these aspects in its formulation. The main features of each model are described throughout Chatper 4.

Computational framework   The solution of the thermomechanical problem is achieved by employing an approach described thoroughly in Bergström (2015) and Alves (2022), whose Python implementation is available in-house. It is restricted to displacement-driven uniaxial loading, tension, or compression, and it achieves the solution of the mechanical problem through a minimization procedure. In each time step, the axial stretch is prescribed, and the transversal stretches are obtained as those leading to a minimum in the transversal stresses. This minimum should be zero as the boundary condition on the lateral surfaces corresponds to a free surface. Accordingly, it is implicitly assumed that the response is homogeneous, which allows for comparisons solely with experimental results where the intrinsic response of the material is shown.

Inclusion of the thermal field   Regarding the thermal field, its inclusion is restricted to the isothermic and adiabatic cases. The former coincides with a strain rate sufficiently slow so that the heat generated from the deformation is easily offloaded to the environment, keeping the temperature constant. The latter corresponds to a strain rate so high that no energy is exchanged with the environment during loading, approaching an adiabatic condition. Arruda and coworkers (Arruda et al., 1995) employ the dimensionless number defined as $\tau_{\text{therm}} = t_{\text{test}}/t_d$ to probe how appropriate either of these assumptions is. t_{test} is defined as the test time to reach the true strain of -1.0 (in compression), and t_d is the thermal diffusion time of the specimen, which may be approximated as

$$t_d \approx \frac{L^2}{2(k/\rho C_{\mathbf{F}})}, \tag{5.1}$$

where L is a characteristic dimension of the specimen from the center of the deforming region to the nearest heat sink. If $\tau_{\text{therm}} \ll 1$, it is safe to assume an adiabatic evolution, while if $\tau_{\text{therm}} \gg 1$, the experiment progresses isothermically. $\tau_{\text{therm}} \approx 1$ points to a coupled problem, in the sense that some heat is removed from the specimen as the experiment progresses, although not preventing an increase in temperature.

In the present work, an adiabatic evolution is achieved through the inclusion of temperature as an internal variable of the model, whose rate equation is the heat

conduction equation (see Equation (2.14)), discarding the heat conduction term, and setting the internal dissipation according to the adopted constitutive model. On the other hand, to ensure an isothermal evolution, the temperature is treated as a model parameter and remains constant throughout the simulation.

5.2.1 Model: Hao and coworkers (2022a)

Following the description in Hao et al. (2022a), the experimental results employed for validation are those of Khan and Farrokh (Khan and Farrokh, 2006) obtained during the uniaxial compression of nylon 101 at a constant strain rate. Nylon 101 is a standard all-purpose extruded grade of nylon type 66 (polyamide). Also, among all of the unmodified nylons, it is the strongest and hardest nylon and has one of the highest melting temperatures (260 °C) (Khan and Farrokh, 2006). The material is modeled by the constitutive model proposed by Hao and coworkers (Hao et al., 2022a), and the material properties are given in Table 5.3. They are taken from Hao et al. (2022a), with the exception of the parameter m whose value is taken as 0.66, following Hao et al. (2022b) [1].

The following strain rates are considered: $10^{-5}\,\text{s}^{-1}$, $10^{-2}\,\text{s}^{-1}$, and $1\,\text{s}^{-1}$. According to the dimensionless parameter τ_{therm} (Hao et al., 2022a), the first corresponds to an adiabatic process and the last to an isothermic process. A strain rate of $10^{-2}\,\text{s}^{-1}$ coincides, however, with a coupled evolution that is neither adiabatic nor isothermic. Despite this, due to the constraints on the computational tool available, it is simulated here using an adiabatic condition. The predicted stress-strain and temperature-strain curves obtained are compared in Figure 5.6 to the experimental results in Khan and Farrokh (2006) and the numerical results obtained by Hao and coworkers (Hao et al., 2022a).

In Hao et al. (2022a), the authors mention that the activation plastic strain may vary with both the temperature and the strain rate, in addition to other variables. They do not, however, establish a specific relation between this parameter and the strain rate for nylon 101. The value corresponding to $\varepsilon = 10^{-5}\,\text{s}^{-1}$ is given in Table 5.3 and found in Hao et al. (2022a), while the values employed for the other two strain rates are taken from Hao et al. (2022b) where the same experimental data is considered. These are $\dot{\gamma}^{p,2} = 0.0577$ at $\dot{\varepsilon} = 10^{-2}\,\text{s}^{-1}$ and $\dot{\gamma}^{p,2} = 0.0705$ at $\dot{\varepsilon} = 1\,\text{s}^{-1}$.

Discussing first the fitness of the model proposed in Hao et al. (2022a) to describe the experimental results of Khan and Farrokh (Khan and Farrokh, 2006), the model captures adequately the elastic range and the first yield point. This is due to the extended formulation of the rate equation presented by the authors (see Equation (4.54)) which considers four different athermal strengths related to the yield of the different phases in the polymer. As seen from the experimental results, nylon 101 displays double yield, which becomes more noticeable as the strain rate increases. Accordingly, in Figure 5.6 where the true stress-strain curves are depicted, only the strain rates of $10^{-2}\,\text{s}^{-1}$ and $1\,\text{s}^{-1}$ show a prominent double yield. This phenomenon is also correctly described by the model, with a slight underestimation of the stress response for the higher strain rates. This is achieved through the dependence of the athermal strength on the temperature through the elastic modulus, similar to what is shown in Equation (4.27). Conversely, regarding the second yield stress, the model slightly overestimates the stress. In fact, the experimental value found for the second

---

[1] As the supplied value in the first contribution, 0.8, did not produce the expected results.

Table 5.3: Material properties and initial conditions for the uniaxial compression of nylon 101.

| Material Properties			Effective value
Density	ρ	$(\mathrm{Ns^2mm^{-4}})$	1.150×10^{-9}
Young modulus at T_{ref}	$E_{a,\mathrm{ref}}$	$(\mathrm{Nmm^{-2}})$	3.01×10^3
Reference temperature	T_{ref}	(K)	295
Temperature dependence coefficient	β	(-)	3.7×10^{-3}
Poisson's coefficient	ν_I	(-)	390×10^{-3}
Heat capacity	$C_{\mathbf{F}}$	$(\mathrm{mm^2 s^{-2} K^{-1}})$	1.500×10^6
Athermal peak strength	s_1	(MPa)	140
First saturation strength	s_2	(MPa)	138
Second saturation strength	s_3	(MPa)	183
Pre-peak hardening	h_1	(MPa)	6.27×10^3
Post-peak softening	h_2	(MPa)	5.03×10^3
Second yield hardening	h_3	(MPa)	740
Peak plastic strain	$\gamma^{p,1}$	(-)	27.0×10^{-3}
Activation plastic strain ($\dot{\varepsilon} = 10^{-5}\,\mathrm{s^{-1}}$)	$\gamma^{p,2}$	(-)	29.8×10^{-3}
Smooth factor	f	(-)	0.3
Pressure sensitivity	α	(-)	0
Rate sensitivity	m	(-)	660×10^{-3}
Pre-exponential strain rate	$\dot{\gamma}_0$	$(\mathrm{s^{-1}})$	329
Rate sensitivity	A	$(\mathrm{KMPa^{-1}})$	115
Rubbery modulus	C_r	(MPa)	-
Number of rigid links	N	(-)	-
Initial Conditions			
Initial temperature	T_0	(K)	295
Initial equivalent strength	s_0	(MPa)	120
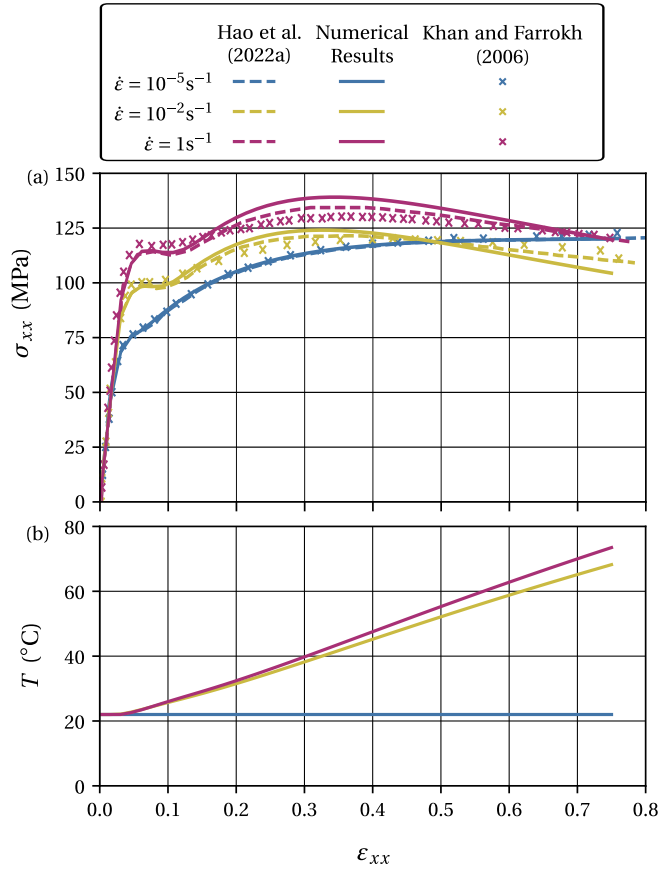
Figure 5.6: Comparison between the experimental results of Khan and Farrokh (2006), the numerical results of Hao et al. (2022a), and the present work for a uniaxial compressive test at strain rates of $10^{-5}\,\mathrm{s}^{-1}$, $10^{-2}\,\mathrm{s}^{-1}$, and $1\,\mathrm{s}^{-1}$: (a) True strain-true stress curve; (b) True strain-temperature curve.

yield stress is 129.8 MPa, with the model predicting a value of 134.5 MPa, amounting to a relative error of 3.6%.

When the numerical results obtained in this work are compared to those in Hao et al. (2022a), there is a perfect agreement for the lowest strain rate (10^{-5} s^{-1}). That said, there are some differences between the responses corresponding to the other two strain rates. Nevertheless, until the first yield and subsequent softening, there is good agreement between the two sets of numerical results. As the strain increases, the difference between the two grows larger. This is due to a number of factors. The first concerns mainly the experiment corresponding to a strain rate of 10^{-2} s^{-1}, which in the present work is simulated as an adiabatic process. This is not strictly true and contributes to differences relative to the reference results, which were obtained employing a fully thermomechanical description of the problem, including conduction inside the cylinder and convection at its borders. A further contributing factor that also affects the response at 1 s^{-1} is the heterogeneity of the response in Hao et al. (2022a). Despite the homogeneous temperature distribution, the plastic deformation is heterogeneous, breaking the assumptions of the numerical tool employed in this work and further motivating differences in the results. Finally, concerning the temperature evolution with the strain in the adiabatic cases, it remains constant during the elastic portion of the stress-strain response, and begins to increase after this. The final value obtained for the 1 s^{-1} strain rate is 73.4 °C, which is close to the value obtained in Hao et al. (2022a) equal to 71.5 °C, corresponding to a relative error equal to 2.7%. However, the same authors find a heterogeneous temperature distribution for the 10^{-2} s^{-1} case, rendering a comparison impossible.

In general, the implementation developed in this work compares favorably with the one found in Hao et al. (2022a).

5.2.2   Model: Abdul-Hameed and coworkers (2014)

Following the description in Abdul-Hameed et al. (2014), the experimental results employed for validation are those of Ayoub and coworkers (Ayoub et al., 2011) obtained during the uniaxial tension of polyethylene with different degrees of crystallinity at a constant strain rate. The material is modeled by the constitutive model proposed by Abdul-Hameed and coworkers (Abdul-Hameed et al., 2014), and the material properties are given in Tables 5.4 and 5.5.

The strain rates considered are 10^{-4} s^{-1}, 5×10^{-4} s^{-1}, 10^{-3} s^{-1}, 5×10^{-3} s^{-1}, and 10^{-2} s^{-1}, and are all assumed to correspond to an isothermic evolution. The stress-strain curves obtained for polyethylenes with crystallinities equal to 15, 30, and 72.4% are compared in Figure 5.7 to the experimental results in Ayoub et al. (2011) and the numerical results obtained by Abdul-Hameed and coworkers (Abdul-Hameed et al., 2014).

To begin, Abdul-Hameed and coworkers's model (Abdul-Hameed et al., 2014) must be assessed for its ability to describe the experimental data in Ayoub et al. (2011). It can capture accurately the yield stress for all the crystallinities considered. However, it does not capture the smooth transient between the elastic range and the "steady state" plastic flow. This is the outcome of the thermally activated flow rule (see Equation (4.20)) employed for both the crystalline and amorphous contributions to the intermolecular resistance, where an appropriate internal variable, such as the athermal strength (and corresponding rate equation) is not included. Regarding the hardening it is not captured so well, specially in the case of LDPE. This is less so for

the ULDPE, and it is only true for at large strains ($\varepsilon_{xx} > 1$) for HDPE. Thus, the attempt of this model to describe the behavior of polyethylene at different crystallinities using just one set of material parameters is only moderately successful.

Moving to the comparison between the numerical results obtained in this work and in Abdul-Hameed et al. (2014). Despite the limitations of the numerical tool available, a good agreement is expected. That said, employing the parameters supplied in the contribution just mentioned, the results obtained are not those expected. A better agreement is found taking the shear modulus C_c multiplied by 2/3. Still, some minor discrepancies in the hardening behavior simulated can be found in the results concerning the HDPE and the LDPE. These are somewhat exacerbated, especially for the larger strain rates considered in the case of ULDPE. On the other hand, there is full accord in the elastic response and subsequent yielding between the two sets of numerical results for all crystallinities considered. This points to some differences in the network branch of the model, to which the parameters already mentioned contribute. That said, there is an acceptable agreement between the numerical results obtained in the present work and in Abdul-Hameed et al. (2014).

Table 5.4: Material properties for the uniaxial tension of polyethylene.

Material Properties			Effective value
Temperature	T	(K)	293
Amorphous phase			
Young modulus	E_a	(Nmm^{-2})	4.7
Poisson's coefficient	ν_a	(-)	499×10^{-3}
Pre-exponential strain rate	$\dot{\gamma}_{0,a}$	(s^{-1})	1.75×10^6
Activation energy	ΔG_a	(s^{-1})	263×10^{-24}
Shear resistance	s_a	(MPa)	6.88
Rubbery modulus	C_r	(MPa)	1.7
Limiting chain extensibility	N_r^2	(-)	202
Temperature relaxation parameter	C	(MPa^{-1}s^{-1})	129.96×10^{-9}
Crystalline phase			
Young modulus	E_c	(Nmm^{-2})	4.490×10^3
Poisson's coefficient	ν_c	(-)	345×10^{-3}
Pre-exponential strain rate	$\dot{\gamma}_{0,c}$	(s^{-1})	1.75×10^6
Activation energy	ΔG_c	(s^{-1})	129×10^{-24}
Shear resistance	s_c	(MPa)	190.73
Shear modulus	C_c	(MPa)	239.13
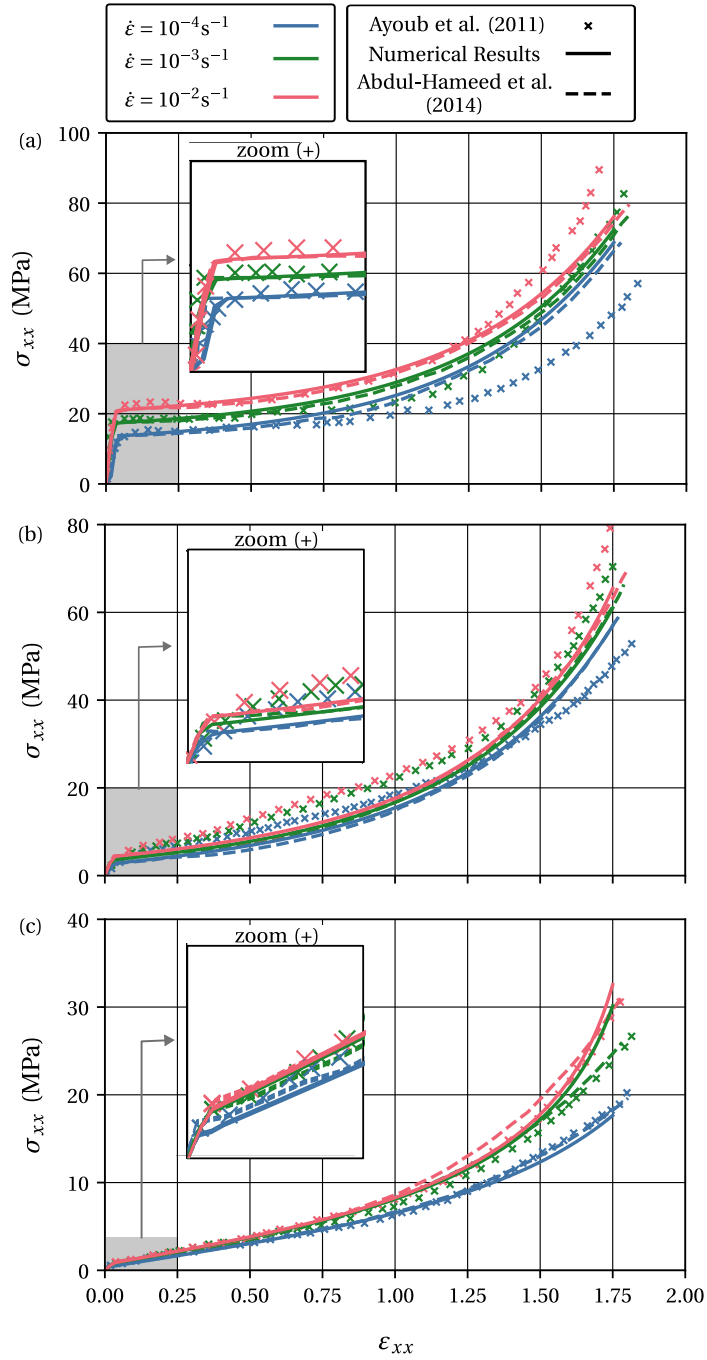
Figure 5.7: True stress-true strain curves obtained corresponding to the experimental results of Ayoub et al. (2011), the numerical results of Abdul-Hameed et al. (2014) and the present work for a uniaxial tensile test at strain rates of $10^{-4}\,\mathrm{s}^{-1}$, $5 \times 10^{-4}\,\mathrm{s}^{-1}$, $10^{-3}\,\mathrm{s}^{-1}$, $5 \times 10^{-3}\,\mathrm{s}^{-1}$, and $10^{-2}\,\mathrm{s}^{-1}$. (a) HDPE ($\chi = 72.4\%$); (b) LDPE ($\chi = 30\%$); (c) ULDPE ($\chi = 15\%$).

Table 5.5: Mechanical interaction parameters.

Parameter	HDPE	LDPE	ULDPE
χ	0.724	0.3	0.15
β_I	5.8	2.9	2.8
β_N	14.1	3.9	3.7

Chapter 6

Conclusion and Future Works

This work has two goals: first, it focuses on computational techniques for numerical simulation of thermomechanical problems and, more broadly, multi-physics problems; second, it attempts to provide an overview of the state-of-the-art in semi-crystalline polymer constitutive modeling. They are both critical to the creation of a robust computational toolbox for the design and optimization of semi-crystaline polymer based materials as well as the simulation of their thermomechanical behavior under mechanical and thermal loadings.

The first task requires both a thermodynamically consistent description of continuum thermodynamics and a precise formulation of the thermomechanical problem. A thorough investigation of the available approaches to solving coupled problems is provided, with a particular focus on thermomechanical problems. The strongly coupled or implicit partitioned schemes are chosen as the most promising approach because they can take advantage of existing software, provide accurate results that agree with a monolithic approach, are not memory intensive, are easy to implement, and are competitive in terms of computational efficiency through the use of convergence acceleration techniques. Recasting the problem as a system of nonlinear equations, where the residual is the difference between the initial input and its output after applying the fixed-point corresponding to the isothermal split, allows the straightforward use of a wide selection of methods for the solution of systems of nonlinear equations. This approach is applied specifically to the thermomechanical problem here, but it applies to other multi-physics phenomena with little modification. These are the fixed-point method, the underrelaxation method, the Aitken relaxation, the Broyden-like family of methods, the Newton-Krylov methods, and the polynomial vector extrapolation methods MPE and RRE in cycling mode.

The validation of the thermomechanical solver and the implicit solution methods, as well as their comparison, is performed by considering an example taken from the literature: the necking of a circular thermoelastoplastic bar. The numerical results agree with the references, hence supporting the developed solution scheme. Regarding the comparison of the different implicit techniques, the best performing are the Broyden-like methods with $\beta = -1$, Type I update, and $s = 1$, corresponding to the good Broyden method, and $s = 2$. These are both computationally efficient (few calls to the residual function) and memory efficient. The Aitken relaxation, the simplest and least memory-intensive, also performs well. The other methods considered, including the Newton-GMRES and the MPE in cycling mode, display worse performance. Moreover, it has been determined that the most computationally

demanding portion of the implicit partitioned schemes is the solution of the mechanical and thermal problems, with the manipulation concerning solely the coupling solver taking a very small part of the total computational time.

The second topic addressed in this work is the constitutive description of semi-crystalline polymers. To accomplish this, a detailed account of the thermomechanical behavior of semi-crystalline polymers is provided so that the appropriate modeling goals can be established. It is primarily based on this class of materials' response to various mechanical experiments, ranging from constant strain rate experiments to stress relaxation, creep, and dynamical mechanical analysis. Semi-crystalline polymers, in constant strain rate experiments, typically exhibit a response that consists of a linear stress-strain relationship followed by yield. A steady state is sometimes observed, followed by intense strain hardening at large strains. Regarding the influence of temperature on the behavior of this class of polymers, its increase leads to lower stiffness and yield strength. However, unlike glassy polymers, they retain usable structural properties even after the glass transition temperature is crossed. Common semi-crystalline polymers employed in commodity uses are HDPE and PP, while PA, PET, PPA, and PEEK satisfy the requirements of increasingly demanding engineering applications. The strain rate and the pressure exert the opposite effect on the stiffness and strength of semi-crystalline polymers. Furthermore, the yield phenomenon in semi-crystalline polymers is neither rate-independent nor linear with the strain rate, requiring appropriate nonlinear modeling.

Concerning the influence of bulk crystallinity and lamellar thickness, an increase in the former implies a nonlinear increase in stiffness and strength, whereas an increase in the latter results in a linear increase in strength for moderate thicknesses, but stagnates for thicker lamella. Semi-crystalline polymers also have a double yield, which means that, as the strain increases, there are two distinct yield stresses. This phenomenon is also linked to the temperature softening phenomenon, in which higher strain rates result in significant heat production and temperature increases, causing the material to soften. Furthermore, cold drawing is common, as when a neck develops in a tensile uniaxial test, where the specimen thins in that region until the natural draw ratio is achieved. After that, the material in the neck has hardened sufficiently so that the thinned region travels across the specimen rather than decreasing until failure. Semi-crystalline strain hardening behavior is also similar to rubber elasticity.

In terms of the semi-crystalline polymer response to dynamical mechanical analysis, polymers with high crystallinity do not show a significant drop in storage modulus as frequency decreases in isothermal results. When the degree of crystallinity is low, a clear viscoelastic transition from glassy to leathery is observed. In isochronal results, one can observe the various relaxations present in semi-crystalline polymers. Relaxation I is visible at all crystallinity levels at lower temperatures, while relaxation II and III are more easily detectable at lower and higher crystallinities, respectively.

Finally, the thermal properties of semi-crystalline polymers are similar to those of other polymers in that they have a relatively large linear expansion coefficient and low thermal conductivity and diffusivity. This raises concerns about heat distortion when using semi-crystalline polymers in engineering applications and difficulties in tuning some manufacturing processes. On the other hand, they display a desirable behavior when it comes to thermal shocks, despite the large linear thermal expansion coefficient, due to the relatively low Young modulus.

Given these goals for thermomechanical modeling, an extensive overview of the state-of-the-art in semi-crystalline polymer modeling is provided.

Thermoviscoelasticity is taken as the starting point. It is, nevertheless, not suitable due to nonlinear features in the behavior of semi-crystalline polymers and its description employing infinitesimal strains. Finite linear viscoelasticity is a generalization of linear viscoelasticity to large strains, although it does not provide a nonlinear description of semi-crystalline polymers. Single integral models are yet another approach that attempts to generalize the convolution integral description obtained from infinitesimal viscoelasticity. It is, however, not adequate for the computation framework based on the FEM method adopted here.

The most common approach is the use of rheological models with appropriate nonlinear viscous and elastic elements. Within the many possible arrangements of elastic and viscous elements, the generalization of the standard linear solid appears to be the most popular, as employed in the early model of Haward and Thackray (Haward and Thackray, 1968) and its generalization by Boyce, Park, and Ahzi (Boyce et al., 1988). The viscous element employed in both models is based on Eyring's model for thermally activated processes. Within that model, an athermal strength controls the yield stress of the polymer, which can be taken as an internal variable in order to capture strain softening behavior (Boyce et al., 1988), or even the double yield phenomenon (Hao et al., 2022a). These two elements, when combined with an Hencky model for the elastic element, are responsible for modeling the pre-yield and yield behavior, which contribute to what is commonly referred to as the intermolecular resistance. The strain hardening is captured most often through the use of a rubber-elasticity model, such as the Arruda-Bouce eight-chain model (Arruda et al., 1995) or the Edward-Vilgis model (Edwards and Vilgis, 1986) in the so-called network resistance. Sometimes, the viscous element proposed by Bergstrom-Boyce based on reptation (Bergström and Boyce, 1998, 2001) is also included in this resistance. That said, the numerical results presented here support the conclusion that the most recent models for thermoplastics such as the model in Hao et al. (2022a) are able to effectively capture the behavior of semi-crystalline polymers.

In order to include the bulk crystallinity in the description of semi-crystalline polymers, the most common approach is to model the resistance due to each phase using a thermoplastic model, such as those already mentioned. Their contributions are then weighted using a mixture rule, such as the Reuss or Voig mixture rules. This set of models is especially compelling because it allows for the description of a polymer at various degrees of crystallinity using a single set of material parameters. An interesting suggestion that models well the pre-yield and yield behavior of a semicrystalline polymer is the nonlinear Voigt mixture rule proposed in Ayoub et al. (2011). However, The authors only use this strategy for the intermolecular resistance, using different material parameters at each crystallinity level for the network resistance. In Abdul-Hameed et al. (2014), the network resistance is also modeled including crystalline and amorphous phases, and by employing the same modified Voigt rule. Models such as those in Ahzi et al. (2003); Makradi et al. (2005) and Cundiff et al. (2022) also try to model the increase in cyrstallinity with strain in polymers such as PET. Nevertheless, scrutinizing the numerical results provided here for the model in (Abdul-Hameed et al., 2014) the ability of said model to achieve this goal is limited when it comes to the description of the strain hardening behavior of semi-crystalline polymers that succeds yield. See this!

6.1   Future research and challenges

Building on the research efforts already made in this work to establish a robuts computational toolbox for the design of multi-functional semi-crystalline polymers in engineering applications, the author's PhD thesis will address the following challenges:

- More physical phenomena will be incorporated into the description of semi-crystalline polymers.   Electrical, magnetic, and hygromechanical phenomena are examples of such phenomena, which are critical in simulating some manufacturing processes and life service conditions.

- Another avenue of research to be explored, is the development of new macroscopic constitutive laws capable of accurately capturing the homogenized response of semi-crystalline polymers. In particular, models similar to those of Abdul-Hameed et al. (2014) and Ayoub et al. (2011), where bulk crystallinity is introduced and the material is characterized by the same material parameters with varying degrees of crystallintiy.   The main challenge is to make an appropriate generalization with the degree of crystallinity of the strain hardening response as understood from the numerical results reviewed in this work. In tandem, a thorough investigation of the thermomechanical behavior of the various models available, as well as a detailed validation using various mechanical loading and thermal regimes.

- Design of semi-crystalline polymer blends, such as nylon 6/PTFE blends, to provide optimal structural efficiency, manufacturability, and multi-functionality. Multi-scale approaches, which transfer information between scales, can provide a more detailed physical understanding of their behavior and the ability to tailor new materials by manipulating their microstructure.

- The modeling and design multi-functional semicrystalline polymeric materials by combining multi-scale strategies with machine learning is to be pursued. The work will initially focus on the mechanical response by finding optimal solutions for strength and toughness.   Later on, the coupling between the mechanical, electro, and transport fields will be addressed enabling the design of advanced multi-functional semicrystalline polymeric materials.